OBSERVING AND RECONSTRUCTING SUBSURFACE NANOSCALE

FEATURES USING DYNAMIC ATOMIC FORCE MICROSCOPY

A Dissertation

Submitted to the Faculty

of

Purdue University

by

Maria Jose Cadena

In Partial Fulfillment of the

Requirements for the Degree

of

Doctor of Philosophy

August 2018

Purdue University

West Lafayette, Indiana

THE PURDUE UNIVERSITY GRADUATE SCHOOL
STATEMENT OF DISSERTATION APPROVAL

Dr. Arvind Raman, Co-Chair

    School of Mechanical Engineering

Dr. Ronald G. Reifenberger, Co-Chair

    Department of Physics and Astronomy

Dr. Charles M. Krousgrill

    School of Mechanical Engineering

Dr. David B. Janes

    School of Electrical and Computer Engineering

Dr. Alam A. Muhammad

    School of Electrical and Computer Engineering

Approved by:

    Dr. Jay P. Gore

        Head of the School Graduate Program

ACKNOWLEDGMENTS

I would like to express my deep gratitude to my advisors, Prof. Arvind Raman and Prof. Ron Reifenberger, who have shared with me their passion for science and their knowledge surrounding the atomic force microscopy world. I thank Prof. Arvind for all the support, encouragement and advice given since the first time I joined his research group. I thank Prof. Ron for his advice, collaboration, and valuable discussions. Thanks to both for being part of this learning and growth path.

I would like to acknowledge all my lab mates from whom I have learned and entertained useful discussions. I thank Prof. Alam, Prof. Janes and Prof. Krousgrill for being part of my Ph.D. committee. I also thank our collaborators that provided us with samples for experiments. I would like to thank the staff and scientists at Birck Nanotechnology Center for all the assistance.

I am grateful for my parents and my family for their unconditional support and being a pole to the ground. I thank my friends for being at the other side of the balance in life.

TABLE OF CONTENTS

Page

LIST OF TABLES

LIST OF FIGURES

Figure   Page

ABBREVIATIONS

AFM	Atomic Force Microscopy (e)
SPM	Scanning Probe Microscopy
AM-AFM	Amplitude Modulation AFM
FM-AFM	Frequency Modulation AFM
KPFM	Kelvin Probe Force Microscopy
EFM	Electrostatic Force Microscopy
CR-AFM	Contact-Resonance AFM
DART	Dual AC Resonance Tracking
SEM	Scanning Electron Microscopy (e)
TEM	Transmission Electron Microscopy (e)
CPD	Contact Potential Difference

ABSTRACT

Cadena, Maria J. Ph.D., Purdue University, August 2018. Observing and Reconstructing Subsurface Nanoscale Features Using Dynamic Atomic Force Microscopy. Major Professors: Arvind Raman, Ronald Reifenberger, School of Mechanical Engineering.

The atomic force microscope (AFM), traditionally known as a nanoscale instrument for surface topography imaging and compositional contrast, has a unique ability to investigate buried, subsurface objects in non-destructive ways with very low energy. The underlying principle is the detection of interactions between the AFM probe and the sample subsurface in the presence of an external wave or field. The AFM is a newcomer to the field of subsurface imaging, in comparison to other available high-resolution techniques like transmission or scanning electron microscopy. Nevertheless, AFM offers significant advantages for subsurface imaging, such as the operation over a wide range of environments, a broad material compatibility, and the ability to investigate local material properties. These make the AFM an essential subsurface characterization tool for materials/devices that cannot be studied otherwise.

This thesis develops a comprehensive qualitative and quantitative framework underpinning the subsurface imaging capability of the AFM. We focus on the detection of either electrostatic force interactions or local mechanical properties, using 2nd-harmonic Kelvin probe force microscopy (KPFM) and contact-resonance AFM (CR-AFM), respectively. In 2nd-harmonic KPFM we exploit resonance-enhanced detection to boost the subsurface contrast with higher force sensitivity. In CR-AFM we use the dual AC resonance tracking (DART) technique, in which the excitation frequencies are near one of the contact resonance frequencies. Both techniques take advantage of the maximized response of the cantilever at resonance which improves the signal to

noise ratio. These enable high-resolution subsurface mapping on a variety of polymer composites.

A relevant challenge is the ability to reconstruct the properties of the subsurface objects from the experimental observables. We propose a method based on surrogate modelling that relies on computer experiments using finite element models. The latter are valuable due to the lack of analytical solutions that satisfy the complexity of the geometry of the probe-sample system and sample heterogeneity. We believe this work is of notable interest because offers one of few approaches for the non-destructive characterization of buried features with sub-micron dimensions.

1. INTRODUCTION

The continuous development of nanomaterials and nanodevices requires innovative new metrology techniques, particularly for the characterization at the sub-micron scale. Recently, there has been a growing interest in the sub-micron scale characterization of subsurface features in a number of materials/devices in a non-destructive, non-invasive manner. Sub-micron subsurface characterization can be key to understand the performance (or lack thereof) of these systems in many areas.

In materials science, such characterization can reveal the internal structure of bulk materials and nanocomposites at different length scales. For instance, to determine the distribution and connectivity of subsurface nano-inclusions in nanocomposites. These are critical factors affecting their performance in diverse applications [1], such as flexible transparent electrodes [2–4], optoelectronic devices [5,6], energy storage/conversion systems [7–10] or integrated circuits [11] (figure 1.1(a-c)).

In the semiconductor industry, subsurface defect detection and analysis of devices and interconnects at the sub-micron scale is of great importance in 3D structures and overlays [13]. The efficiency and performance of electronic devices are determined by the quality of interfaces between semiconductors, metals and non-metals. The interfaces can be buried beneath the surface layer as in the spin valve device shown in figure 1.1(d) [12]. In this figure, buried defects (grey regions and black dots) are detected underneath the surface between the bottom of a Cu wire and buried junction interfaces of $Ni_{0.8}Fe_{0.2}$.

Subsurface sub-micron imaging is also important in biology to investigate the cytoskeleton [14, 15] and subcellular phenomena [16], as well as the evaluation of cytotoxicity in the presence of nanomaterials [17].

Not surprisingly, many microscopy techniques have been recently employed for subsurface imaging, such as X-ray microscopy, confocal microscopy, transmission

electron microscopy (TEM), scanning electron microscopy (SEM), and atomic force microscopy (AFM). In this chapter, we will discuss the main sub-micron resolution techniques categorized as non-AFM (section 1.1) or AFM based techniques (section 1.2).

In comparison to the other high resolution techniques for subsurface imaging, the AFM is a newcomer to this field since it is primarily known as a nanoscale instrument for surface topography and compositional contrast. However, it has also the potential to investigate buried, subsurface objects. The underlying principle is the detection of interactions between an AFM probe and the subsurface of a sample, in the presence of an external wave or field that penetrates the subsurface. When compared to other high resolution microscopies, the relevant advantages of AFM are its low-energy, the operation over a wider range of materials and environments and its capability to investigate local material properties. In general, the AFM subsurface data is represented using 2D spatial maps with a contrast related to a sample physical property or an experimental variable. A key challenge is to take the given observables and to recreate the distribution, shape, and appearance of features within the volume of the sample. Methods used for this purpose are known as 3D reconstruction or tomography.

This chapter contains an outline of the main techniques used for subsurface imaging with a particular emphasis on the state-of-the-art for AFM based methods, distinguishing between destructive and non-destructive approaches. It is divided as follows: section 1.1 presents a discussion on non-AFM subsurface techniques, section 1.2 contains an overview of AFM and AFM based techniques for subsurface imaging, section 1.3 presents an outlook on the present and future challenges placed in the context of the contribution of this work, described in section 1.4.

1.1 Non-AFM Techniques for Subsurface Imaging

Several techniques have been used to investigate the interior of materials. Some of them have isotropic resolution, i.e. identical resolution in three dimensions, others have higher or lower resolution in the direction normal to the surface (z) compared to the lateral (x-y) directions, as shown in figure 1.2 [18]. X-ray microscopy is distinguished by having a field-of-view in three-dimensions but lower lateral resolution, in a range of 40 - 100 nm [19]. Secondary ion mass spectroscopy (SIMS) has a low lateral (100 nm) and depth resolution (< 5 nm) [20, 21]. High lateral resolution techniques are transmission electron microscopy (TEM), focused ion beam (FIB) / scanning electron microscopy (SEM) [22], atom probe microscopy (APM) [23] and atomic force microscopy (AFM) [24]. These are typically 2D imaging techniques that can resolve the subsurface of a specimen within one to hundreds of nanometers deep. In what follows, we describe the most common non-AFM high resolution techniques at the nanoscale, i.e. TEM and SEM, that possess a resolution comparable to the AFM.

TEM and SEM were introduced in the late 1930/early 1940s. Both make use of electrons and their interaction with matter. TEM generates atomic level images related to the sample chemistry and crystallography [25]. It has a greater resolution and higher magnification than the SEM. However, some of its limitations are no depth sensitivity in a single image (2D image) [26] and time consuming thinning processes of the specimen to ensure transmission of electrons, which makes it a destructive method. The SEM can image bulk specimens based on scattering processes and diffusion of electrons, it has a larger field of view and provides more information about the shape and the location of features relative to each other [27].

For subsurface imaging and 3D reconstruction applications, destructive or non-destructive approaches have been implemented to access the layers underneath the surface. Common destructive methods, known as slice and view, involve a sectioning process of the specimen [22] using ultramicrotomy [28–32], ion milling [33–35] or

polishing/etching [36,37]. After the upper layer is removed, the exposed surface is imaged by one of the microscopy methods. For instance, figure 1.3(a) shows a schematic representation of an ultramicrotome mounted inside an environmental SEM, in which a diamond knife cut thin slices of the specimen (50 to 100 nm thick) and then the electron beam images the remaining block face [38]. Figure 1.3(b) illustrates a dual beam instrument, in which a FIB is used to mill thin slices of a specimen previously prepared in a cube shape. After removal of thin layers, SEM is used for imaging the exposed surface [33, 35, 39]. Some examples are shown in figure 1.3(c-d), corresponding to SEM images of a graphene-polystyrene (PS) composite [32] and TEM images of intercalated/exfoliated PS and polypropylene-g-maleic anhydride (PPgMA) nanocomposites, after sectioning by ultramicrotomy [28]. To achieve 3D reconstruction using these destructive approaches, serial sectioning is applied to collect multiple images after each layer removal, which are then assembled by computational algorithms [22, 35].

On the other hand, there has been a great effort in the development of non-destructive approaches based on SEM and TEM. The capability of the SEM has been demonstrated using a voltage contrast method, also known as charging effect, typically at high acceleration voltages. It has been applied to image conducting nanostructures in a dielectric matrix, such as CNTs or graphene nanoplatelets embedded in polymer composites [40–44], Si nanostructures embedded in SiO_2 [45] or overlay marks [46, 47]. The common feature within these studies is the conductive or semiconductive nature of the specimens. In fact, subsurface image contrast strongly depends on the conductivity of the specimen [41–43]. Figure 1.4(a), shows an example of subsurface imaging of SWCNTs in a polyimide (PI) composite above the percolation threshold, using accelerating voltages of 5kV and 20kV. The latter gives higher contrast and better resolution [43].

A non-destructive imaging tool based on TEM is electron tomography. With this technique, the creation of 3D images is achieved through the acquisition of 2D TEM projections at different angles around a tilt axis [48]. As a result of recent develop-

ments in instrumentation and software, it has been applied to a series of systems such as electronic devices, composites, biomaterials, metals and alloys [18]. For example, figure 1.4(b) corresponds to images of agglomerated grafted silica particles in a PS matrix. The 3D rendering is produced after processing images recorded with tilt angles ranging from -60° to 60° with an increment of 1° [49]. The orthogonal slices exhibit an elongation artifact in the z direction due to a "missing wedge" during recording [50]. The sample still requires preparation before imaging. In this case, the nanocomposite was cut in a 250 nm thick film, then floated onto deionized water and set on a copper grid.

Although SEM and TEM are useful high resolution imaging tools for subsurface imaging, they have limitations for a wider range of applications. Specifically they are invasive, energetic imaging techniques that can locally damage the sample under study, by electron beam induced heating, electrostatic charging, ionization damage, displacement damage, sputtering and hydrocarbon contamination [51]. These issues are particularly problematic for polymer based samples whose properties can change due to these effects. Additionally, complex chemical and mechanical preparation techniques are required in the case of electron-beam-sensitive materials such as soft matter (polymers) or biological samples [52, 53]. Also, in the case of TEM, for 2D projections, materials must be transparent to electrons and machinable into some thin slices, for which not all specimens are suitable. For 3D imaging, electron tomography would require low beam dose, controlled acquisition times and assumption of specific symmetry of the specimen for post-processing algorithms [48, 53]. Both EM techniques generally require vacuum conditions, although recent advances allow imaging under liquid using environmental chambers or closed liquid cells, while the rest of the microscope is kept at low pressure [54].

1.2 Subsurface Imaging Using AFM

In comparison to SEM and TEM based high resolution subsurface imaging techniques described above, AFM based subsurface imaging techniques boast special advantages as described below:

1. These are low energy techniques, hence non-invasive. There is little charging or damage of sample,

2. Easy sample preparation in comparison to complex or time consuming processes required for SEM or TEM [55].

3. There is no need to apply destructive processes to the samples, preserving the native states of the specimen.

4. Hard, soft or hybrid materials can be imaged. Electrical conductivity of samples is not required [56–58].

5. It allows subsurface imaging through the detection of a variety of detectable fields.

6. Beyond morphology, it is a useful tool to investigate local material properties such as mechanical [59–61], electrical [62–65], chemical [66–68].

7. Operates in a wider range of environments: air [57], liquid [69,70] and vacuum [71].

In what follows we provide a brief overview of AFM and of the state-of the-art of AFM based subsurface imaging.

1.2.1 An Overview of AFM

AFM is classified as a scanning probe technique. Its predecessor is the scanning tunneling microscopy (STM), introduced in the early 1980s. The STM provides atomic resolution (~ 0.1 nm) [72,73] based on a tunneling current flowing through a

sharp tip held nanometers apart from a substrate. This limits its use to electrically conductive samples (metals or semiconductors). It also usually requires ultrahigh vacuum conditions for clean and well-defined surfaces [55, 74]. After the remarkable success of the STM, AFM made its appearance in 1986. AFM was originally thought as a method to analyze the surfaces of both conductors and insulators on the atomic scale, overcoming the limitation of the STM. The AFM is notable for its high sensitivity to detect interatomic forces acting on a sharp tip in close proximity to a surface [56].

The essential components for the operation of an AFM are shown in figure 1.5. The probe is composed of a microcantilever with an integrated conical sharp tip at one of its end. The head consists of a probe holder, a system to measure the microcantilever deflection, in this case, the laser beam bounce detection method used in current AFMs, and a probe excitation mechanism, commonly a piezoactuator. The scanner regulates the position of the tip relative to the sample in the x-y-z direction and the feedback loop controls a measure of microcantilever vibration or mechanics that is sensitive to the interaction forces (deflection, amplitude, frequency or phase shift) while scanning [75].

The physics of the AFM draws upon the interaction forces developed between the tip and the sample. In general, AFM techniques are categorized within two modes: static and dynamic. In static AFM, tip-surface forces are first measured as a function of the separation distance (Z). In a second approach, known as contact mode AFM (CM-AFM), the tip is brought into contact with the sample surface for scanning at a constant applied force. Due to high lateral forces, this method is not appropriate in some cases, such as in soft or weakly bonded materials.

Dynamic AFM is based on the induced oscillation of the microcantilever-tip above the sample. The vibration can be generated either by dither-piezo excitation (moving the base of the microcantilever) or direct excitation by means of magnetic field, Lorentz force or a pulsed laser (phototermal), applied to the microcantilever. The frequency of the excitation usually matches the resonance frequency of the fundamental

mode of the microcantilever, which starts vibrating with a certain amplitude (A) and phase (ϕ). Then, variations in A, ϕ or frequency are measured to infer the tip-sample interaction forces. For convenience, in most of the text, frequency is expressed in terms of the angular frequency $\omega = 2\pi f$. The frequency of the fundamental mode is expressed as ω_0 ($\omega_0 = \omega_1$).

Two of the relevant features of dynamic AFM techniques in comparison to CM-AFM are the lower lateral forces and access to additional observables for investigation of local surface material properties [76, 77]. Dynamic AFM covers a wide variety of techniques. The most common is amplitude modulation AFM (AM-AFM). In this method, the feedback loop controls the oscillation amplitude of the microcantilever, while the sample is scanned at a constant separation distance. The motion of the microcantilever (or sample) during this process is rendered as the topography of the sample. Furthermore, mapping of phase (ϕ) shifts provides useful compositional information, mainly based on local mechanical properties. AM-AFM forms the basis for other dynamic techniques as a first step to track surface topography in air or liquid. In addition to a feedback based on A, the drive frequency can be modulated to keep a constant ϕ while maintaining a constant frequency shift during the scan (three feedback loops). This approach is known as frequency modulation AFM (FM-AFM). It has been used to acquire very high resolution images under vacuum, ambient and under liquid conditions and also used in combination with other techniques [66, 78].

Most dynamic AFM techniques described above are used for surface characterization. Now we describe the existing state of the art with respect to subsurface imaging. Subsurface imaging using AFM has been demonstrated using either destructive (slice-and-view) or non-destructive approaches. The former has been promoted for 3D reconstruction applications and involves sectioning processes of the specimen, such as etching, ultramicrotomy or scratching [24].

Some examples of slice-and-view approaches are given in figure 1.6. Plasma etching in combination with AM-AFM have been used to image domain structures of a triblock copolymer poly-(styrene-block-butadiene-block-styrene) (SBS) film. Phase

contrast reveals PS cylinders (bright) embedded into a polybutadiene (PB) matrix (dark), after removal of thin layers (7.5 ± 0.2 nm) of the sample. A volume image ($200 \times 160 \times 45 \text{nm}^3$) is reconstructed from a series of phase images [79] taken between serial sectioning. Another example uses a doped ultra-sharp full diamond probe to remove the upper layer of the specimen, as shown in the topography in figure 1.6(b). The probe scans successively digging into the sample, while a bias is applied between the probe and a TiN electrode at the bottom. An AFM technique, known as scanning spreading resistance microscopy (SSRM), is used to generate 2D maps of the local resistance. Vertically aligned bundles of multi-walled carbon nanotubes (MWCNTs) are distinguished from a surrounding oxide matrix in the map. Processing stacks of 2D resistance images results in a 3D volume representation [80]. Figure 1.6(c) corresponds to images of a conductive graphene network embedded in PS. Ultramicrotomy is used as a sectioning process and current distribution maps are generated using conductive AFM (C-AFM). A 3D volume ($2.5 \times 2.5 \times 0.34 \mu\text{m}^3$) reconstruction of a single graphene cluster is achieved through a series of current maps obtained after microtome cuts with steps of 12 nm.

In what follows we present a summary of non-destructive AFM techniques that have been used for subsurface imaging. Depending on the detection mechanism, the state of the art breaks up into three areas (figure 1.7): (1) surface vibrations, (2) local mechanical properties and (3) electrostatic force interactions.

1.2.2 Surface Vibration Detection

Within this dynamic AFM classification, we encounter the approaches characterized by surface detection of scattering of an ultrasonic wave that is launched from below the sample to the top, due to buried nano-objects. The AFM is then used to map out the resulting patterns of surface vibration. In the literature, various studies are found based on this principle but with slight modifications in the technique. For instance, in ultrasonic force microscopy (UFM), a high frequency wave (usually in the

MHz range) is sent from below the sample [81] or through the microcantilever [82], as indicated in figure 1.8(a). This technique has been used to visualize subsurface edge dislocations in highly oriented pyrolytic graphite [83].

On the other hand, in heterodyne force microscopy (HFM) two ultrasound waves are utilized, as shown in figure 1.8(b). One is launched from the bottom of the sample at a frequency ω_1, another via the microcantilever at a frequency ω_2 and the maximum tip-surface distance is modulated at a beat frequency $(\omega_2 - \omega_1)$, as shown in figure 1.8(b). HFM relies on the nonlinear tip-sample interaction as a result of the frequency mixing of both waves. It has been used to resolve near surface inclusions of rubber added to poly(methylmethacrylate) (PMMA) [84].

A modification to HFM is scanning near-field ultrasound holography (SNFUH). This technique detects amplitude and phase changes of the acoustic standing wave in near-contact mode, reportedly appropriate for soft and biological specimens [85]. It has been used in several heterogeneous systems, for instance to detect gold nanoparticles beneath a polymer cover, voids or defects in coated Si_3N_4 structures as shown in figure 1.9, malaria parasites inside infected red blood cells [85], single-walled carbon nanohorns inside cells from mice lungs [17], silica nanoparticles within a macrophage [86] or buried defects in copper interconnects [87]. Wave scattering and diffraction are thought to make contributions to the image contrast [85,88]. However, the exact imaging mechanism is still not fully understood, since theoretical calculations demonstrate that both amplitude and phase contrast are much weaker than the experimental measurements [89].

In mode-synthesizing AFM (MSAFM), the probe and the sample are excited by forces containing a number of known frequency components or modes [90], as shown in figure 1.8(c). The mechanical waves scatter due to the internal structure of the sample influencing the tip-surface coupling sensed by the tip. In addition, a new set of modes is generated by the tip which mixes the waves at the surface with the microcantilever's own frequency components [91]. Therefore, a multiple order spectrum is created. Amplitude and phase images generated at each of the synthesized modes contain

information of topography as well as mechanical properties of surface and subsurface features. This technique has been used to study layers of poplar wood cells and nickel nanodots within a germanium coating [90].

1.2.3 Detection of Local Mechanical Properties

Within the available dynamic AFM techniques, some take advantage of the dynamics of the microcantilever and the subtle variations of local mechanical properties caused by subsurface objects. Some of these techniques applied for subsurface imaging are: amplitude modulation AFM (AM-AFM), multimodal AFM (figure 1.10(a)), contact resonance AFM (CR-AFM)(figure 1.10(b)) and DC-biased AM-AFM (figure 1.10)(c).

An approach using AM-AFM has been demonstrated for subsurface imaging of soft materials by adjusting the tip-sample indentation [92]. This method relies on amplitude and phase distance curves taken pointwise above a selected region. The data are processed to obtain true sample surface [93], tip indentation, and depth resolved images. For instance, cylinders of PS (20 nm deep) covered by polybutadiene are distinguished by contrast in a phase map and reconstructed as a function of depth. Similarly, crystalline and amorphous regions are mapped under the surface of a thin film of elastomeric polypropylene (EPP) to a depth of 19 nm.

Simultaneous excitation of several flexural modes of the microcantilever has been applied to gather complementary information, higher compositional resolution and sensitivity through dynamic AFM [94]. The most common is a bimodal scheme in which the microcantilever is mechanically excited by two driving forces, each at frequencies that match two of the flexural modes, usually the first and second resonances. The first mode is used to image the topography of the surface similar to AM-AFM. The second mode has been utilized to map local properties based on dissipation, Young modulus, viscosity and short and long-range interactions [61]. Recently, the capability of bimodal and trimodal (simultaneous excitation of three modes) for sub-

surface imaging of nanostructures embedded in a soft materials has been shown [**?**,95]. For instance, silicon nanowires, iron oxide nanoparticles [95] and glass nanoparticles [**?**] have been imaged underneath a thin film of polydimethylsiloxane (PDMS). In these studies, the first mode is used to map the surface topography, the second mode to enhance subsurface contrast, and the third mode to modulate sample indentation. Figure 1.11(a) shows the detection of subsurface silicon nanowires covered by 70 nm thick PDMS film using trimodal AFM. These are not visible through conventional tapping mode [95].

Detection of minute elastic variations, i.e., contact stiffness induced by subsurface features is the foundation of contact resonance AFM (CR-AFM) [96,97]. Embedded inclusions or defects influence local mechanical properties so long as the elastic strain fields extend deep enough into the sample [98]. One mechanical property that is influenced is the local contact stiffness which subsequently alters the microcantilever dynamics. When the contact stiffness changes, the contact resonance frequency (ω_c) of the microcantilever will shift correspondingly. With this principle, CR-AFM has been used mainly for characterizing mechanical properties [99, 100]. In addition, the microcantilever oscillation includes frequency, amplitude and phase information which are all able to generate subsurface contrast information. In this way, CR-AFM methods have been exploited to probe nanoparticles (NPs) buried in polymers [96,97]. For example, figure 1.11(b) shows the detection of silica NPs buried under a 125 nm thick PS film using the contact stiffness contrast map ($\Delta k/k_b$) [100]. To enhance the sensitivity, higher eigenmodes of the microcantilever are often employed.

Lastly, DC-biased amplitude modulation AFM uses a dc bias voltage between the tip and the sample, while it operates in AM mode, as shown in figure 1.10(d). The microcantilever oscillates near its resonance frequency in attractive regime (non-contact mode). Phase contrast allows the detection of subsurface features. Electromechanical dissipation has been explained as the main mechanism for contrast formation [101]. This technique has been applied to study 2D arrangement of SWCNTs and a 3D

network of doubled-walled nanotubes (DWCNTs) underneath a polymer mix (SEBS-PS) [101] and SWCNTs dispersed in a PI composite [102].

1.2.4 Detection of Electrostatic Force Interactions

Non-invasive electrostatic techniques based on AFM are also used to attain sub-surface information. Two techniques utilize the long range electrostatic interaction between the probe and the sample under the influence of an external electric field. These are known as electrostatic force microscopy (EFM) and Kelvin probe force microscopy (KPFM). EFM and KPFM can be used either in single-pass or in double-pass mode. In the former, only one scan per line is used to simultaneously measure surface topography and the microcantilever response to the electric field [103]. The latter requires two scans, the first records the topography and the second senses the electrostatic interactions at a certain lift-off height above the sample [104], as shown in figures 1.12(a),(b).

In single-pass EFM, an AC bias voltage is applied across the tip-sample system and the amplitude and phase of the microcantilever response at the frequency of the electrical excitation is recorded [105]. In double-pass EFM a DC voltage is applied during the second scan while the tip oscillates at or close to its resonance frequency (figure 1.12(a)). Phase shift is generated in the microcantilever response due to the electrostatic force gradient. This shift in phase is considered as the EFM signal [106].

For KPFM, single- and double-pass modes work under the same principle, i.e. an applied DC bias equal to the contact potential difference (CPD) between the tip and the sample nullifies the microcantilever response at the frequency of the AC excitation (figure 1.12(b)). This feature of the KPFM technique is particularly useful for the investigation of surface potential [107,108]. However, additionally it is possible to capture the microcantilever response at the second harmonic of the electrostatic force. This signal is proportional to the gradient of the capacitance with respect to the tip-sample distance, which depends mainly on the dielectric properties of the

sample [102]. Due to the utility of this channel, this technique is named 2nd-harmonic KPFM [109].

Both EFM and KPFM have been used for surface compositional mapping based on heterogeneities in the electrical properties when different phases are present in a material [105, 110, 111]. This feature has been exploited in the identification of subsurface components. For instance, EFM has been used to distinguish organic domains of a methyl-terminated monolayer ($CH_3(CH_2)_{16}SH$) and an alcohol-terminated monolayer ($HO(CH_2)_{16}SH$) buried under a polystyrene film of 430±50 nm [112] thick. The same technique has been used to visualize individual single-walled carbon nanotubes (SWCNTs) suspended in a matrix of polymethylmethacrylate (PMMA) or SWNT networks embedded in polyimide (PI) films [102, 113]. Recently, imaging of networks of multi-walled carbon nanotubes (MWCNTs) within a dried latex film was reported [114]. Also KPFM studies have been reported on imaging SWCNTs-PI composites using the 2nd-harmonic channel [102, 109]. By using maps of CPD, buried micropatterns of self-assembled monolayers deposited on a gold substrate have been determined under a coating of PS [115].

Previously, we performed a comparative study that imaged embedded SWCNTs in a PI composite film, as shown in figure 1.13, using a variety of electrostatic methods [102]. This work reveals the capability of three of the techniques for subsurface imaging mentioned above. First, second and third rows in figure 1.13 correspond to the observables obtained by DC-biased AM-AFM, single-pass EFM and single pass KPFM, respectively. It is notable that no CNTs are revealed in the surface topography (figures 1.13(a,d,g)). The presence of CNTs are revealed in the phase channel corresponding to DC-biased AM-AFM (figure 1.13(b)), the amplitude of the electrostatic force in EFM (figure 1.13(e)) or the capacitance gradient in KPFM (figure 1.13(i)). Among these, the KPFM channel ($\partial C/\partial Z$) is considered the best to obtain high-contrast subsurface images of the CNT networks, since the surface charging and subsurface images are well-decoupled.

1.3 Outlook of Present and Future Challenges

Remarkable advances have taken place in AFM techniques for non-invasive subsurface imaging, as presented in the review above. Reliable subsurface images have been achieved by means of different mechanisms, either by acoustic (ultrasound) waves, electric or stress fields, or multimodal schemes. It is worthwhile to summarize the advantages offered by each class of techniques to allow a rational choice based on the available instrumentation or researcher expertise.

In terms of the experimental setup, some techniques are easy to implement based on standard equipment in commercial AFMs, such as DC-biased AM-AFM, EFM, KPFM. Others require external resources, such as additional lock-in amplifiers in tri-modal AFM [95], signal generators or mixers in MSAFM [90], one or two transducers (typically piezoelectric) in UFM [83,97], HFM [84], SNFUH [116] or CR-AFM [96]. In addition, complex data post-processing is required in MSAFM or for the APD curves obtained by AM-AFM mode [92]. This can become a drawback for widespread and reproducible use.

In general, the outcome of all techniques are 2D maps corresponding to one or more observables. Some of these are intrinsically qualitative but others can be interpreted in a quantitative manner. Both aspects are faced with critical challenges. On the one hand, visualization of subsurface features with high resolution requires attention to relevant aspects such as spatial resolution, depth sensitivity (how deep we can "see"), contrast enhancement, artifact identification, and dissociation of surface and subsurface information. These characteristics are associated with the quality of the obtained maps, which usually are measurements of amplitude, phase or frequency shifts with respect to some reference excitation.

On the other hand, a current concern is the ability to gather spatial distribution data for 3D volume reconstruction, which is not a straightforward task. First, it requires a clear understanding of the underlying mechanisms behind the technique. Second, the observables need a quantitative interpretation related to a physical vari-

able. This usually involves the creation of a mathematical model. Due to the complexity of the probe geometry, sample heterogeneity or the presence of non-linear interactions, an analytical solution is not always feasible, therefore numerical and computational methods are mostly required. Third, a set of 2D maps or curves are needed to reproduce a 3D representation with spatial (x-y-z) and morphology (shape, size) information of the subsurface features. This would require the manipulation of the experimental variable(s) or conditions, for which there is not always an obvious procedure.

Some novel solutions have been reported in the literature using mechanical or electrical excitation techniques. For instance, amplitude and phase distance (APD) curves have been used to create a depth resolved image of a thin film of polypropylene (PP), as shown in figure 1.14(a) [92]. This is obtained by reconstructed maps of the tip-sample spring constant (k_{TS}), which are combined into a volume image. The k_{TS} maps are the result of converting 50 x 50 APD curves measured in the region indicated by the phase image in figure 1.14(c). Some k_{TS} slices are shown for three different depths in figures 1.14(d-f). This approach is based on the heterogeneity of the mechanical properties in the specimen. In this case, hard regions of PP (crystalline - in yellow) are distinguished from the soft (amorphous) regions. As it is indicated in figure 1.14(a) and the cross-section of a lamella in figure 1.14(b), the resolved depth is 19 nm. In general, the depth resolution of this technique is limited by how much the tip can indent the sample without damage.

Another approach combines 2nd-harmonic KPFM with finite element analysis (FEA) to obtain a 3D reconstruction of SWCNTs embedded in a polyimide (PI) composite film, as shown in figure 1.15 [109]. Embedded SWCNTs are clearly detectable through the 2nd-harmonic or $\partial C / \partial Z$ channel, as in figure 1.12(b). The capacitance gradient difference ($\Delta C' = (\partial C / \partial Z)_{SWCNT} - (\partial C / \partial Z)_{PI}$) is calculated as a function of CNT depth using FEA, as shown in figure 1.12(a), which is also obtained experimentally. These curves are used to convert the experimental $\partial C / \partial Z$

data (figure 1.12(b)) into depth information. The rationale of this method, is based on the proportional relation between $\partial C/\partial Z$ and depth.

Much remains to be understood and explored in the noninvasive characterization of subsurface structures and the generation of quantitative 3D spatial distribution maps. The family of techniques based on AFM is relatively young in comparison to the other high resolution microscopy such as SEM or TEM, but it has become a promising versatile tool.

1.4 Contributions and Layout of This Thesis

Following the brief review on AFM subsurface techniques presented in this chapter, this thesis chapters focuses primarily on 2nd-harmonic KPFM and CR-AFM.

Second-harmonic KPFM has emerged as a key tool for subsurface nanoscale imaging, typically demonstrated in CNT based polymer composites [102, 109]. Chapter 2 exploits resonance-enhanced mode in 2nd-harmonic KPFM for high resolution subsurface imaging of a variety of polymer nanocomposites. This study explores the advantages of detection at resonance of the electrostatic force, which remain unexplored for subsurface imaging applications. Additionally, a finite element model using Comsol Multiphysics is introduced, to gain a deeper understanding in the role of the electrostatic force and analyze the depth sensitivity, lateral resolution and contrast dependence on dielectric properties of the material. The model is in turn used to interpret quantitatively the experimental observable ($A_{2\omega_e}$) as a function of depth.

The capability of CR-AFM for subsurface imaging is explored in Chapter 3. A detailed comparison with 2nd-harmonic KPFM is presented in terms of lateral resolution and depth sensitivity. For this purpose, a much needed simultaneous experiment is performed to compare the two techniques, using a SWCNTs/PI composite film as a sample. Both techniques have been reported separately for subsurface imaging, but no direct comparison has been done until now. This study lays out the advantages, limitations and disadvantages offered by each technique. Furthermore, a significant

result is the agreement in the estimation of depth of subsurface CNTs, between the two techniques.

Chapter 4 presents a method for 3D volume reconstruction using electrostatic force detection within the framework of KPFM. This process involves the creation of a surrogate model based on numerical results obtained via finite element computations and the acquisition of a set of experimental subsurface data. Contrary to prior work, this non-destructive approach can be used not only to estimate the depth but to reconstruct the size of the buried object, and in principle estimate other unknown properties. Validation is made on a model sample, composed of nanoparticles ($BaTiO_3$) buried under a thin polymer film (PDMS).

We extend the reconstruction approach based on surrogate modeling to CR-AFM, which is detailed in Chapter 5. CR-AFM is advantageous due to the highly localized stress field. The local contact stiffness is measured between the contact area of the apex of the tip with the surface of the sample. This in turn provides higher lateral resolution and there is no contributions of the macroscopic parts of the probe as in KPFM.

Finally, in chapter 6 we summarize the contributions of this thesis and propose some future research directions.
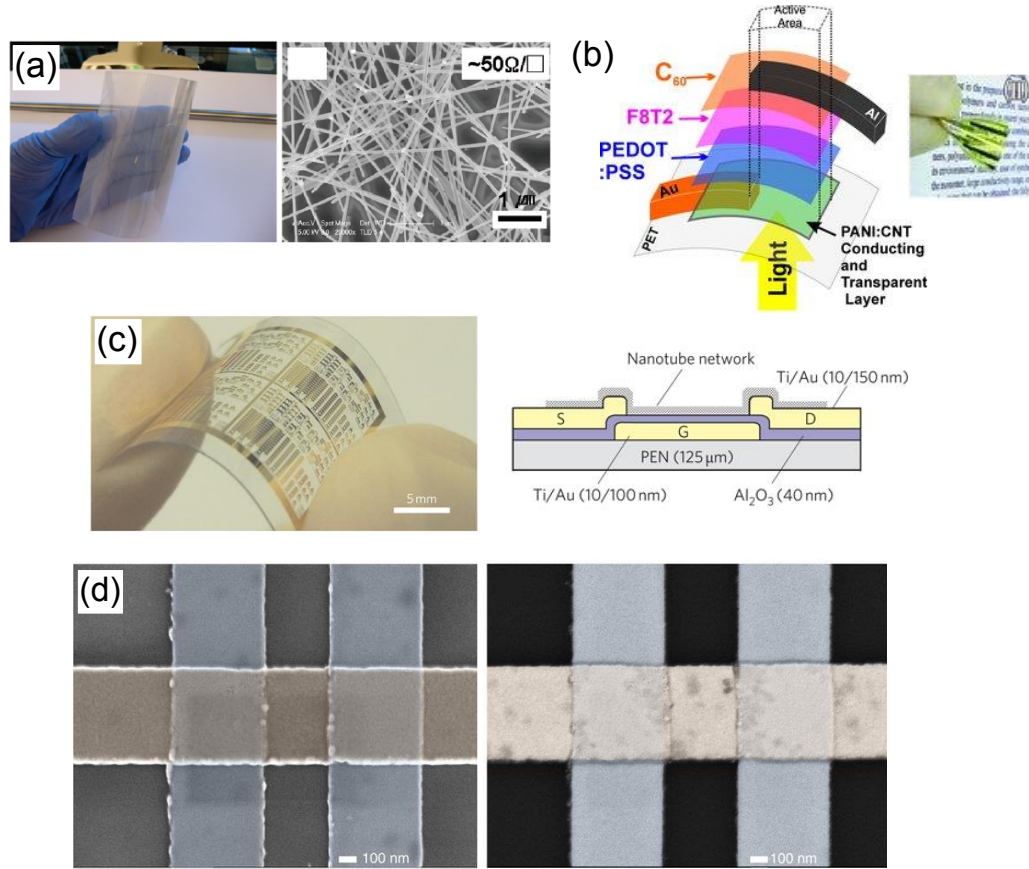
Figure 1.1. Nanocomposites and nanoelectronic devices where sub-surface nanoscale characterization is important. (a) Transparent and conductive silver nanowire (Ag NW) coating on polyethylene terephthalate (PET) substrate with a sheet resistance of 50Ω/sq. Reprinted with permission from [5]. Copyright American Chemical Society 2010. (b) ITO-free flexible organic solar cell built over a PET/polyaniline:carbon nanotube film used as transparent electrode. Reprinted with permission from [9]. Copyright (2013) John Wiley & Sons, Inc. (c) CNT thin film transistor (TFT) fabricated on a flexible and transparent polyethylene naphthalate (PEN) substrate and a schematic cross-section of a bottom-gate TFT with an Al_2O_3 gate insulator. Adapted by permission from Macmillan Publishers Ltd: Nature Nanotechnology [11], Copyright (2011). (d) (Left) SEM image of a spin-valve device consisting of two 200 x 200 nm $Ni_{0.8}Fe_{0.2}$/Cu junctions, followed by top 70 nm thick Cu wires. (Right) Defects detected in the Cu wire by backscattered electrons (BSE) near the buried junction interfaces. Adapted by permission from Nature Publishing group: Nature Communications [12], Copyright (2016).
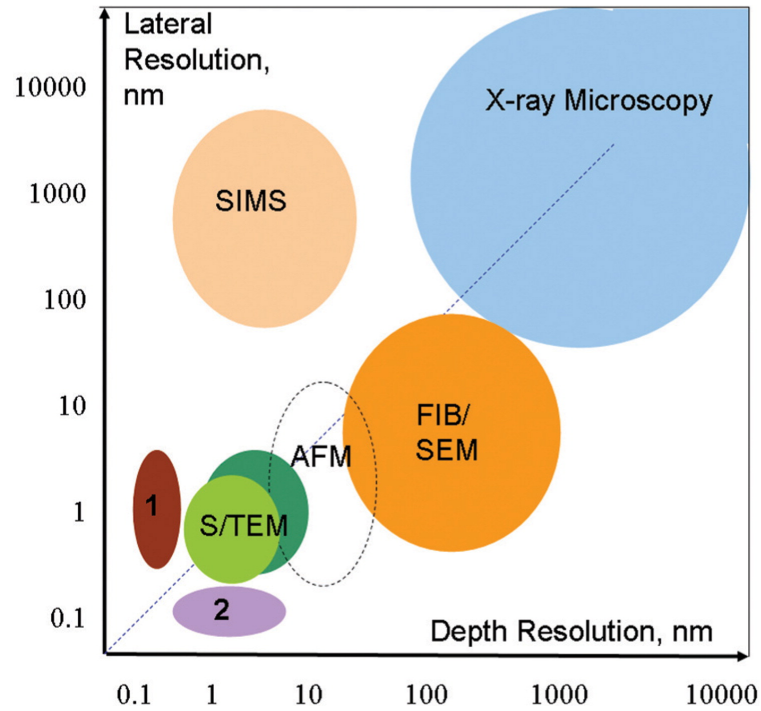
Figure 1.2. Diagram of lateral versus depth resolution for the techniques used in the investigation of the internal structure of materials, known as tomography. X-ray microscopy is distinguished by having three-dimensional resolution but lower lateral resolution. High lateral resolution techniques are (1) atom probe tomography, (2) scanning transmission electron microscopy (STEM), electron tomography (green color), atomic force microscopy (AFM), focused ion beam (FIB) / scanning electron microscopy (SEM). Secondary ion mass spectroscopy (SIMS) have a low lateral and depth resolution. Reprinted from [18], with permission from Elsevier.
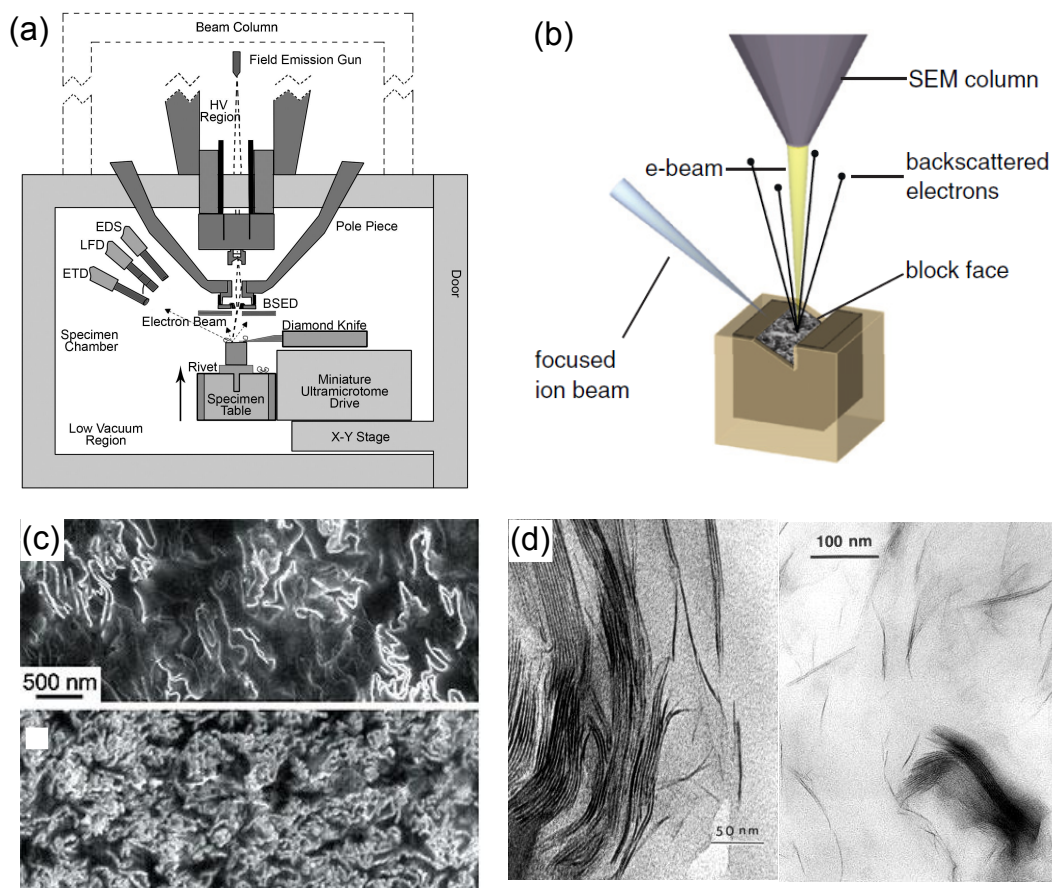
Figure 1.3. (a) Schematic diagrams of slicing procedures using (a) ultramicrotomy inside an environmental SEM. It has backscattered electron (BSE) and secondary electron detectors (SE) for imaging under high and low vacuum conditions. Adapted from [38], with permission from Wiley. (b) Slice and view process in dual beam FIB/SEM. Layers are cut with the ion beam at an angle of 52deg and then imaged by the electron beam. Reprinted with permission from [35]. Reprinted from [35], Copyright (2012), with permission from Elsevier. (c) SEM image of microtomed graphene (0.24 and 1.44 vol% -polystyrene composite. Adapted by permission from Macmillan Publishers Ltd: Nature [32], copyright (2006). (d) High-magnification TEM image of intercalated/exfoliated PS nanocomposite (mass fraction = 5% AMMT) and a PPgMA intercalated/exfoliated nanocomposite (mass fraction = 8% AMMT). Reprinted with permission from [28]. Copyright (2013) John Wiley & Sons, Inc.
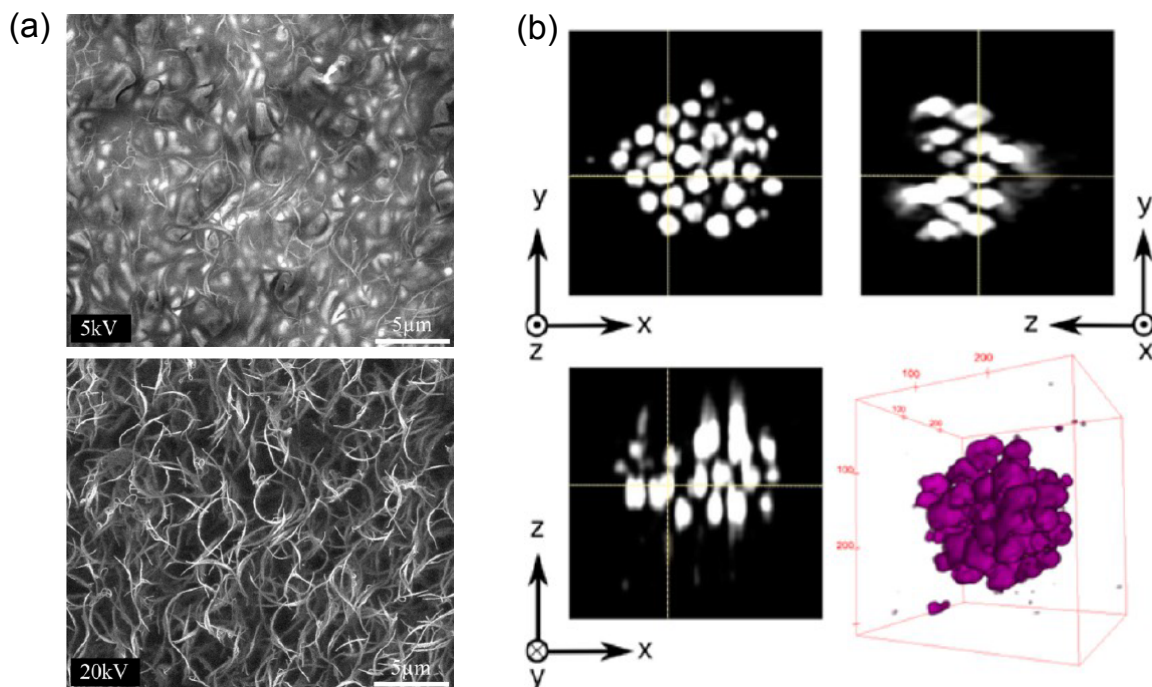
Figure 1.4. Non-destructive approaches with SEM and TEM. (a) Voltage contrast SEM using accelerating voltages of 5kV and 20kV showing SWCNTs embedded in PI. Reprinted from [43], Copyright (2013), with permission from Elsevier. (b) Observation of agglomerated grafted silica particles in a polystyrene matrix, obtained using transmission electron tomography. The 3D rendering is produced after processing images recorded with tilt angles. The orthogonal slices slices exhibit an elongation artifact in the z direction. Reprinted with permission from [49]. Copyright (2014) American Chemical Society.
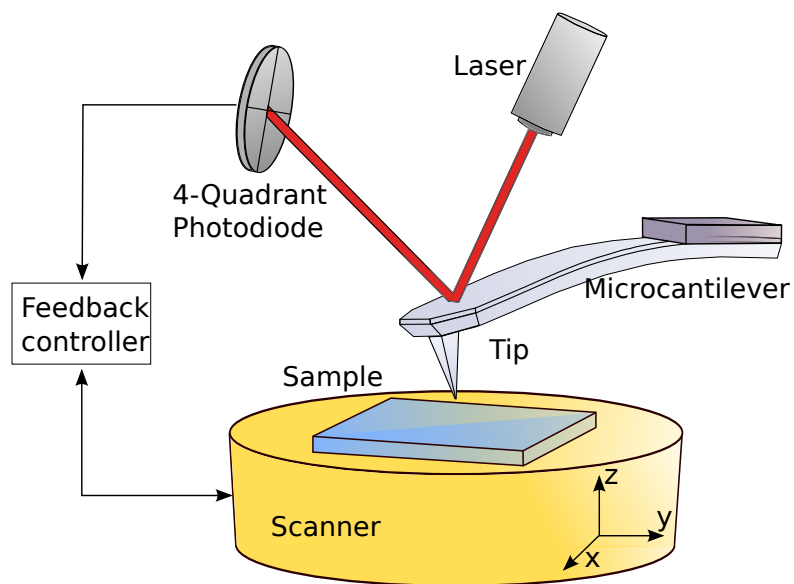
Figure 1.5. Schematic representation of the basic components of an atomic force microscope. Main elements of the head are: the laser beam bounce detection system (laser and 4-quadrant photodiode), a holder of the probe (microcantilever-tip assembly), and a probe excitation mechanism. The scanner controls the position of the tip relative to the sample. The feedback loop usually maintains constant one of the experimental variables.
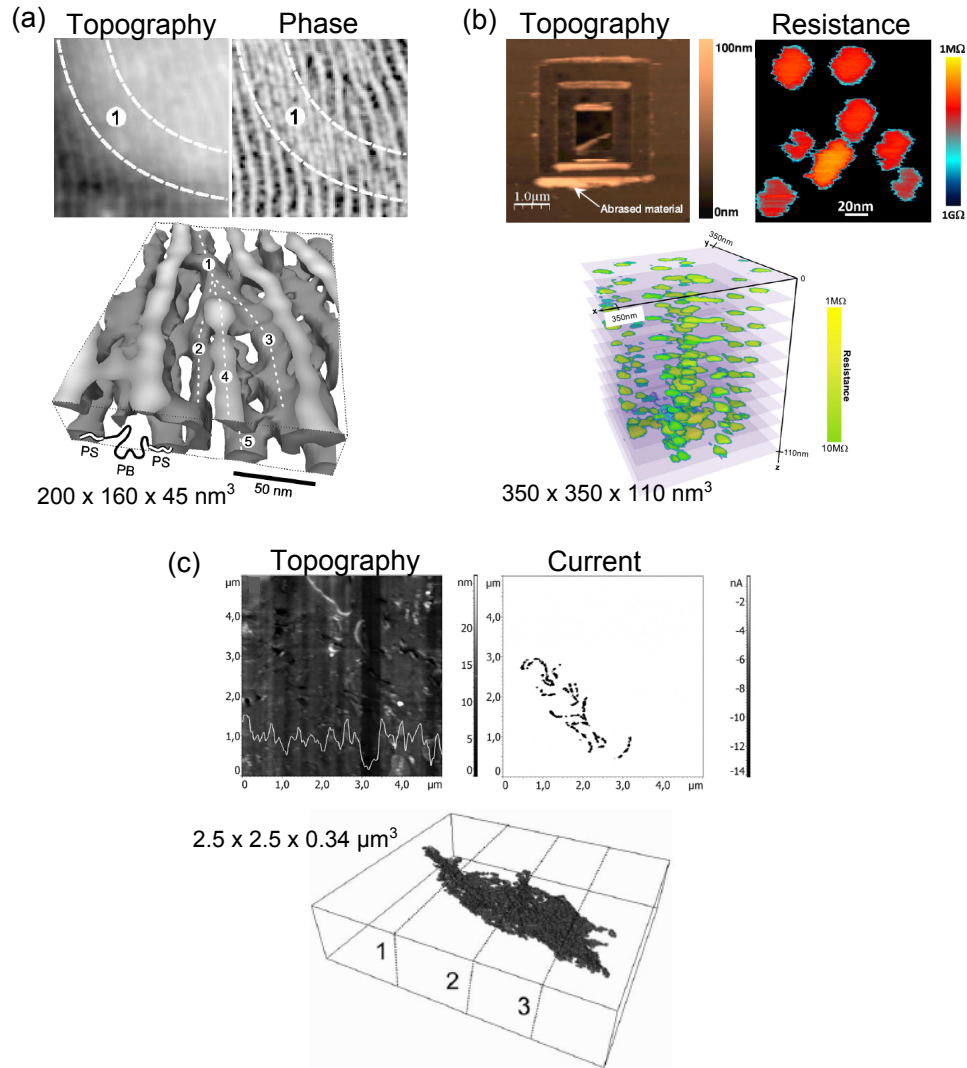
Figure 1.6. Slice-and-view approaches for subsurface imaging using AFM. (a) AM-AFM in combination with plasma etching reveals PS cylinders (bright phase contrast) formed within a SBS film (dark phase constrast) [79] Copyright (2000) by the American Physical Society. (b) Successive removal of material (crater feature) made by an ultra-sharp full diamond probe. 2D SSRM measurements shows the total resistance obtained on vertically aligned MWCNT bundles (bright, lower resistance) surrounded by oxide (dark, higher resistance). Reprinted with permission from [80]. Copyright (2012) John Wiley & Sons, Inc. (c) Ultramicrotome used in combination with C-AFM to image a conductive graphene network in a PS matrix. Reprinted with permission from [117]. Copyright (2012) John Wiley & Sons, Inc.
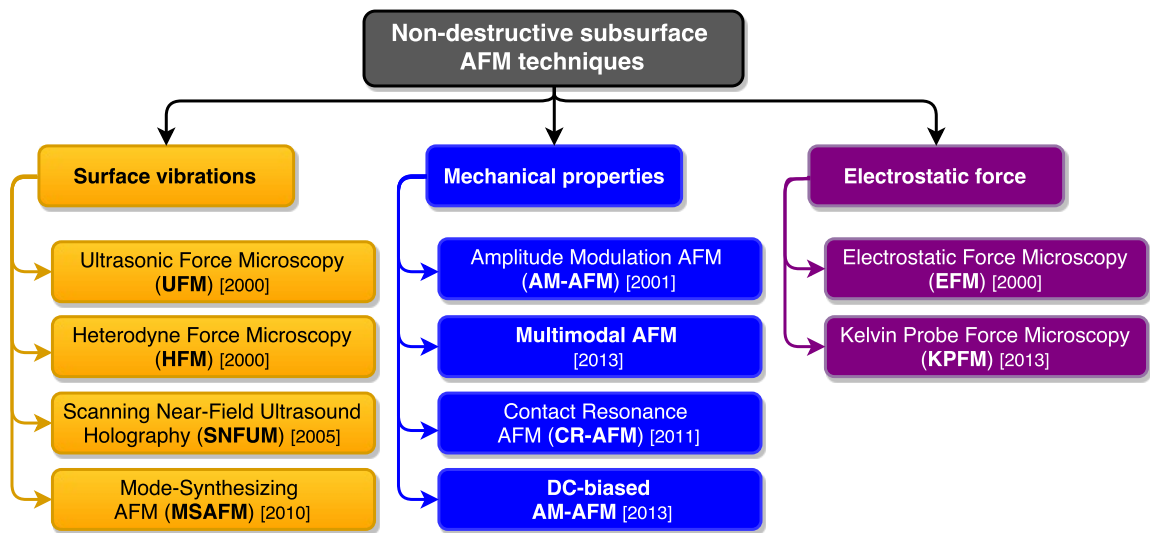
Figure 1.7. Non-destructive AFM techniques for subsurface imaging. Relevant features are the preservation of the original state of the specimen in study, no complex sample preparation and operation under a wider range of environments/media. These techniques are classified based on the mechanism of detection either surface vibrations, mechanical properties or electrostatic force interactions.

26
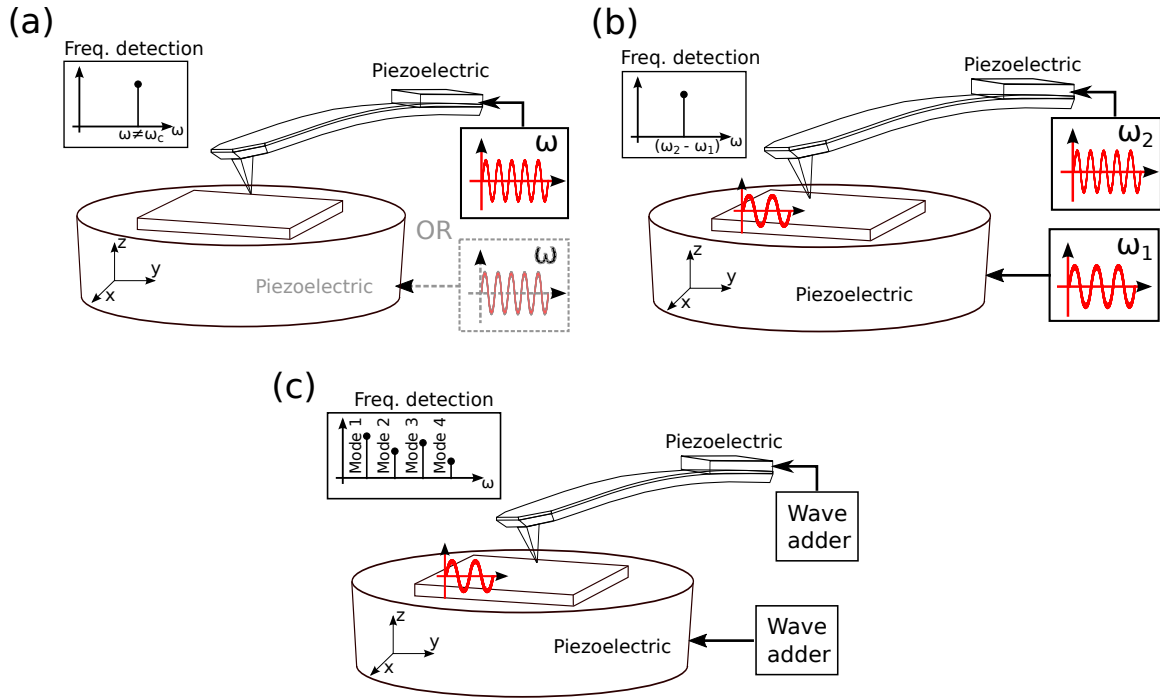
Figure 1.8. Schematic representation of techniques based on detection of surface vibrations. Ultrasound waves are launched, using an external transducer usually a piezoelectric, from the sample or via the microcantilever as in (a) UFM CR-AFM, or through both in (b) HFM and SNFUM, while the tip is in contact or near-contact with the sample. The measured frequency response is different in each case, for example, in HFM is the beat frequency $(\omega_2 - \omega_1)$. (c) In MSAFM, the probe and the sample are excited with forces containing different frequency components.
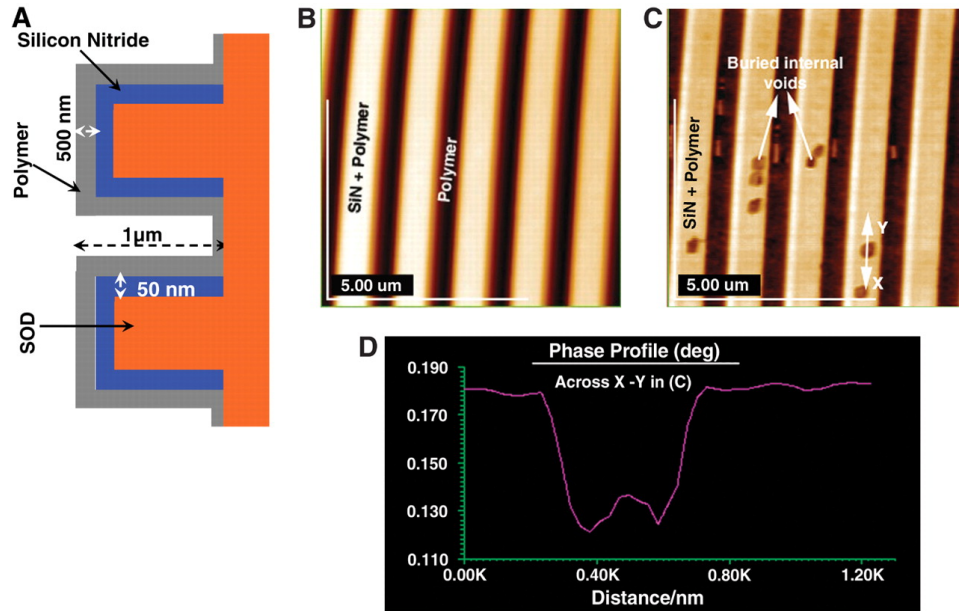
Figure 1.9.   Detection of voids/defects in trench structures using scanning near-field ultrasound holography (SNFUH). (A) Schematic representation of the sample with 1 μm deep trenches etched in SOD (spin-on-dielectric) covered by a 50 nm layer of Si_3N_4, and 500 nm of polymer (benzocyclobutene). (B) Sample topography with uniform superficial coating. (C) SNFUH phase image reveals internal voids or defects on the trenches (D) Profile across the void. From [85] Reprinted with permission from AAAS.
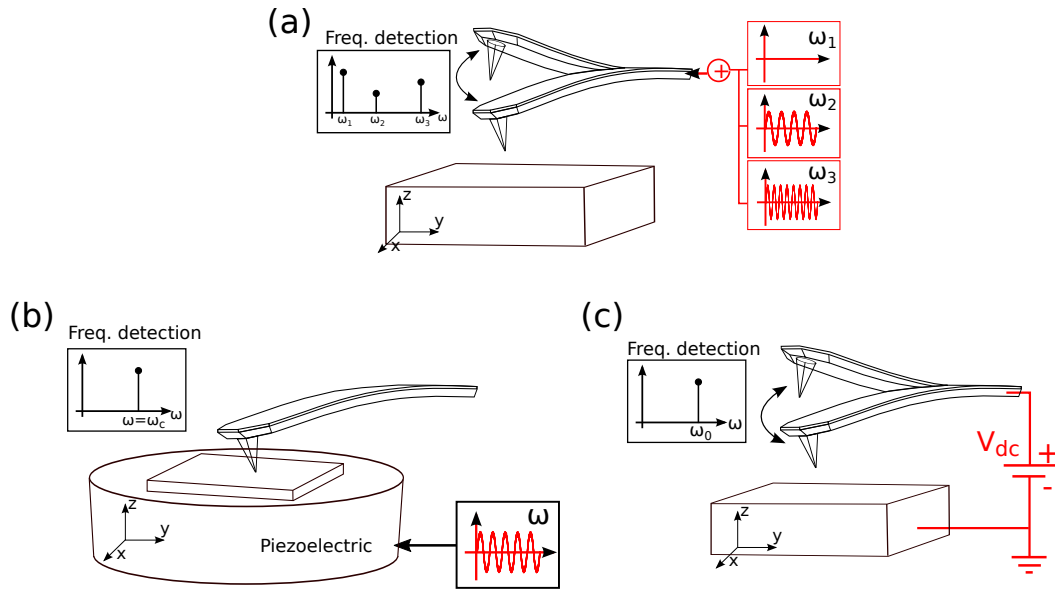
Figure 1.10. Schematic representation of techniques based on the detection of local mechanical properties. (a) In multimodal AFM there is a simultaneous excitation of the flexural modes of the microcantilever. (b) In CR-AFM, a piezoelectric at the bottom of the sample generates a wave while the tip is in contact with the sample. (c) In DC-biased AM-AFM, the microcantilever oscillates at $\omega \sim \omega_0$ while biased with a DC voltage. The measured frequency response is different in each case, for example, in the trimodal case are the frequency components equal or close to the first three of the flexural modes (ω_1, ω_2 and ω_3), in MSAFM could be any of the mixed frequencies (modes), in CR-AFM is the contact resonance frequency (ω_c) and in DC biased AM-AFM one of the flexural frequencies.
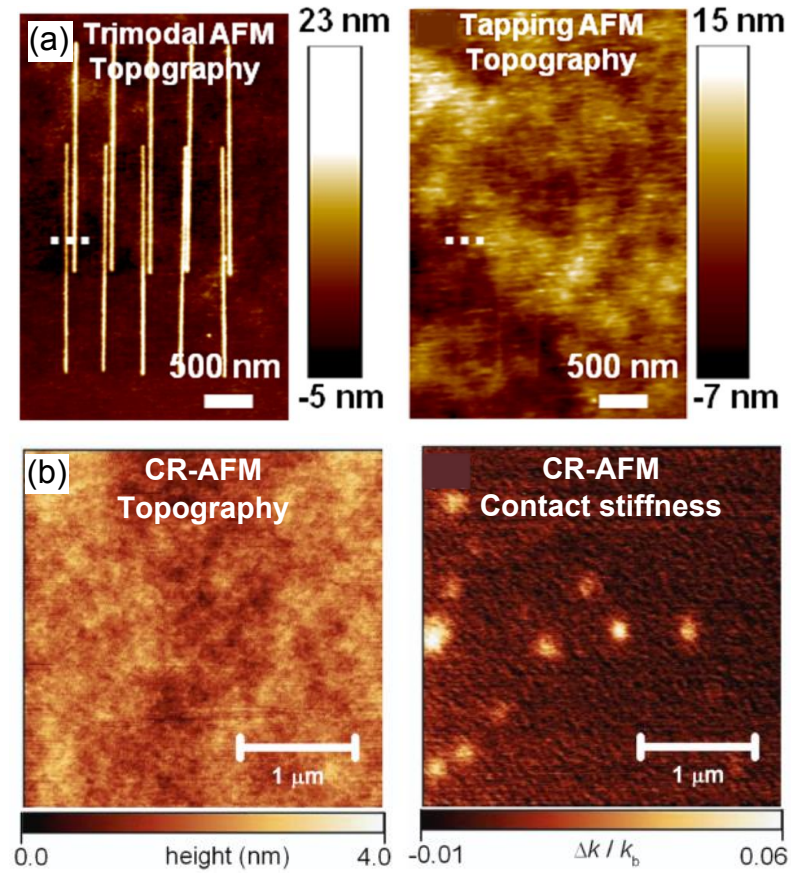
Figure 1.11. Subsurface imaging using detection of local mechanical properties. (a) Trimodal and tapping AFM images (topography) of an array of silicon nanowires buried under a 70 nm PDMS film. From [118] ©IOP Publishing. Reproduced with permission. All rights reserved. (b) Topography and contact stiffness contrast obtained using CR-AFM. Buried silica particles (50 nm size) are located under a 125 nm thick PS cover film. From [100] ©IOP Publishing. Reproduced with permission. All rights reserved.
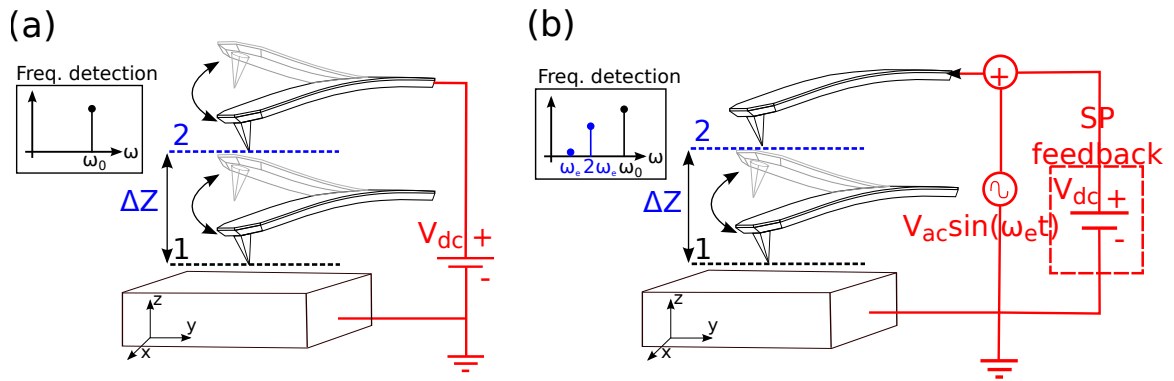
Figure 1.12. Schematic representation of AFM techniques based on the detection of electrical force interactions for subsurface imaging. The diagrams in (a) and (b) are representations of double-pass modes for EFM and KPFM, respectively. During the second pass the tip is at a lifted height ΔZ, an electrical bias is applied to the tip and the mechanical oscillation of the microcantilever is on in EFM (at $\omega \sim \omega_0$) and off in KPFM. An additional feedback loop measures the surface potential (SP) in KPFM.
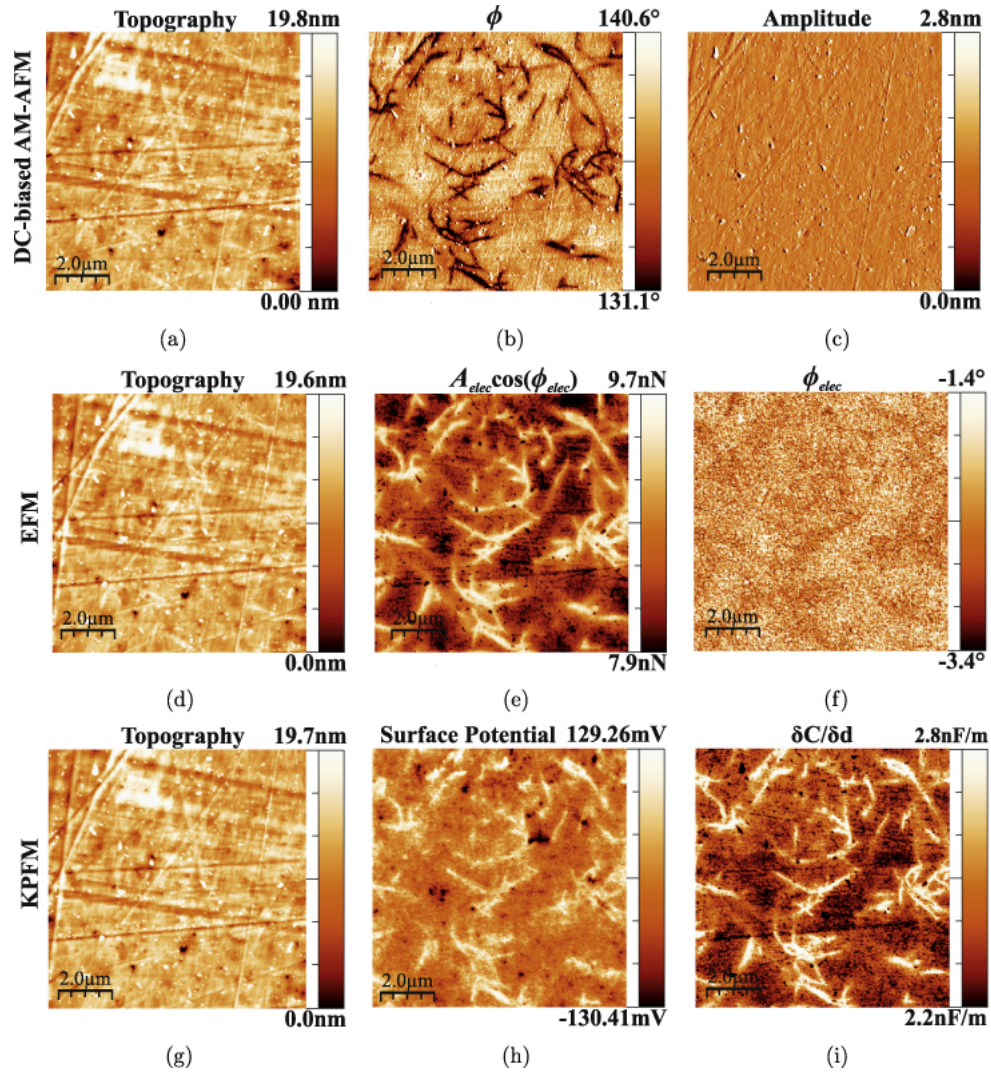
Figure 1.13. Comparison of subsurface imaging of SWCNTs in a PI composite using DC-biased AFM-AFM, EFM and KPFM. (First row) Observables from DC-biased AM-AFM: (a) Topography, (b) phase shift and (c) amplitude, with -3V applied to the tip. (Second row) Single-pass EFM observables: (d) topography, (e) amplitude component, and (f) phase. (Third row) Single-pass KPFM observables: (g) topography, (h) surface potential and (i) capacitance gradient. From [102] ©IOP Publishing. Reproduced with permission. All rights reserved.
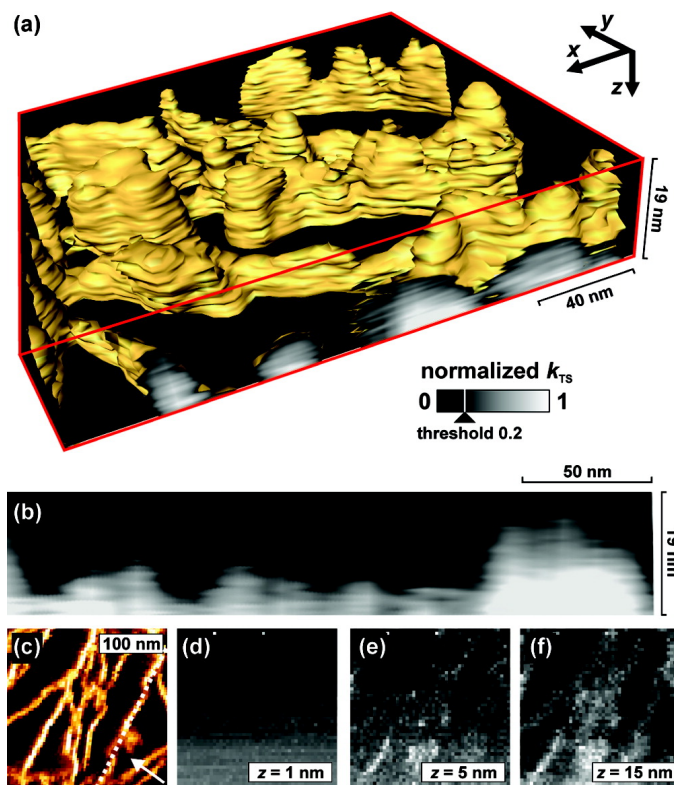
Figure 1.14. Depth resolved image of a thin film of polypropylene (PP) (a) Volume image reconstructed from k_{TS} maps. The resolved depth is 19 nm. (b) Cross-section of the lamella marked in (c), which corresponds to the phase image obtained by AFM-AFM of the region where the APD curves (50 x 50) were taken. Some k_{TS} slices are shown from (d) to (f) for three different depths. Reprinted with permission from [92]. Copyright (2013) American Chemical Society.
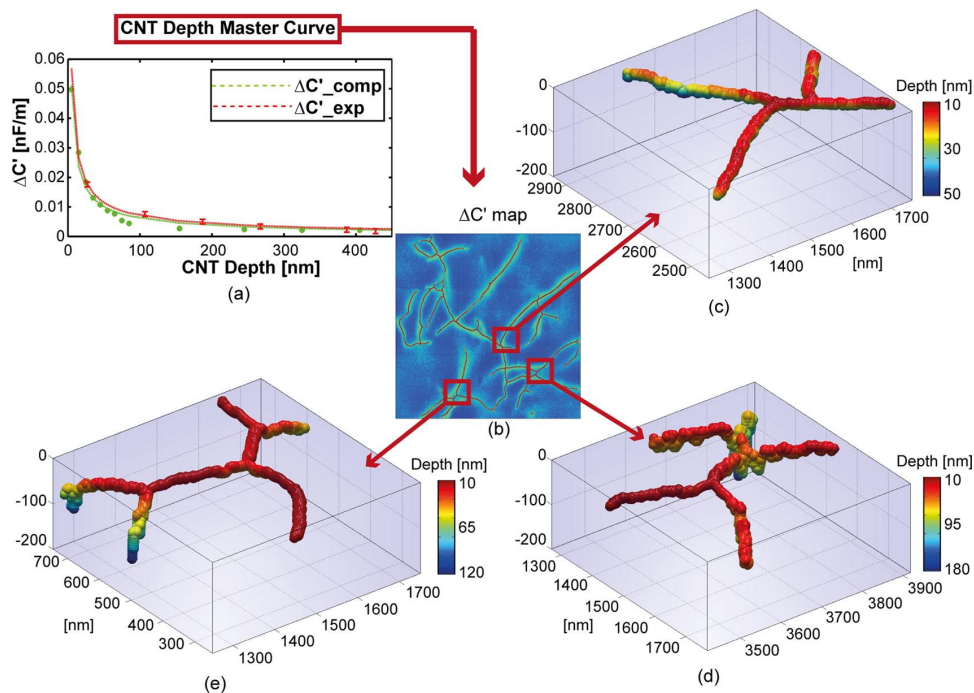
Figure 1.15. Three dimensional reconstruction of SWCNTs embedded in polyimide (PI) using 2nd-harmonic KPFM. (a) Computational and experimental capacitance gradient difference ($\Delta C' = (\partial C \partial z)_{SWCNT} - (\partial C \partial z)_{PI}$) as a function of CNT depth. (b) $\partial C \partial z$ map (5 μm x 5 μm) (c - d) Volume images of three selected SWCNTs regions (500 nm x 500 nm). Reprinted with permission from [109]. Copyright (2015) American Chemical Society.

2. RESONANCE-ENHANCED 2nd-HARMONIC KPFM FOR SUBSURFACE IMAGING

Dynamic AFM techniques based on electrostatic force sensing, such as electrostatic force microscopy (EFM) and Kelvin probe force microscopy (KPFM), have been used to detect subsurface features in a non-invasive manner [102, 109, 112, 113, 119]. In a previous study, we demonstrated the advantages of KPFM as a robust quantitative subsurface technique when compared to EFM [102]. KPFM is known as a technique to measure the local contact potential difference (CPD) between the tip and the sample at nanoscale [107, 120]. However, it also provides a 2nd-harmonic channel largely sensitive to the dielectric properties or charge distribution on or below the surface [121–123]. Due to its quantitative character and dependence on sample properties, it opens up the possibility to convert additional KPFM observables into physical quantities, especially for subsurface imaging. All prior works using KPFM 2nd-harmonic for subsurface imaging [102,109] have done so with off-resonance electrostatic excitation. While resonance-enhanced 2nd-harmonic imaging has been proposed earlier in the context of dielectric mapping [104, 124–126], the benefits for subsurface imaging remain unexplored.

This chapter contains a comprehensive analysis on 2nd-harmonic KPFM, using resonance-enhanced detection for subsurface imaging. This scheme takes advantages of the microcantilever dynamics and its maximized response at resonance. The 2nd-harmonic channel is set at one of the frequencies of the available flexural modes of the microcantilever. Theoretical considerations are provided for the electrostatic force interaction generated at a potential difference between the probe and the sample, as well as a model to describe the microcantilever dynamics when it is directly excited by an external electrostatic force. The technique is used in the observation of buried 0D, 1D and 2D objects in three types of polymer composites. Lastly, a finite ele-

ment model is used to analyze material contrast, depth and lateral resolution of the technique.

2.1 Theory

2.1.1 Microcantilever Dynamics in Double-Pass KPFM

KPFM belongs to the family of dynamic AFM techniques based on electrostatic force detection. It draws upon the macroscopic Kelvin probe method invented to measure the work function of metals and semiconductors [127], and later adapted to the sub-micron scale in 1991 [107]. In KPFM, the response of an electrically biased microcantilever accounts for electrostatic force interactions, generated by an external electric field applied between the AFM probe and sample. The detection is further improved by using resonance-enhanced mode, which relies on the microcantilever response at resonance, to improve material contrast and sensitivity.

In dynamic AFM, the microcantilever exhibits several eigenmodes of vibration and the intention is to drive the microcantilever at resonance [128]. Particularly, resonance-enhanced KPFM uses one of the flexural or bending modes, which are transverse to the plane of the microcantilever. Each bending mode has its own resonance frequency and can be determined using the Euler Bernoulli beam theory. The partial differential equation describing the motion of a thin rectangular microcantilever is

$$EI\frac{\partial^4 w(x,t)}{\partial x^4} + c^*\frac{\partial w(x,t)}{\partial t} + \rho A\frac{\partial^2 w(x,t)}{\partial t^2} = F_{drive}(x,t) \qquad (2.1)$$

where EI, $w(x,t)$, c*, ρ, A and $F_{drive}(t)$ are the flexural rigidity, transverse deflection, damping, mass density, cross-sectional area and driving (excitation) force, respectively. F_{drive} in this case refers to the electrostatic force, which is presently approximated as a point force applied at the end of the microcantilever, where the tip is located. Therefore, $F(t)_{drive}$ is equal to $F\delta(x-L)$, where δ is the Dirac delta function.

Equation (2.1) is discretized using Galerkin's method [129]. This approach assumes a solution in the form

$$w(x,t) = \sum_{j=1}^{\infty} \psi_j(x) q_j(t),$$ (2.2)

where $\psi_j(x)$ is the ith microcantilever eigenmode function and $q_j(t)$ is a modal co-ordinate. Each $\psi_j(x)$ is normalized so that $\psi_j(L) = 1$, so that $q_j(t)$ corresponds to the deflection of the microcantilever at the location of the tip [130, 131]. A detailed derivation is given in Appendix A.1. Using the discretization, Equation (2.1) can be simplified into the following ordinary differential equations for $i = 1, 2, ..., N$,

$$\frac{1}{\omega_i^2} \frac{d^2 q_i(t)}{dt^2} + \frac{1}{\omega_i Q_i} \frac{dq_i(t)}{dt} + q_i(t) = \frac{F_i(t)}{k_i},$$ (2.3)

where ω_i, Q_i, k_i, and $F_i(t)$, are the bending resonance frequency, quality factor, equivalent stiffness, and modal forcing of the ith eigenmode, respectively. Furthermore, the microcantilever-sample capacitance can be discretized in terms of the modal coordinates such that $C(Z, q_1, q_2, ..., q_N)$, where Z is the separation between the non-vibrating microcantilever tip and the sample.

In a microcantilever-sample system, considered as a small vibrating capacitor, the modal electrostatic excitation (driving) force $F_i(t)$ in the vertical z direction, is given by

$$F_i(t) = -\frac{\partial U}{\partial q_i} = -\frac{1}{2} \left| \frac{\partial C}{\partial q_i} \right| (\Delta V(t))^2,$$ (2.4)

where U is the stored energy, $\partial C / \partial q_i$ is the capacitance gradient with respect to the modal contribution to Z. ΔV is the potential difference, composed of an ac voltage with amplitude V_{ac} and frequency ω_e, a dc voltage V_{dc}, and the contact potential difference between the tip and the sample V_{cpd}. Both V_{dc} and V_{ac} are applied to the conductive microcantilever, and typically are in the order of few volts (1-3 V). Expanding Equation (2.4), three separate contributions are found for $F_i(t)$ as [104]

$$F_i(t) = F_{i,dc} + F_{i,\omega_e}(t) + F_{i,2\omega_e}(t), \qquad (2.5)$$

$$F_{i,dc} = -\left|\frac{\partial C}{\partial q_i}\right| \left[\frac{1}{2}(V_{dc} - V_{cp})^2 + \frac{V_{ac}^2}{4}\right], \qquad (2.6)$$

$$F_{i,\omega_e}(t) = -\left|\frac{\partial C}{\partial q_i}\right| (V_{dc} - V_{cp})V_{ac}\sin(\omega_e t), \qquad (2.7)$$

$$F_{i,2\omega_e}(t) = \frac{1}{4}\left|\frac{\partial C}{\partial q_i}\right| V_{ac}^2\cos(2\omega_e t). \qquad (2.8)$$

where $F_{i,dc}$, F_{i,ω_e} and $F_{i,2\omega_e}$ correspond to the DC, ω_e and $2\omega_e$ components of the modal electrostatic force.

KPFM has two main working modes, namely amplitude modulation (AM-) or frequency modulation (FM-) KPFM. AM-KPFM is based on the electrostatic force given in Equation (2.4), and the induced microcantilever amplitude response. FM-KPFM draws upon the gradient of the electrostatic force and the resulting shifts on the microcantilever oscillation frequency of the chosen eigenmode. Therefore, [132]

$$\Delta f_i(z, \omega_e) \propto \frac{\partial F_{i,\omega_e}}{\partial q_i} = \frac{\partial^2 C}{\partial q_i^2}(V_{dc} - V_{cpd})V_{ac}\sin(\omega_e t). \qquad (2.9)$$

FM-KPFM is mostly implemented under ultra high vacuum (UHV) conditions to estimate the work function of materials, especially when absolute values are required [132, 133]. Conversely, AM-KPFM is commonly operated under ambient conditions and its implementation is relatively easier compared to FM-KPFM, so it is feasible in most commercial AFMs.

Both AM- and FM-KPFM can be implemented in two schemes, namely, single-pass and double-pass. In single-pass, measurements of surface topography and the microcantilever response to the electrostatic forces are performed simultaneously [103, 125]. Double-pass differs from single-pass in that two scans are performed. The first records the surface topography and the second senses the electrostatic interactions at a preset height offset above the surface. Therefore, in double-pass, the frequency of $F_{i,2\omega_e}$ can be tuned to one particular eigenmode, so that only one of N are in the response. Then, the equation of motion reduces to a one degree of freedom model

(Equation (2.3)). Henceforth the modal coordinate of the one chosen eigenmode, $i = 1$ or $i = 2$, in double-pass KPFM will be denoted simply as "q". In this work, we use AM-KPFM in double pass mode, focusing on the $F_{i,2\omega_e}$ component, hereafter referred as 2nd-harmonic KPFM or KPFM for brevity.

Traditionally, KPFM has been used to map the contact potential difference (CPD), while the tip scans the sample surface. This is achieved by recording the V_{dc} voltage that nulls the microcantilever oscillation at ω_e (Equation (2.7)). The CPD is proportional to the work function in metals or semiconductors ($V_{cpd} = \frac{\Phi_{sample} - \Phi_{tip}}{e}$), local charges in insulators and voltage drops in a biased circuit [134].

The $2\omega_e$ component, namely 2nd-harmonic channel, depends on the electrical properties of the sample and the microcantilever-sample geometry. It determines the variation of the capacitance with respect to the tip-sample distance. In early days, before KPFM was formally introduced as a technique, the $2\omega_e$ channel was already being used to study surface dielectric properties as well as dopant concentration in semiconductors [125, 126].

In double-pass resonance-enhanced KPFM, the microcantilever response at $2\omega_e$, using the first flexural microcantilever eigenmode ($i = 1$), can be obtained by the steady state solution of the single degree of freedom point mass-model given in Equation (2.3). Letting $q_p(t) = A_{1,2\omega_e}\sin(2\omega_e t - \Psi_{2\omega_e})$,

$$
\begin{aligned}
A_{1,2\omega_e} &= \frac{|F_{1,2\omega_e}|}{k_1}\sqrt{\frac{1}{(1 - r^2)^2 + (r/Q_1)^2}}, &&(2.10)\\
&= \frac{|F_{1,2\omega_e}|}{k_1}|H_{1,2\omega_e}|,
\end{aligned}
$$

where $r = \frac{2\omega_e}{\omega_1}$. $|H_{1,2\omega_e}|$, $A_{1,2\omega_e}$ and $\Psi_{1,2\omega_e}$ are the magnitude of the microcantilever transfer function, the amplitude and phase response at $2\omega_e$, respectively [124]. Assuming $\omega_e = \omega_1/2$, the amplitude response at $2\omega_e$ simplifies to

$$
A_{1,2\omega_e} = \frac{Q_1}{k_1}F_{1,2\omega_e}. \qquad (2.11)
$$

The above equation shows the dependence of $A_{2\omega_e}$ on the ratio Q/k. Furthermore, using Equations (2.8) and (2.11), we can relate the 2nd-harmonic of the electrostatic force to the experimental $A_{2\omega_e}$ and find an analytical relation for $\partial C/\partial q_1$ as

$$\frac{\partial C}{\partial q_1} = \frac{4k_1 A_{1,2\omega_e}}{V_{ac}^2 |H_{1,2\omega_e}|}. \tag{2.12}$$

The measured phase is given by $\Psi_{1,2\omega_e} = \phi_{1,2\omega_e} + \phi_{1,2} + \phi_{inst}$, where $\phi_{1,2\omega_e}$ is the phase due to the electric properties of the sample, $\phi_{1,2}$ is the phase lag due to microcantilever dynamics $\left(\phi_{1,2} = tan^{-1}\left(\frac{r}{Q_1(1-r^2)}\right)\right)$ and ϕ_{inst} is an instrumental phase shift introduced by the electronics. For the purposes of this work, we mainly use $A_{1,2\omega_e}$ (amplitude channel), but $\Psi_{1,2\omega_e}$ has been employed elsewhere to study the real and imaginary components of $\partial C/\partial q_1$ related to complex dielectric properties [65].

2.1.2   Electrostatic Force Calculation Using Finite Element Analysis

The 2nd-harmonic channel is useful in the detection of subsurface features, being sensitive to changes in the electrostatic force interactions caused by variation of the local capacitance gradient. Buried objects with different dielectric properties compared to the surrounding media, perturb the electric field applied between the tip and the sample, affecting the electrostatic interactions. Also, there are contributions from the geometry of the probe and sample that must be considered, due to the long-range nature of the electrostatic force.

Within this framework, three relevant questions arise for subsurface imaging applications: what is the material contrast resolution, how deep a buried object can be detected (depth sensitivity), and what is the spatial (lateral) resolution. In order to answer those questions, we need a model, considering the properties of the probe-sample system. One of the main challenges in modeling long-range electrostatic interactions is the shape of the probe and the complexity of sample properties, particularly when dealing with heterogeneous materials. A typical probe is composed of a microcantilever (beam), and a conical (or pyramidal) tip ending in an spherical apex. Some analytical models have been derived for homogeneous substrates, such as

a flat conductor [135–137], a semiconductor [138] or a thin dielectric [139,140]. These studies have shown that the electrostatic force between the tip and the sample is not confined at the very end of the tip but rather it is the sum of the contributions from the spherical apex, the conical side faces and the distal end of the microcantilever. The dominant part depends on the relation between tip-sample gap with respect to the tip radius and length [135, 140].

In the case of heterogeneous materials with buried objects within a matrix or thick dielectrics, there is a lack of accurate analytical models. Therefore, numerical or finite element analyses have been proposed to compute the electrostatic force interaction between a conductive probe and more complex samples. For instance, numerical simulations of the equivalent charge method are used for point charges embedded in a dielectric matrix [141,142] or finite element modeling in the case of uncharged/charged buried nanoparticles [143], or CNT bundles [109] embedded in a polymer matrix.

Here, a 3D finite element model is built in Comsol Multiphysics using the electrostatics interface. Within the model, it is relevant to consider the contributions of all parts of the probe, i.e. the micrometric sized cone and microcantilever and the nanometric sized tip apex [**?**, 144]. The tip of the probe is modeled as a hemisphere (apex) with radius r_t attached to a cone with a half angle θ and height h_t. The distal end of the microcantilever is modeled as a disk of radius r_c and thickness t_c, as shown in figure 2.2(a). In consideration of the type of samples used in this study, we model the sample as a matrix (block) with a dielectric constant ϵ_m, and a filler (cylinder or sphere) with a dielectric constant ϵ_f. For conductive materials, such as CNTs, we assume a floating potential boundary condition on its surface, not necessarily grounded. The surrounding air is defined as an infinite element domain. Note: the 3D model can be simplified computationally by exploiting symmetries. For instance, a 2D axisymmetric model is suitable in the case of an axisymmetric tip and a 0D subsurface object, when the latter is aligned with the tip. In case of asymmetry with one of the axis, the mirror symmetry of the 3D model can be invoked to mesh only half of the volume.

To compute the electrostatic force, the boundary problem is defined by the following conditions: a constant electric potential applied to the probe (V_t), a constant electric potential at the bottom surface of the sample (0 V, ground), zero charge ($\mathbf{n} \cdot \mathbf{D} = 0$) in the air domain surrounding the probe and the sample and charge conservation enforced everywhere. An example of the electric potential distribution with $V_t = 1V$ is shown in figure 2.2(b), using a 2D surface plot of the y-z plane. The electrostatic force on an arbitrary charge distribution with a volume V having a position dependent charge density $\rho(x, y, z)$ is given by

$$\mathbf{F} = \int_V \rho \mathbf{E} dV, \tag{2.13}$$

where $dV = dxdydz$ is the volume element. Defining the force per unit volume $\mathbf{f} = \rho \mathbf{E}$, it can be shown that

$$\mathbf{f} = \epsilon_0 \left[(\nabla \cdot \mathbf{E})\mathbf{E} + (\mathbf{E} \cdot \nabla)\mathbf{E} \right] - \frac{1}{2}\nabla(\epsilon_0 E^2). \tag{2.14}$$

Comsol uses the Maxwell stress tensor ($\mathbf{T}$) to compute $\mathbf{F}$, which simplifies the computation of the volume integral. $\mathbf{T}$ is defined as [145]

$$\mathbf{T} = T_{ij} \equiv \epsilon_0 \left(E_i E_j - \frac{1}{2}\delta_{ij} E^2 \right), \tag{2.15}$$

where the indices i, j refer to the coordinates x, y, z and E_i, E_j are the components of the electric field. It can be shown that

$$(\nabla \cdot \mathbf{T})_{,j} = \epsilon_0 \left[(\nabla \cdot \mathbf{E})E_j + (\mathbf{E} \cdot \nabla)E_j \right] - \frac{1}{2}\nabla_j(E^2). \tag{2.16}$$

Equations (2.16) and (2.14) imply that the force per unit volume can be written as $\mathbf{f} = (\nabla \cdot \mathbf{T})$. Therefore, the force $\mathbf{F}$ on an arbitrary charge distribution is given by

$$\mathbf{F} = \int_V (\nabla \cdot \mathbf{T}) dV. \tag{2.17}$$

Using the divergence theorem, Equation (2.17) is equal to

$$\mathbf{F} = \oint_S \mathbf{T} \cdot d\mathbf{s}, \tag{2.18}$$

which means that instead of solving the volume integral given in Equation (2.13), the force is calculated by a surface integral over an arbitrary surface (Equation (2.18)). Physically, $\mathbf{T}$ represents the traction force per unit area acting on the surface S. Thus T_{xx}, T_{yy}, T_{zz} represent normal stresses and T_{xy}, T_{xz}, etc. represent shear stresses respectively acting along xy, yz and xz planes. A more detailed explanations is given in Appendix A.2.

The computational model allows the estimation of the electrostatic force in different scenarios, for example, changing the dielectric constant, geometry or depth of the embedded object. This is a useful approach to estimate material contrast, depth and lateral resolution.

One of the criteria to determine the limits of the experimental subsurface detection is the force sensitivity, i.e. the minimum detectable force. This is determined by the noise, mainly the thermal noise of the microcantilever (η_{th}) and the detector noise of the AFM [146]. The thermal noise can be estimated from the microcantilever oscillations in a thermal bath, as follows. From the fluctuation dissipation theorem, the power spectral density can be calculated as

$$S(\omega) = \frac{2k_B T}{\omega_1}\text{Im}(\chi(\omega)) \tag{2.19}$$

where k_B is the Boltzmann constant, T is the room temperature and $\chi(\omega)$ is the microcantilever transfer function relating the tip motion to the input force. For a single degree of freedom oscillator,

$$S(\omega) = \frac{2k_B T}{\pi k \omega_1 Q_1} \frac{1}{(1 - (\omega/\omega_1)^2)^2 + \omega^2/(\omega_1 Q_1)^2}. \tag{2.20}$$

$S(\omega)$ is related to the thermal noise by [147]

$$\eta_{th}^2 = \int_0^\infty S(\omega)d\omega. \tag{2.21}$$

To calculate η_{th} for the resonance and off resonance case, we integrate Equation (2.21) over a frequency bandwidth range ($B = 1$ kHz), in which the experiments are performed. Using $\omega_1 = 68.3$ kHz, $Q = 120.4$, $k = 2.37$ N/m, $T = 293$ K, $\eta_{th} = 37.5$

pm when $\omega = \omega_1$. If $\omega < \omega_1$ (20 kHz), $\eta_t h = 0.56$ pm. These values are used to calculate $F_{\min,\text{th}}$ given by

$$F_{\min,th} = \frac{k_1 \eta_{th}}{|H_{1,2\omega_e}|} \tag{2.22}$$

The detector noise is determined mainly by the optical beam deflection sensor noise density (η_{obd}) of the AFM system. In Cypher AFM (Asylum Research) from Asylum Research used throughout this work, $\eta_{obd} \approx 25 \text{fm}/\text{Hz}^{1/2}$. Then, the minimum detectable force due to η_{obd} is given by

$$F_{\min,obd} = \begin{cases} \dfrac{\eta_{obd}\sqrt{B}k_1}{Q_1} & 2\omega_e = \omega_1, \\[2ex] \eta_{obd}\sqrt{B}k_1 & 2\omega_e \ll \omega_1. \end{cases} \tag{2.23}$$

$F_{\min}^{obd}$ is frequency dependent and is lower (higher sensitivity) at resonance than off-resonance. The minimum total force is obtained as

$$F_{\min} = \sqrt{(F_{\min,\text{th}})^2 + (F_{\min,\text{obd}})^2}. \tag{2.24}$$

Using typical values for a conductive microcantilever used during experiments, $\omega_1 = 77.1$kHz, $k_1 = 2.3$ N/m, and $Q_1 = 232$, at room temperature and $B = 1$kHz, Fmin is equal to 0.82 pN and 2.0 pN when $2\omega_e$ is at ω_1 and off-resonance, respectively.

2.2 Experimental Setup

In double-pass mode, two scans per line are performed on a selected sample location. As shown in figure 2.1, during the first pass, the AC deflection of the microcantilever is sensed by Lock-in A, whose reference is set to ω_m, approximately equal to one of the frequencies of the flexural eigenmodes of the microcantilever (typically ω_1). Lock-in A tracks the topography by controlling the amplitude of the microcantilever oscillation in non-contact (or tapping) mode, while it keeps constant the distance between the tip and the sample. During the second pass, the tip is raised to a lift-height (ΔZ) above the sample, the mechanical oscillation is turned off and an electrical excitation at a frequency ω_e and amplitude V_{ac} is applied to the tip. The microcantilever

response to the electrostatic interactions at ω_e and $2\omega_e$ are captured by Lock-in B and Lock-in C, respectively. Additionally, a feedback loop constituted by a KPFM servo, is used to apply V_{dc} to nullify the amplitude response to F_{ω_e} (Equation (2.7)). The latter is used in the common application of KPFM for surface potential measurements. The main observables are the topography from the 1$^{\text{st}}$-pass and the amplitude $(A_{2\omega_e})$ and phase $(\Psi_{2\omega_e})$ corresponding to the microcantilever response from the 2$^{\text{nd}}$-pass. This is the mode used in this work. Single-pass differs from double pass in that measurements of surface topography and the microcantilever response to the electrostatic forces are performed simultaneously, usually in non-contact mode [103, 125].

Double-pass is advantageous for the resonance-enhanced mode. The same eigenmode frequency can be used for the mechanical and electrical driving forces, since they are not simultaneously applied as required in single-pass. Therefore, during the first pass, ω_m is set near to the first resonance frequency ω_1, and in the second pass, ω_e is adjusted close to $\omega_1/2$. Detection at resonance has been used to improve resolution in CPD measurements under vacuum conditions, using the second oscillation mode instead $(\omega_e = \omega_2)$. This is done taking advantage of a high Q achieved in vacuum due to reduction in damping [148, 149]. However, in air it is better to use the first oscillation mode for the electrical excitation, as discussed below.

Experiments were performed using the Cypher AFM at room temperature with the AFM chamber back-filled with flowing dry nitrogen. We use metallic coated silicon probes (PPP-EFM), with a nominal length and width of 225 μm and 28 μm, respectively. The tip has a height of 10 - 15 μm, a pyramidal apex angle of 25° and a tip apex radius of approx. 25 nm.

2.3 Results and Discussion

2.3.1 Resonance-Enhanced Subsurface Imaging

The capability of resonance-enhanced 2$^{\text{nd}}$-harmonic KPFM for high resolution subsurface imaging is demonstrated for three types of polymer nanocomposites. These

composites differ from each other by the morphology of the filler, i.e. 0D (nanospheres), 1D (nanotubes) or 2D (platelets). Representative results using double-pass mode are shown in figure 2.3. The first sample (figure 2.3(a, b)) corresponds to a 10 wt% barium titanate (BaTiO$_3$)-polydimethylsiloxane (PDMS) composite. The embedded BaTiO$_3$ nanoparticles (NPs), which can not be distinguished in the surface (figure 2.3(a)), are clearly revealed in the $A_{2\omega_e}$ map (figure 2.3(b)). The NPs have an average size of 100 ± 15nm, during fabrication they were aligned through the volume of the PDMS matrix by electrophoresis [150]. The second sample is a 3 wt % SWCNTs-PI film. Buried SWCNTs are seen in the $A_{2\omega_e}$ map (figure 2.3(d)), but not detectable in the topography (figure 2.3(c)). This composite is above the percolation threshold, so it is expected to contain networks of well-dispersed CNTs [43]. The third sample is a 0.25 wt % reduced graphene oxide (RGO)-polystyrene composite (PS), made by chemical reduction method [151]. The appearance of RGO flakes as crumpled or folded structures as seen in $A_{2\omega_e}$ map (figure 2.3(f)) is expected. As in the other cases, the flakes do not appear in the topography image (figure 2.3(e)). Table 2.1 presents a summary of these samples.

Resonance-enhanced detection significantly improves image contrast when compared to the off-resonance case. This is demonstrated using double-pass mode in one of the composite samples. Figure 2.4 indicates the results obtained using double-pass in the BaTiO$_3$-PDMS composite. As shown in table 2.2, we chose ω_m to be equal to ω_1, for the first pass in which the topography map (figure 2.4(a)) is acquired. For the second pass, the two cases of resonance-enhanced can be performed when $2\omega_e$ is equal or close to ω_1 (figure 2.4(b)) or ω_2 (figure 2.4(c)). Figure 2.4(d) shows the off-resonance case ($2\omega_e < \omega_1$). The maps were taken with the same voltage applied between the tip and the sample ($V_{ac} = 4$V). A clear subsurface contrast is observed in the resonance-enhanced modes for both observables ($A_{2\omega_e}$ and $\Psi_{2\omega_e}$). The amplitude response being higher when $2\omega_e = \omega_1$ (figure 2.4(b)). This result reflects the dependence of $A_{2\omega_e}$ on the ratio between Q and k (Equation (2.11)), which decreases with higher eigenmodes. These values vary depending on the mode shape of the microcan-

tilever [152, 153]. For instance, approximating a real microcantilever to a rectangular beam without a tip in air, $Q_2 = 6.27Q_1$ while $k_2 = 39.31k_1$[1]. Therefore, $(\frac{Q_1}{k_1}) > (\frac{Q_2}{k_2})$ and the amplitude response is reduced when the frequency of the 2nd flexural mode of the microcantilever is used as $2\omega_e$.

In comparison to resonance-enhanced subsurface detection, the traditional off-resonance methods are not so good. Under the same conditions of tip voltage and tip-sample distance, the two observables $A_{2\omega_e}$ and $\Phi_{2\omega_e}$ exhibit a weak or lack of contrast, as shown in figure 2.4(c). This implies the need to increase the voltage applied between the tip and the sample.

A main advantage of using resonance-enhanced detection is a higher force sensitivity, while decreasing the magnitude of the bias voltage applied between the tip and the sample. This is convenient to avoid charging or damage of samples susceptible to higher voltages [154] and reduces the constant electrostatic background in topography by F_{dc} (Equation (2.6)). Furthermore, the tip can be brought closer to the surface of the sample in the second pass, which gives better lateral resolution. The latter due to the dominant contribution from the apex at lower Z. Also, we get a better contrast resolution.

For a quantitative assessment on contrast resolution (image quality) as a function of frequency, we use as a metric the contrast-to-noise ratio (CNR) defined as [155, 156]

$$CNR = \frac{\mu_0 - \mu_B}{\sigma_B}, \tag{2.25}$$

$$CNR_n = \frac{CNR - \min(CNR)}{\max(CNR) - \min(CNR)}, \tag{2.26}$$

where μ_f and μ_m correspond to the mean $A_{2\omega_e}$ measured over the filler (brighter) and the mean $A_{2\omega_e}$ on the surrounding polymer matrix (darker), i.e. higher and lower amplitude response, respectively. This is analogous to the analysis of exposure images from MRI (magnetic resonance imaging) or X-ray imaging. Figures 2.5(a), (b) show subsurface images of a region in the BaTiO$_3$-PDMS sample when $2\omega_e$ is equal or lower to ω_1, respectively. From maps taken at frequencies around ω_1, the

---

[1]Indices 1 and 2 correspond to the 1st and 2nd flexural modes, respectively

normalized CNR (Equation (2.26)) was calculated as a function of frequency ($2\omega_e$), as shown in figure 2.5(c). The maximum CNR occurs at $2\omega_e = \omega_1$, as expected from the microcantilever dynamics.

2.3.2 Material Contrast, Depth and Lateral Resolution

In this section, we use the FE model built in Comsol Multiphysics to compute the electrostatic force between the AFM probe and a sample, in scenarios close to real experiments. We gain a deeper understanding on image contrast and sensitivity dependence on sample properties such as dielectric constant, geometry and depth of the embedded object. In experiments, these parameters are also influenced by the operation at resonance or off-resonance. Furthermore, we estimate the lateral resolution influenced by the long-range nature of the electrostatic force.

The subsurface maps shown in figure 2.3, corresponds to composite samples in which a filler (BaTiO$_3$ NPs, SWCNTs, or RGO flakes) with high dielectric constant is embedded within a low dielectric matrix (PDMS, PI or PS). This implies a higher $\partial C/\partial q_1$ and therefore higher $F_{q_1,2\omega_e}$ (Equation (2.8)). In terms of image contrast, this is reflected as brighter regions for the embedded object and darker for the polymer. In a first simulation, we calculate the force as function of depth (d) in the case of an embedded sphere or a cylinder, both buried into a low dielectric matrix ($\epsilon_m = 3$, typical value of low dielectric polymers), as shown in figure 2.6. We define ΔF as the difference in the force measured when the tip is over the filler (F_f) and when it is over the matrix (F_m) at a fixed tip-sample distance Z.

Figure 2.6(a) shows ΔF vs d for the case of a sphere of radius $r_f = 20$ nm. Different values of ϵ_f were assumed, 1 as if it was a void (air) to 10000. When $\epsilon_f \geq 1000$, ΔF is close to the case defining floating potential boundary conditions on the surface of the filler (conductive). Figure 2.6(b) corresponds to ΔF vs d in the case of a cylinder of fixed length ($L = 1\mu$ m) and radius ($r_f = 20$ nm). ϵ_f is varied

similar as in the case of the buried sphere. In both cases, the geometry of the probe is fixed, tip radius $r_t = 20$ nm, $V_t = 1$ V and $Z = 10$ nm.

The electrostatic force is proportional to ϵ_f. When $\epsilon_f > \epsilon_m$, ΔF is positive and brighter contrast is expected in $A_{2\omega_e}$. On the contrary, ΔF is negative when $\epsilon_f < \epsilon_m$, as in the case of a void, anticipating a darker (lower $A_{2\omega_e}$) contrast in the subsurface maps. Figures 2.6(a, b) also show the dependence of ΔF on the geometry of the embedded object, which is higher in the case of the 1D object (cylinder) compared to the 0D object (sphere).

With respect to the depth of the embedded object, higher values of ΔF are obtained when the filler is near the surface and decays with increasing d, until it gets close to zero. The latter occurs when F_f approximates F_m, in which case no contrast is expected in $A_{2\omega_e}$ and therefore, no detection of the embedded object. Figure 2.7(a) shows ΔF as a function of d for the case of a conductive 1D object, for which floating potential or ground boundary conditions are assumed. A threshold of detection is determined by the minimum detectable force [109] (F_{min}, Equation (2.24)), shown by the straight lines in figures 2.7 (a) and (b). Using resonance-enhanced with a typical conductive microcantilever $F_{min} = 0.8$ pN (orange line). The conductive 1D object ($L = 1\mu$m, $R_f = 20$nm) would be detected up to ~ 100 nm deep with $V_t = 1$V at $Z = 10$ nm or more than 600 nm if it is grounded. For off-resonance operation, $F_{min} = 2.5$ pN (green line), in which case the limit would be ~ 50 nm if the filler is not grounded. There is an increase in depth sensitivity when using resonance-enhanced detection at $2\omega_e$. The threshold varies depending on η_{obd} of the AFM and the properties of the microcantilever such as k, Q, ω_1 and the detection frequency. The depth sensitivity estimated from ΔF versus d, depends on the electrical properties and shape of the embedded object, the applied voltage (V_t), and the tip-sample distance Z.

Figure 2.7(b) shows the dependence of ΔF on V_t^2 (Equation (2.4)) and length of the influence of the size (length L) of the 1D object. From this simulation, the detection of larger objects is expected to occur first at lower voltages, while shorter

would appear at higher V_t. This is demonstrated with the experimental maps shown in figure 2.7(c-d). The images were acquired on a sample composed by a 2D CNT network grown on a silicon substrate, coated with 40 nm of polymer. At 2V, the larger CNTs under the surface start to appear in the subsurface map, but the short ones can be barely seen, contrary to when $V_t = 5$ V.

In a second simulation, we analyze the lateral resolution when the tip ($r_t = 20$ nm, $V_t = 1$ V) moves in the y direction, over an embedded 1D object ($r_f = 20$ nm, $L = 1\mu$m), located at a depth d. The results are shown in figure 2.8. From the data, we calculate the full width at half maximum (FWHM) and the minimum distance (L_s) at which two similar objects at the same d can be detected individually. For instance, figure 2.8 (b) shows the cases assuming the objects are separated at distances $L_s = n \times$FWHM, where n = 1, 2, ...N (multiple values of FWHM) obtained, for $d = 20$ nm. The FWHM obtained for $d = 20, 40$ and 60 nm are 122.6, 163.2 and 197.6 nm, respectively. This is reflected by a widening effect of the embedded object compared to its real size. Figure 2.8(c) relates ΔF as a function of the lateral separation distance between the two objects, where each point corresponds to multiples of the FWHM measured for each of the depths. Using the threshold given by the minimum detectable force, similar objects must be separated at least a distance equivalent to two times the FWHM to be detected individually ($\Delta F > 2$FWHM) for depths below 100 nm. Lateral resolution depends also on tip radius. We simulated the case in which r_t is comparable to the radius of the embedded object, at a fixed $Z = 10$ nm.

It is relevant to notice that this analysis is based on amplitude modulation KPFM (AM-KPFM), where the amplitude of the microcantilever response is proportional to the electrostatic force. The other common implementation in KPFM is based on frequency modulation (FM-KPFM), in which the frequency shift is proportional to the gradient of the electrostatic force. The latter would exhibit a different sensitivity and lateral resolution for subsurface imaging applications [132, 140, 157].

2.3.3 Additional: Single-Pass Resonance-Enhanced KPFM

In single-pass mode, using the same scheme in figure 2.1(b), the three lock-ins (A, B, C) are operated at the same time during one single scan. Same as in double-pass, Lock-in A tracks the surface topography by mechanically exciting the microcantilever at ω_m close or equal to ω_1. Lock-in B is used to electrically excite the microcantilever and detect its response, both at ω_e, which must be distinct from ω_m. Typically, ω_e is chosen within a low frequency range (5 to 20 kHz) to avoid cross-talk. Additionally, the feedback loop is in charge of CPD measurements. Lock-in C detects the microcantilever response at $2\omega_e$.

For resonance-enhanced mode, single-pass requires a bimodal scheme, i.e. a simultaneous excitation of two of the oscillation modes of the microcantilever. In this case, either ω_1 is used for the mechanical excitation and the ω_2 for the electrical excitation or viceversa.

For single-pass mode, the resonance-enhanced and off-resonance cases are presented in figure 2.9, i.e when $2\omega_e$ (figure 2.9(b)) is equal or close to ω_2 and less than ω_1 (figure 2.9(c)), respectively. Same as in double-pass mode, there is a remarkable difference in $A_{2\omega_e}$ contrast in the first case, as a result of the magnification in the amplitude response at resonance and a lack of contrast when using a lower frequency at the same applied voltage ($V_{ac} = 5$ V). A quantitative assessment of the observables would require a more careful analysis of the microcantilever dynamics.

Table 2.2 summarizes both modes for a particular case of resonance-enhanced detection, which we have implemented in this work to improve the sensitivity of the 2nd-harmonic subsurface channel.

2.4 Summary

Resonance-enhanced detection is an effective complement to 2nd-harmonic KPFM for subsurface imaging applications. Higher contrast resolution (image quality) is obtained when compared to the off-resonance case in double or single-pass modes,

and lower voltages are required for the detection of objects underneath the surface. This is convenient for materials sensitive to the application of electric potential and in turn, reduces the dc component of the electrostatic force that may affect the topography channel.

We point out that for AM-KPFM in air, it is more appropriate to use the first flexural mode of the microcantilever for two main reasons. First, the microcantilever response to $F_{2\omega_e}$ is higher when $2\omega_e = \omega_1$ and second, the microcantilever dynamics described by the point-mass model, can be used to relate the experimental observable $(A_{2\omega_e})$ to $F_{2\omega_e}$. Within the available schemes for KPFM, single and double-pass, the latter is more advantageous for resonance enhanced detection. In this mode, mechanical and electrical excitations are not mixed during scanning as in single-pass mode. For this reason, conventional single-pass uses ω_e lower than ω_1. Resonance-enhanced in single-pass requires to use the second oscillation mode, so that $2\omega_e = \omega_2$, while the microcantilever is mechanically driven at its first mode for the topography channel. The opposite situation can also be applied, in which $2\omega_e = \omega_1$ and $\omega_m = \omega_2$. However, in any case, when using the second mode, quantitative estimations require more careful considerations of the microcantilever dynamics, as well as tip-sample gaps [152].

A deeper understanding of the relevant aspects behind the technique is gained through finite element analysis. We investigate the contrast mechanism related to material properties, depth sensitivity and lateral resolution, using a model that approximates the geometry of the probe and sample properties. This type of computational approach is one of the key steps to convert KPFM into a quantitative reconstruction technique, which is further detailed in Chapter 4.
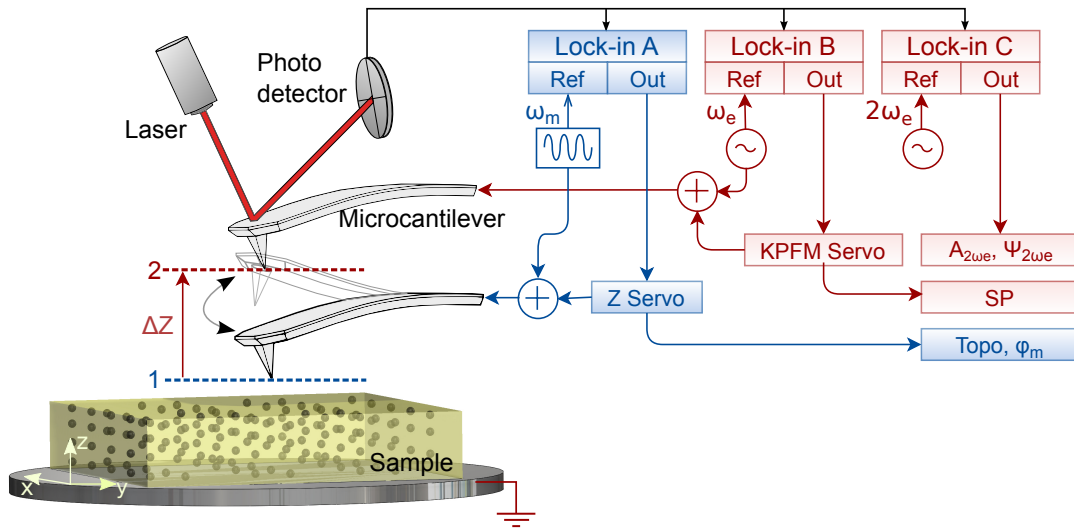
Figure 2.1. Schematic of the experimental setup in double-pass mode. Lock-in A is used to track surface topography during the first pass. Lock-ins B and C acquire the microcantilever response to the electrostatic force at ω_e and $2\omega_e$, respectively, during the second pass performed at a distance ΔZ from the sample. The relevant observables are surface topography and $A_{2\omega_e}$ for subsurface mapping.
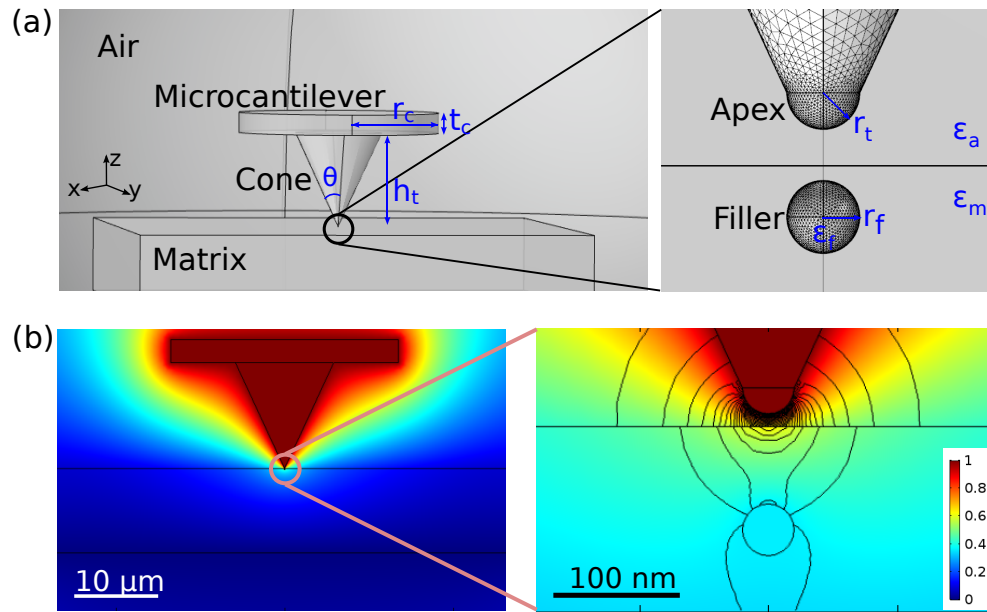
Figure 2.2. Representative plots in Comsol Multiphysics using the electrostatics interface. (a) Geometry of the 3D model corresponding to the AFM probe and sample. Zoom-in area for better visualization of nanometer sized objects, such as the tip apex and the filler). (b) 2D surface plot of the electric potential distribution, with 1V applied to the probe and bottom of the sample is grounded. The contours in the zoom-in image corresponds to the electric field lines. Floating potential boundary conditions are defined to the embedded object 60 nm deep. Geometric parameters: $r_t = 20$ nm, $h_t = 12.5$ μm, $\theta = 25°$, $r_c = 14$ μm, $t_c = 3$ μm, $Z = 10$ nm.
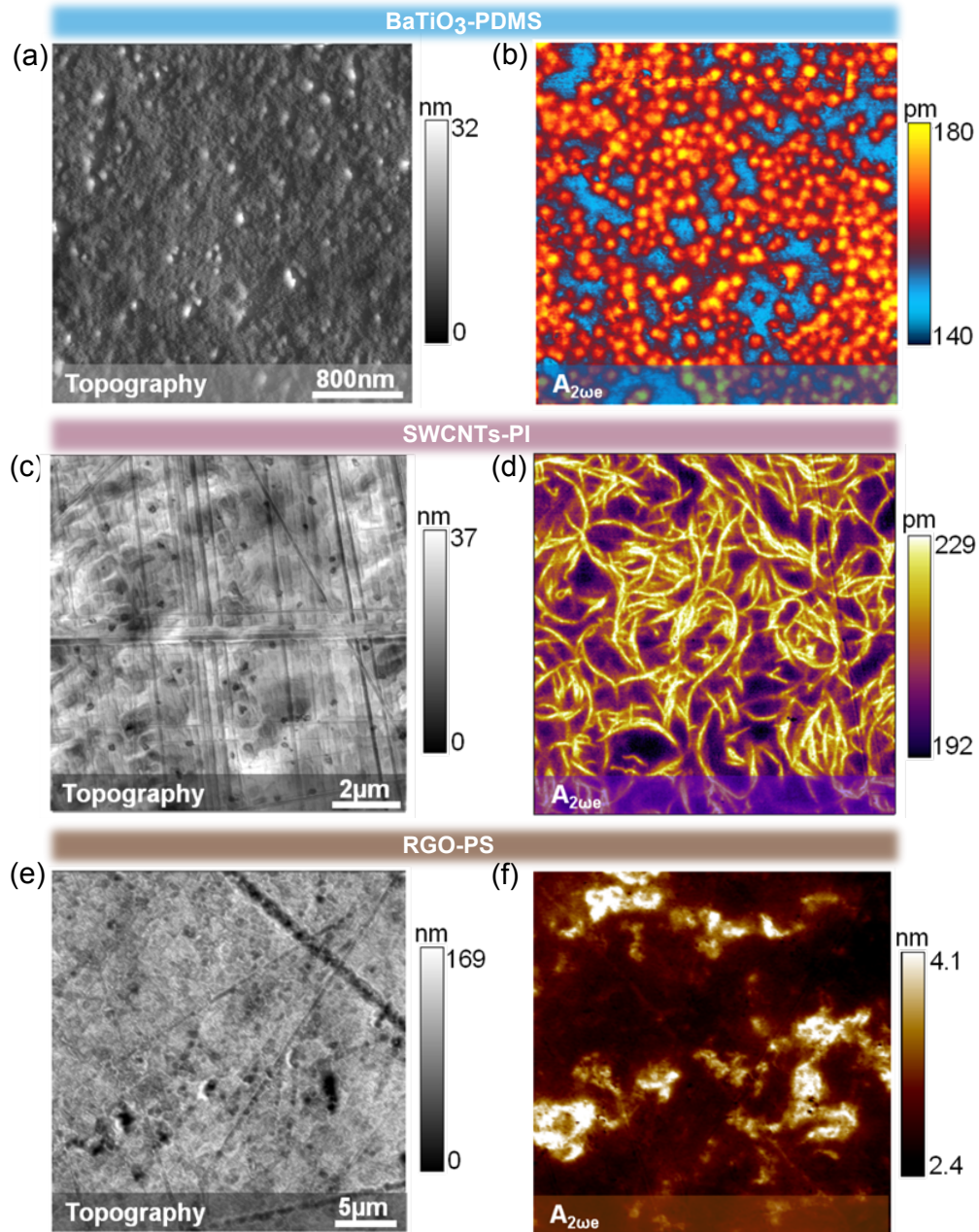
Figure 2.3. Representative subsurface images of polymer composites using resonance-enhanced 2nd-harmonic KPFM. (1st-column) Surface topography and (2nd-column) subsurface maps corresponding to (a-b) BaTiO$_3$-PDMS (0D composite), (c-d) SWCNTs-PI (1D composite), (e-f) RGO-PS (2D composite). Topography and $A_{2\omega_e}$ are obtained during the 1st and 2nd scans, respectively. Parameters: $A_0 = 14.6, 15.0, 29.7$ nm, $A_{sp} = 9.1, 10.0, 17.8$ nm, $\omega_0 = 66.8, 53.4, 66.8$ kHz, $V_{ac} = 8.0, 1.7, 3.0$ V, $\Delta Z = 8, 3, 10$ nm, $2\omega_e = \omega_1$ in all cases.
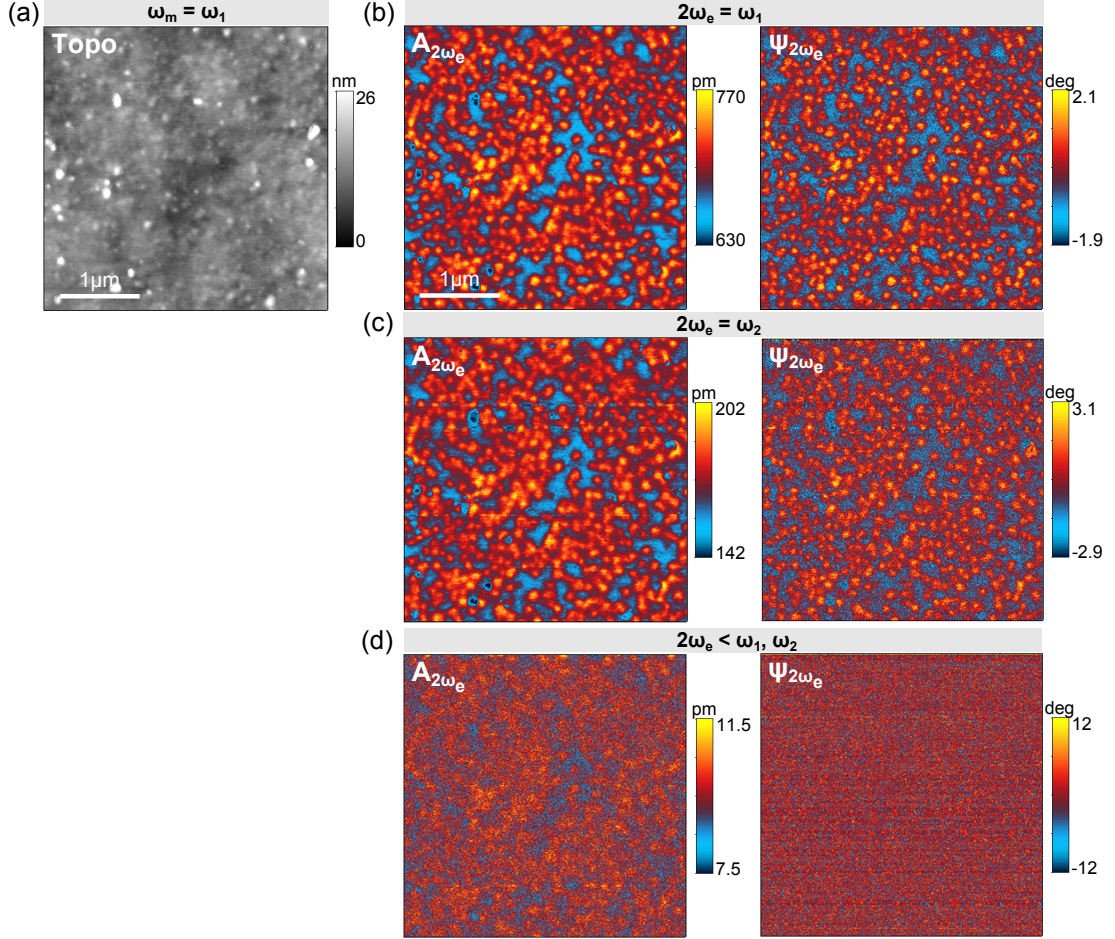
Figure 2.4. Comparison of resonance-enhanced and off-resonance double-pass KPFM for subsurface imaging on the BaTiO$_3$-PDMS composite. (a) Topography during the 1$^{\text{st}}$-pass ($\omega_m = 68.4$ kHz). Second and third column correspond to 2$^{\text{nd}}$-pass subsurface observables, $A_{2\omega_e}$ and $\Psi_{2\omega_e}$, for three cases: (b) $2\omega_e = 68.2$kHz $\approx \omega_1$ (resonance) and (c) $2\omega_e = 401.4$kHz $\approx \omega_2$ (resonance), and (d) $2\omega_e = 30$kHz $< \omega_1, \omega_2$ (off-resonance). Parameters: $A_0 = 11$ nm, $A_{sp} = 60\%$, $\Delta Z = 5$ nm, $V_{ac} = 4.8$ V.
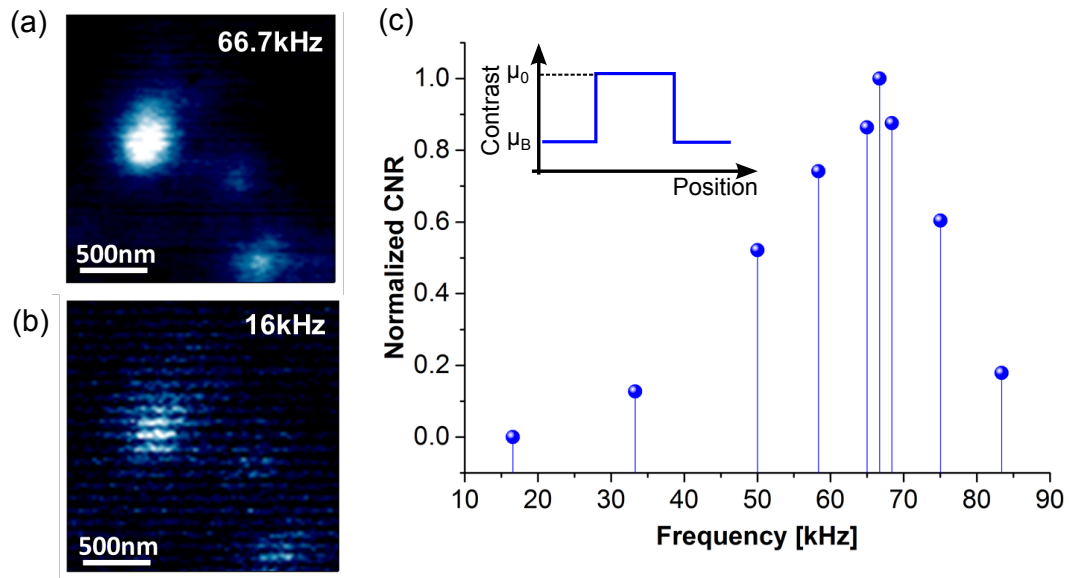
Figure 2.5. Contrast-to-noise ratio calculated for resonance and off-resonance frequencies. Representative subsurface maps of a BaTiO₃-PDMS composite region (a) at resonance and (b) off-resonance, where data was collected. (c) Normalized contrast to noise ratio as a function of the frequency of the 2nd-harmonic of the electrostatic force.
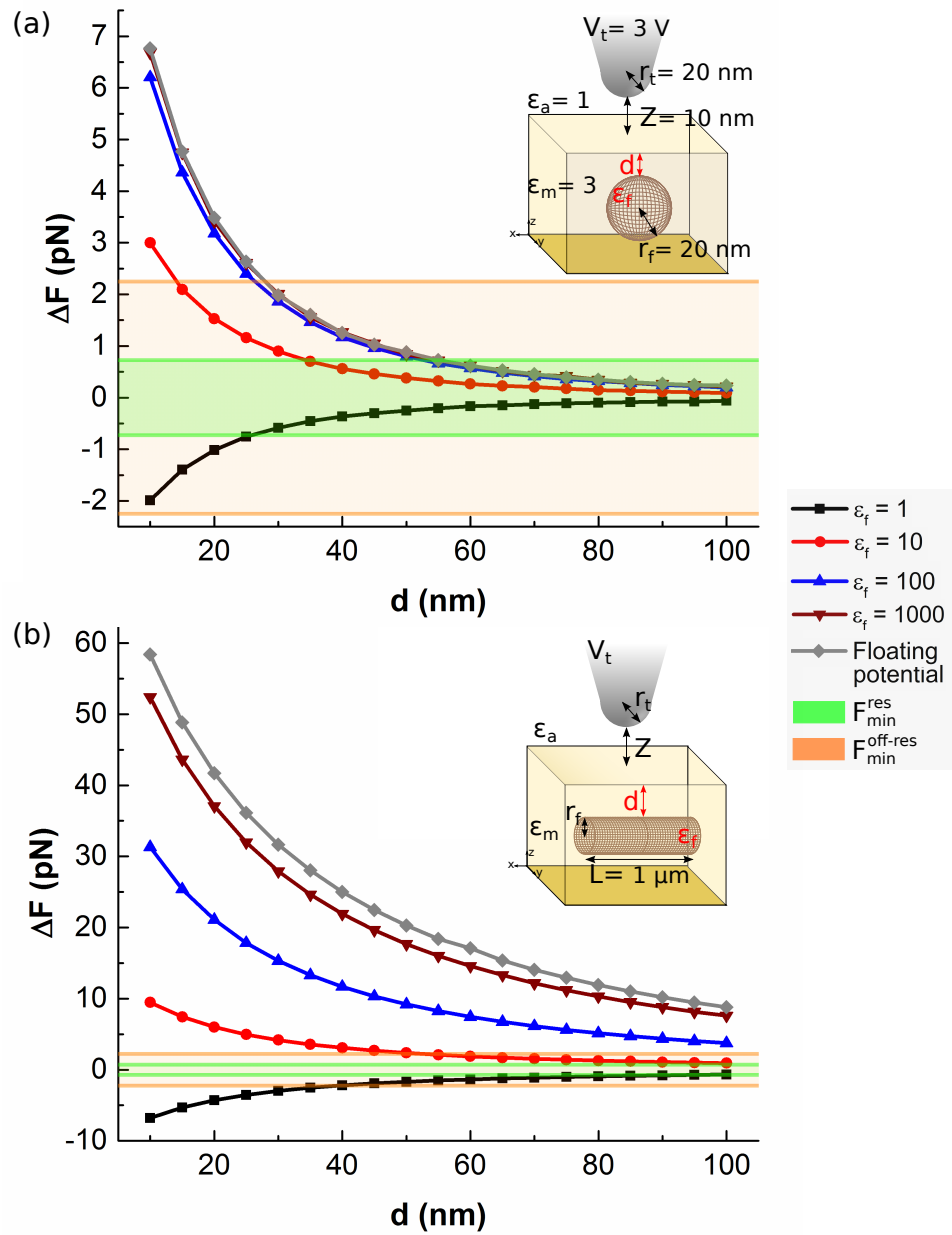
Figure 2.6. Force dependence on the dielectric properties of the filler (ϵ_f), embedded at a depth (d) in a low dielectric (ϵ_m) matrix . (a-b) ΔF as a function of depth (d) in the case of a 0D object (sphere) and a 1D object (cylinder) for different ϵ_f, respectively. When $\epsilon_f > 1000$, Δ_F approaches the case of floating potential boundary conditions on the filler. In both plots, the inset parameters labeled in black designate those variables held constant.
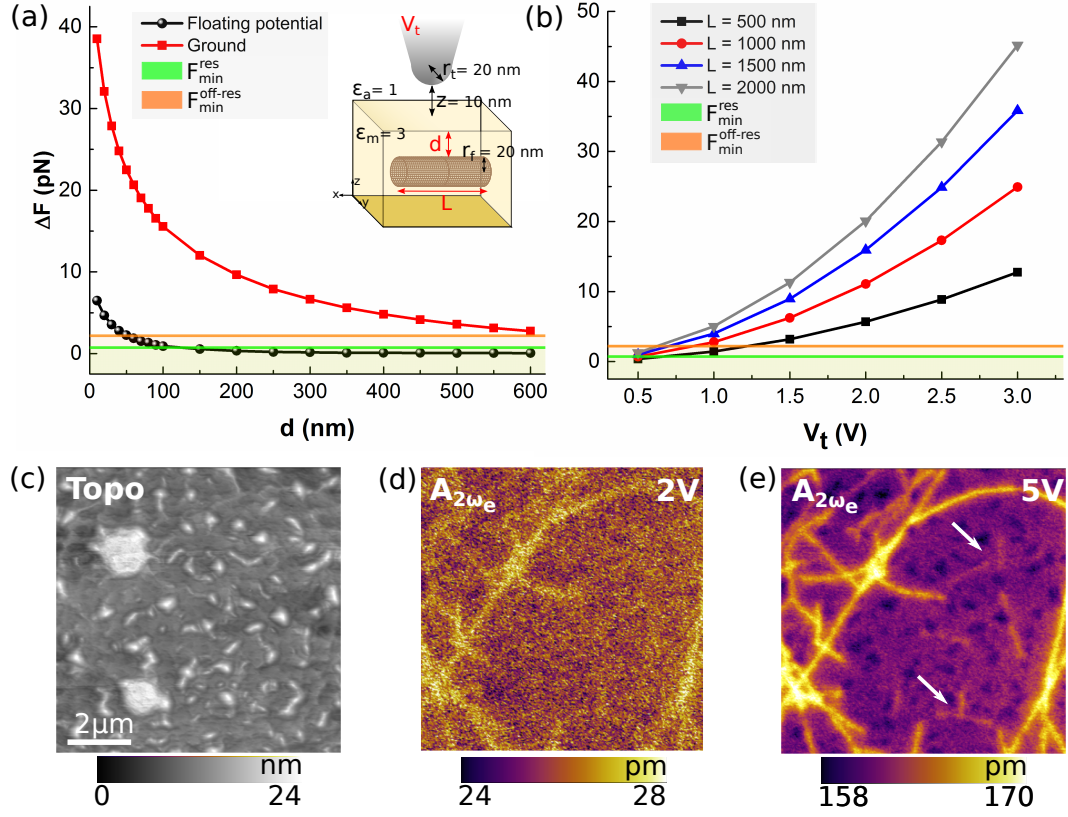
Figure 2.7. Depth sensitivity in the case of a 1D object (conductive cylinder) embedded in a low dielectric matrix ($\epsilon_m = 3$). (a) Dependence on boundary conditions of the conductive 1D object (floating potential or ground). The diagram corresponds to the geometry used in the computation model with fixed tip radius ($r_t = 20$ nm), length ($L = 1\mu$m), filler's radius ($r_f = 20$ nm) and tip-sample distance ($Z = 10$ nm). (b) Dependence on tip voltage V_t for different L, other parameters are kept constant and $d = 40$ nm. The thresholds correspond to F_{min} at resonance (green line) and off-resonance (orange line). (c) Experimental data obtained in a sample composed of 2D CNTs grown on silicon buried in a 40 nm coating of poly(styrene-butadiene-styrene) (SBS). The arrow indicates shorter CNTs not visible at lower voltage in (d).
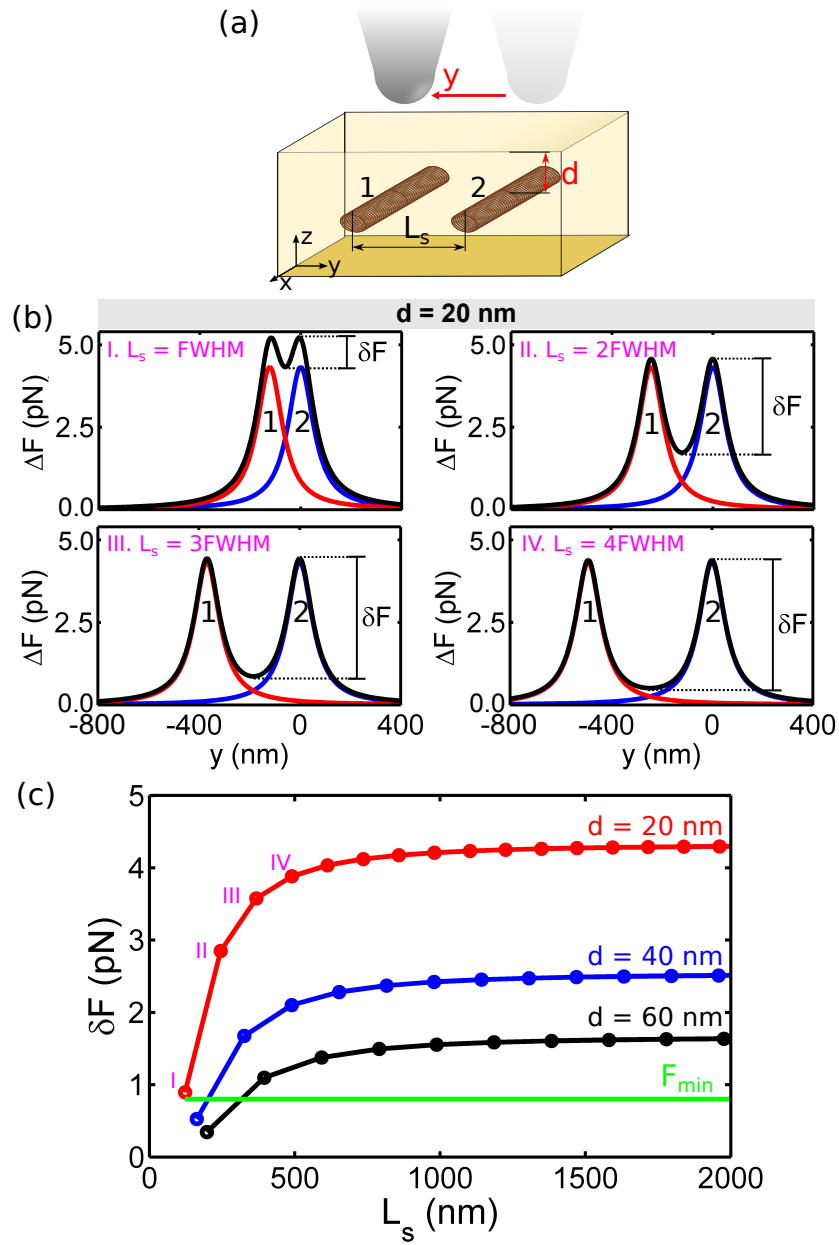
Figure 2.8. Lateral resolution in the case of a 1D conductive object embedded in a matrix as indicated by the diagram in (a). (b) Superposition of a profile obtained when tip scans above the embedded object ($d = 20$ nm) in the y-direction. (c) δF as a function of the separation distance (L_s) of two fillers at different depths. $F_{\min}$ is a typical noise level threshold for resonance-enhanced mode.
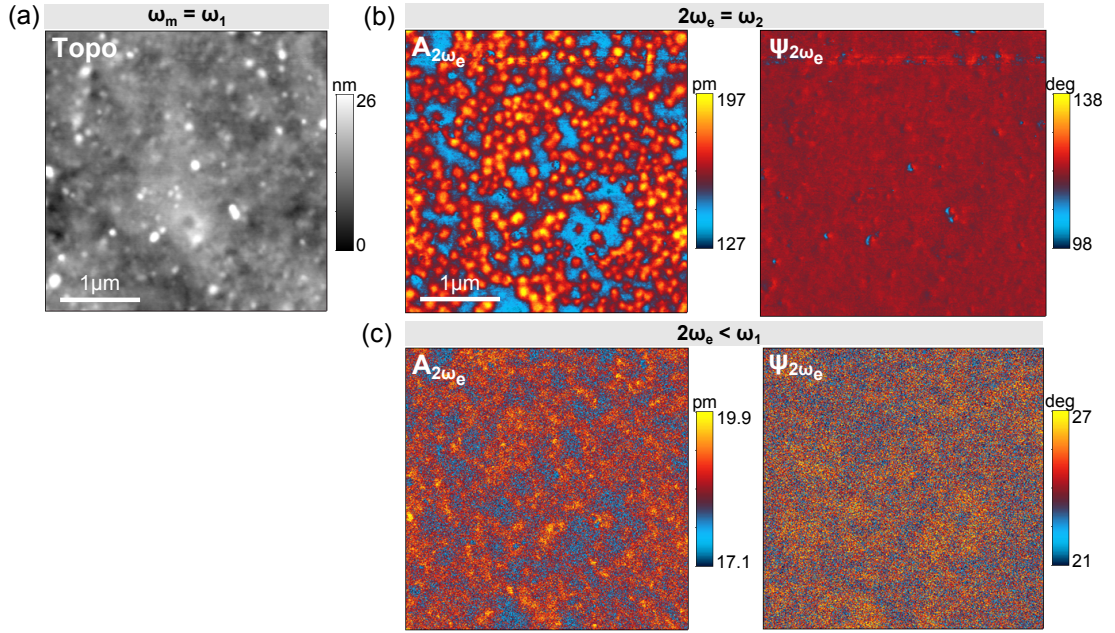
Figure 2.9. Comparison of resonance-enhanced and off-resonance single-pass KFPM for subsurface imaging on a $BaTiO_3$-PDMS composite. (a) Topography acquired simultaneously with subsurface maps, $A_{2\omega_e}$ and $\Psi_{2\omega_e}$, for the resonance case (b) $2\omega_e = \omega_2$ and the off-resonance case (d)$2\omega_e < \omega_1$. Parameters: $\omega_m = 68.4$ kHz, $A_0 = 11.8$ nm, $A_{sp} = 72\%$, $V_{ac} = 5$ V.

Table 2.1. Polymer nanocomposites used as samples for subsurface imaging using resonance-enhanced KPFM.

	Nanocomposite	Properties
0D	PDMS (Polydimethylsiloxane)	Polymer, insulator, $\epsilon_r = 2.3\text{-}2.8$
	BaTiO$_3$ (Barium titanate)	Ceramic, ferroelectric, $\epsilon_r = 1500$
1D	PI (Polyimide)	Polymer, insulator, $\epsilon_r = 4$
	SWCNTs (Single-walled carbon nanotubes)	Semiconductor or metallic
2D	PS (Polystyrene)	Polymer, insulator, $\epsilon_r = 2.4\text{-}2.7$
	rGO (Reduced graphene oxide)	Conductor

Table 2.2. Resonance-enhanced detection in double and single-pass 2nd-harmonic KPFM (ω_1, ω_2: frequencies of the 1st and 2nd flexural eigenmodes).

Mode		Excitation		Detection		Observables
		Mech.	Elec.	Mech.	Elec.	
Double pass	1st scan	$\omega_m = \omega_1$	-	ω_m	-	Topo, ϕ
	2nd scan	-	$\omega_e = \omega_1/2$	-	ω_e	CPD
					$2\omega_e$	$A_{1,2\omega_e}$, $\phi_{1,2\omega_e}$
Single pass	Simultaneous	$\omega_m = \omega_1$	$\omega_e = \omega_2/2$	ω_m	ω_e	Topo, ϕ, CPD
					$2\omega_e$	$A_{1,2\omega_e}$, $\phi_{1,2\omega_e}$

3. COMPARATIVE SUBSURFACE AFM IMAGING BY DETECTION OF ELECTROSTATIC FORCE INTERACTIONS AND LOCAL MECHANICAL PROPERTIES USING 2nd-HARMONIC KPFM AND CR-AFM

In this chapter, we compare the capabilities for subsurface imaging of 2nd-harmonic KPFM, and contact resonance AFM (CR-AFM). Both are robust techniques, in which the dynamic motion of the microcantilever can be quantitatively related to a physical variable. As described in Chapter 2, KPFM is based on the detection of electrostatic force interactions in the presence of an electric field. While CR-AFM detects variations on local mechanical properties upon the application of stress fields. These techniques have been reported separately for subsurface imaging, but little or no information is available to allow a direct comparison of the advantages, limitations and disadvantages offered by each technique. For this reason, a parallel study using both techniques is undertaken by mapping an identical region of a composite thin film containing single-walled carbon nanotubes (SWCNTs) buried in a polyimide (PI) matrix, with the same probe tip.

A prerequisite for a quantitative interpretation of the images obtained from either of these two approaches is the emphasis on numerical simulations. Except for the simplest configurations, analytical solutions to the interaction of a tip with subsurface features are not available. Not surprisingly, prior literature reports on a variety of studies using finite element methods [89, 98, 109, 141, 143]. In this study we use finite element simulations in COMSOL Multiphysics to compute solutions to two relevant problems: i) the electrostatic force that develops between a tip and a polymer matrix with an embedded CNT bundle and ii) the modulation of the contact stiffness when a tip indents the same matrix with the CNT bundle in it. This analysis allows a quantitative comparison between theoretical expectations and experiments. For instance, the experimental subsurface images clearly show a reduced lateral resolution

in KPFM, a trend also predicted by simulations, but a comparable depth sensitivity. Additionally, the simulations are used to infer the depth of a single CNT bundle from both experimental KPFM and CR-AFM images and the depth estimates are in good agreement with each other. By making a head-to-head comparison, we can convincingly assess the inherent advantages and disadvantages offered by each of these two techniques.

The layout of this chapter is as follows. First, it is presented an explanation of CR-AFM, with the theory and experimental setup of CR-AFM[1]. Then, the finite element computations for KPFM and CR-AFM are discussed. Lastly, experimental subsurface maps are presented from a polymer composite film. A major result is that we can infer the depth of subsurface CNTs, by matching the experimental data and computational results between the two techniques.

3.1   Contact-Resonance AFM

CR-AFM is a dynamic AFM technique use to measure the elastic and viscoelastic properties of a sample [100, 158–160]. In this technique, a resonant vibrational mode of the microcantilever is excited while the microcantilever tip is in contact with the surface of the sample. The resonant frequency of the surface-coupled microcantilever, namely contact-resonance frequency (ω_c), is sensitive to variations in the local contact stiffness. Particularly, minute elastic variations, induced by subsurface features, can be detected as the tip scans over the sample at a constant average force. To enhance the sensitivity of stiffness detection, higher eigenmodes of the microcantilever are often employed [96].

The local contact stiffness can be inferred from the contact resonance frequency, acquired as a function of lateral position. For this purpose, the Euler Bernoulli partial differential equation can be applied, assuming the microcantilever as a rectangular slender beam with uniform cross section.

---

[1]A detailed description of KPFM is given in Chapter 2

3.1.1 Beam Theory

The microcantilever in contact with the sample in the case of CR-AFM can be described by the model shown in figure 3.1(a). This model considers the microcantilever tilt, the tip position offset and the normal and lateral forces. The total length of the microcantilever is L and it is titled at an angle α. The tip has a length h and it is located at a position L_1 from the microcantilever base. The tip-sample contact is represented by a normal contact stiffness k^* and a lateral stiffness k_L^*, related to the normal and lateral forces, respectively [161].

To find the characteristic equation, we first start with the homogeneous equation of motion of the undamped microcantilever beam, given by

$$EI\frac{\partial^4 w(x,t)}{\partial x^4} + \rho A\frac{\partial^2 w(x,t)}{\partial t^2} = 0, \tag{3.1}$$

where EI, ρ, A and $w(x,t)$ are the flexural rigidity, mass density, cross-sectional area and deflection of the microcantilever, respectively. A general solution to the above equation can be expressed as,

$$w(x,t) = w(x) \cdot w(t) = e^{i\omega t} = (A_1 e^{\lambda x} + A_2 e^{-\lambda x} + A_3 e^{i\lambda x} + A_4 e^{-i\lambda x})e^{i\omega t}. \tag{3.2}$$

Substituting the solution into Equation (3.1), we get the dispersion relation given by

$$EI\lambda^4 - \rho A\omega^2 = 0. \tag{3.3}$$

which can be written as

$$\omega = \frac{(\lambda L)^2}{L^2}\sqrt{\frac{EI}{\rho A}} \tag{3.4}$$

The above equation can be used to calculate the resonance frequencies of the microcantilever. The resonance frequency of the nth mode normalized by the free resonance frequency is

$$\frac{\omega_n}{\omega_n^0} = \left(\frac{\lambda_n L}{\lambda_n^0 L}\right)^2. \tag{3.5}$$

Here, superscript 0 denotes the free resonance and the subscript n denotes the eigenmode number.

To relate the contact stiffness to the resonance frequencies, we need to build the characteristic function. This is obtained from the general solution and the boundary conditions given by the model in figure 3.1(a). For convenience, for the two microcantilever sections of length L_1 and $L_2 = L - L_1$, we can define

$$w(x,t) = \begin{cases} w_1(x_1, t) & \text{for } 0 < x_1 < L_1, \\ w_2(x_2, t) & \text{for } 0 < x_2 < L_2, \end{cases} \tag{3.6}$$

At the tip position ($x_1 = L_1$ and $x_2 = L_2$), the sample and microcantilever are coupled.

The boundary conditions of the model are

$$w_1(x_1 = 0, t) = 0, \tag{3.7}$$

$$\frac{\partial w_1}{\partial x}\Big|_{x_1=0} = 0, \tag{3.8}$$

$$w_1(x_1 = L_1, t) = w_2(x_2 = L_2, t), \tag{3.9}$$

$$\frac{\partial w_1}{\partial x_1}\Big|_{x_1=L_1} = -\frac{\partial w_2}{\partial x_2}\Big|_{x_2=L_2}, \tag{3.10}$$

$$EI\left(\frac{\partial^2 w_1}{\partial x_1^2}\Big|_{x_1=L_1} - \frac{\partial^2 w_2^2}{\partial x_2^2}\Big|_{x_2=L_2}\right) = -F_x h, \tag{3.11}$$

$$EI\left(\frac{\partial^3 w_1}{\partial x_1^3}\Big|_{x_1=L_1} + \frac{\partial^3 w_2^2}{\partial x_2^3}\Big|_{x_2=L_2}\right) = F_w, \tag{3.12}$$

$$EI\frac{\partial^2 w_2}{\partial x_2^2}\Big|_{x_2=0} = 0 \tag{3.13}$$

$$EI\frac{\partial^3 w_2}{\partial x_2^3}\Big|_{x_2=0} = 0 \tag{3.14}$$

where

$$F_x = h\frac{\partial w_1}{\partial x_1}\Big|_{x_1=L_1}\left(k^*\sin^2\alpha + k_L^*\cos^2\alpha\right) + w_1|_{x_1=L_1}\sin\alpha\cos\alpha\left(k_L^* - k^*\right), \tag{3.15}$$

$$F_w = h\frac{\partial w_1}{\partial x_1}\Big|_{x_1=L_1}\sin\alpha\cos\alpha\left(k_L^* - k^*\right) + w_1|_{x_1=L_1}\left(k^*\sin^2\alpha + k_L^*\cos^2\alpha\right). \tag{3.16}$$

The general solution given in Equation (3.2) can be re-written as

$$w(x,t) = A_1(\cos\lambda x\cosh\lambda x) + A_2(\cos\lambda x - \cosh\lambda x)$$
$$+ A_3(\sin\lambda x + \sinh\lambda x) + A_4(\sin\lambda x - \sinh\lambda x). \tag{3.17}$$

Using the piecewise definition for $w(x,t)$ (Equation (3.6)), the mode shape function given by the above equation, can be separated into

$$W_1(x_1) = A_1(\cos\lambda x\cosh\lambda x) + A_2(\cos\lambda x - \cosh\lambda x)$$
$$+ A_3(\sin\lambda x + \sinh\lambda x) + A_4(\sin\lambda x - \sinh\lambda x), \tag{3.18}$$
$$W_2(x_2) = B_1(\cos\lambda x\cosh\lambda x) + B_2(\cos\lambda x - \cosh\lambda x) \tag{3.19}$$
$$+ B_3(\sin\lambda x + \sinh\lambda x) + B_4(\sin\lambda x - \sinh\lambda x), \tag{3.20}$$

Applying the boundary conditions given in Equations (3.7), (3.8), (3.13) and (3.14), the coefficients $A_1 = A_3 = B_2 = B_4 = 0$. The other boundary conditions are then used to determine the remaining unknown constants in Equations (3.19), and (3.20). After a long process (details of the solution are given elsewhere [161, 162]), it is obtained the following equation [158]

$$\frac{C}{3}\frac{k_c}{k^*} + B + 3A\frac{k^*}{k_c} = 1, \tag{3.21}$$

where

$$A = \gamma^2\left(\frac{h}{L_1}\right)^2(1 - \cos\lambda_n L_1\cosh\lambda_n L_1)(1 - \cos\lambda_n L_2\cosh\lambda_n L_2), \tag{3.22}$$
$$\gamma = \frac{k_L^*}{k^*}, \tag{3.23}$$
$$B = B_1 + B_2 + B_3, \tag{3.24}$$
$$C = 2(\lambda_n L_1)^4(1 + \cos\lambda_n L\cosh\lambda_n L), \tag{3.25}$$

and

$$B_1 = \left(\frac{h}{L_1}\right)^2(\lambda_n L_1)^3\left(\sin^2 a + \gamma\cos^2 a\right)^2 \tag{3.26}$$
$$\times[(1 + \cos\lambda_n L_2\cosh\lambda_n L_2)(\sin\lambda_n L_1\cosh\lambda_n L_1 + \cos\lambda_n L_1\sinh\lambda_n L_1)$$
$$- (1 - \cos\lambda_n L_1\cosh\lambda_n L_1)(\sin\lambda_n L_2\cosh\lambda_n L_2 + \cos\lambda_n L_2\sinh\lambda_n L_2)],$$
$$B_2 = 2\left(\frac{h}{L_1}\right)^2(\gamma - 1)\cos a\sin a \tag{3.27}$$
$$\times[(1 + \cos\lambda_n L_2\cosh\lambda_n L_2)\sin\lambda_n L_1\sinh\lambda_n L_1$$
$$+ (1 - \cos\lambda_n L_1\cosh\lambda_n L_2)\sin\lambda_n L_2\sinh\lambda_n L_2],$$

$$B_3 = \lambda_n L_1 \left(cos^2 a + \gamma sin^2 a \right) \tag{3.28}$$
$$\times \left[(1 + cos\lambda_n L_2 cosh\lambda_n L_2)(sin\lambda_n L_1 cosh\lambda_n L_1 - cos\lambda_n L_1 sinh\lambda_n L_1) \right.$$
$$\left. - (1 - cos\lambda_n L_1 cosh\lambda_n L_1) \times (sin\lambda_n L_2 cosh\lambda_n L_2 - cos\lambda_n L_2 sinh\lambda_n L_2) \right].$$

Combining Equations (3.5) and (3.21), we can thus relate the measured resonance frequency to contact stiffness (k^*).

3.1.2 Experimental Setup: DART Mode

To implement CR-AFM, we use a piezoceramic transducer (Steminc, Miami, FL, USA) placed in close contact to the bottom of the sample. The transducer has a resonance frequency of 4.25 MHz and a nominal piezoelectric constant of 450 pm/V. The excitation waveform was generated by the internal direct digital synthesizer of the AFM controller and the microcantilever oscillation signal was analyzed using the ARC2 controller of the Cypher AFM. Subsurface imaging was realized by either driving at a single frequency or employing the dual AC resonance tracking (DART) mode [163]. The schematic of the experimental setup is shown in figure 3.1(b).

The microcantilever is first brought into contact with the sample at a preset normal force. By using a frequency sweep, the contact resonance frequencies are determined. Then, dual excitations are applied to modulate the tip-sample contact at two frequencies (ω_1 and ω_2). These two frequencies are centered near the contact resonance with one below resonance and another above. The corresponding microcantilever amplitudes (A_1 and A_2) were analyzed by lock-ins A and B respectively. During scanning, the resonance frequencies are tracked by changing the excitation frequencies via a feedback loop to maintain the amplitude difference constant [163].

3.2 Finite Element Analysis (FEA)

Two separate computational models are built into COMSOL Multiphysics, within the AC/DC and Solid Mechanics modules, respectively. These models are used to

calculate the electrostatic force and the contact stiffness, as in KPFM and CR-AFM, respectively.

3.2.1 Electrostatic Force Calculation

The Electrostatics interface, available in the AC/DC module, is used to solve the electrostatics problem with boundary conditions, similar as in Chapter 2. i) A constant electric potential applied to the probe, ii) a constant electric potential (0 V , ground) at the bottom surface of the sample (polymer matrix with dielectric constant), iii) a floating potential on the cylinder surface (CNT bundle), and iv) zero charge in the air region surrounding the probe and the sample. Charge conservation was enforced everywhere. We use the floating potential condition assuming the CNT bundle is conductive or has a conductivity many orders of magnitude larger than the surrounding medium and is not connected directly to ground. The tip of the probe is modeled as a hemisphere (apex) with radius R_{tip} attached to a cone with a half angle θ and length L_{tip}. The microcantilever is modeled as a disk of radius R_{cant} and thickness T_{cant} approximately equal to the given specifications of the FORTA probe (AppNano). The surrounding air is defined as an infinite element domain. The values of relevant parameters are given in Table I.

To compute the electrostatic force on the probe an integration of the Maxwells stress tensor is performed on the external surface, as it is detailed in Chapter 2.

3.2.2 Contact Stiffness Calculation

A similar procedure is followed to simulate the stress field generated when the tip exerts a force on the polymer composite. The contact stiffness that results when an AFM tip scans over a nanocomposite is analyzed using the Solid Mechanics module. The tip is modeled as a silicon hemisphere. The top of the sample and the bottom of the tip are defined as a contact pair while the CNT-polymer interface is treated as perfectly bounded. Automatic global fine meshing is applied on all FEA elements,

with further adaptive refinement around the tip-sample contact area and the CNT-polymer interface.

The same sample geometry is employed using a silicon hemisphere of radius R_{tip} as the tip of the AFM probe (figure 3.2(c)). The top of the sample and the bottom of the tip are defined as a contact pair while the CNT-polymer interface is treated as perfectly bounded. Automatic global fine meshing is applied on all FEA elements, with further adaptive refinement around the tip-sample contact area and the CNT-polymer interface. At each point of contact, the FEA calculates the sample deformation dF_n for an applied normal load F_n. The contact stiffness is then calculated by

$$k^*(F_n) \approx \frac{1}{2}\left[\frac{(F_n + \Delta F) - F_n}{d_{F_n + \Delta F} - d_{F_n}} + \frac{F_n - (F_n - \Delta F)}{d_{F_n} - d_{F_n + \Delta F}}\right]. \qquad (3.29)$$

Here, ΔF is an incremental force step (5 nN in our calculations). Before computations, we validated the 3D FEA model by comparing with the Hertz theory in the case of an AFM tip contacting an elastic half-space. The relative deviations of the contact stiffness were found to be less than 5% for a load up to 100 nN.

All relevant parameters employed when simulating these two situations are listed in Table I. A distinguishing characteristic of the results plotted in figures3.2(b) and 3.2(c) is the non-local nature of the electrostatic field in KPFM when compared to the highly localized stress field that develops in CR-AFM.

3.3 Results and Discussion

3.3.1 Subsurface Maps

To investigate subsurface imaging and to compare the predictions of the simulations to data, a parallel experimental AFM-based study of a PI-SWCNTs composite film was performed. The measurements were conducted using a Cypher AFM (Asylum Research, Santa Barbara, CA, USA) operating under ambient conditions. A rectangular, highly doped Si microcantilever model FORTA (Applied Nanostructures,

Mountain View, CA, USA) with spring constant of 1.23 N/m by thermal calibration and free resonance frequency of 53.48 kHz was used throughout.

We use resonance-enhanced KPFM in double-pass mode. The tip is withdrawn by an amount ΔZ, and an electrical excitation ($V = V_{ac}\sin\omega_e t + V_{dc}$) is applied to the tip with ω_e close to $\omega_0/2$. The tip is scanned across the sample surface taking into account the geometry of the sample that was just previously measured. The amplitude of the microcantilever response at $2\omega_e$ are acquired which correspond to the 2nd harmonic of the electrostatic force (Equation (2.8)) using resonance-enhanced mode ($2\omega_e \approx \omega_0$). Some of the parameters used in this study are: $V_{ac} = 1.7$ V, $\Delta Z = 10$ nm and $2\omega_e = 53.4$ kHz. The typical image size was 10 μm $\times$ 10 μm and contained 512×512 points. The scan rate was 1.0 Hz and it required ≈ 8.5 minutes to acquire a single image.

After mapping the KPFM signal, the same region of the sample was studied using CR-AFM using the same probe. In the experiment, the applied normal force was approximately 65.0 nN. The 3rd-eigenmode with resonance frequency of ~ 1.035 MHz was used because it demonstrated the best frequency sensitivity to the contact stiffness variations among the first three eigenmodes. The typical image size was 10 μm $\times$ 10 μm and contained 512×512 points. The scan rate was 1.0 Hz and it required ~ 8.5 minutes to acquire a single image.

Typical subsurface images are summarized in figure 3.4. Topography and the microcantilevers oscillation amplitude at the 2nd harmonic of the electrostatic force ($A_{2\omega_e}$) from KPFM are shown in figure 3.4(a,b). Figures 3.4(c, d) contain the maps of topography and the 3rd eigenmode CR frequency shift (CR-Freq) of the microcantilever when loaded against the polymer composite. The surface topography using both techniques reveal identical features and show no evidence of CNTs on the surface. A careful comparison of $A_{2\omega_e}$(figure 3.4(b)) to CR-Freq (figure 3.4(d)) shows excellent agreement in the location and shape of the subsurface bundles of CNTs. In addition, the CR-Freq map clearly reveals a sensitivity to surface defects (parallel scratch lines in figure 3.4(d)) when compared to the $A_{2\omega_e}$map in figure 3.4(b).

3.3.2   FEA: Lateral Resolution and Depth Sensitivity

A salient result from the finite element simulations comes from a comparison between the change in electrostatic force (ΔF for KPFM) and the change in contact stiffness (Δk^* for CR-AFM) as a function of the depth of the CNT bundle beneath the surface with respect to the neat polymer. In both instances, the numerical difference is calculated when the tip is positioned directly over the buried CNT bundle and when the tip is positioned over the uniform polymer matrix with no presence of CNT. As shown in figure 3.3 both ΔF and Δk^* decrease as the depth of the CNT bundle beneath the interface increases. Both ΔF and Δk^* intersect the noise-floor as the CNT is buried deeper, giving rise to the saturation in figure 3.3(a) as the depth increases and have a small but systematic dependence on tip radius. This result implies that both techniques are limited to imaging CNT bundles of radius 20 nm and length 300 nm that are within approximately 50 nm below the surface, for CR-AFM and KPFM respectively. The depth sensitivity will vary depending on the tip-sample geometry, its electrical/mechanical properties and the noise from the AFM system. For instance, previous work has shown a higher depth sensitivity in which the CNTs are assumed to be grounded [109].

It is also worth noting that there are other approaches to KPFM which measure different quantities related to the electrostatic force [104, 164]. In this work we only measure the electrostatic force as this is the most common output from KPFM in amplitude modulation mode. Further simulations were performed in which the AFM tip was rastered in a direction perpendicular across the buried CNT bundle. In these simulations, both $F(x)$ and $k^*(x)$ were calculated as a function of the depth of the bundle, where x is the raster direction of the tip. An important feature comes by closely examining the profiles of the simulated KPFM and CR-AFM scans across the CNT bundle and calculating the full width at half maximum (FWHM) versus depth as shown in figure 3.3(b). The inset is a representative result of the scan across a CNT bundle at 5 nm deep. From these simulations, we conclude the width from

CR-AFM is essentially independent of the CNT depth, being equal to the diameter of the bundle assumed in the simulations (40 nm). In this regard, when imaging a subsurface feature, CR-AFM provides depth independent information about the width of the embedded object closer to its actual value. On the contrary, a larger FWHM is obtained in the case of KPFM, which increases with the depth of the bundle. This indicates a diminished lateral resolution, which could be utilized to infer the depth of the object.

3.3.3 Electric Field vs Stress Field

The computational results above can also be understood from the point of view of Greens function-like response in the simple cases of the electric field ($\mathbf{E}$) in a dielectric slab generated by a point charge Q located outside at a distance Z (in air) and the stress field (σ_z) generated by an applied point force at the surface of an elastic material. In the former case, the magnitude of $\mathbf{E}$ inside the dielectric (relative dielectric constant ϵ_r directly below Q is given by [165] $|\mathbf{E}| = \frac{1}{4\pi\epsilon_0} \frac{2Q}{(\epsilon_r+1)} \frac{Z}{(Z+d)^3}$. In the latter case the normal stress generated at a depth d directly below where a normal point force P is applied on the surface can be calculated from a Boussinesq analysis [166] to be $\sigma_z = -\frac{3P}{2\pi} \frac{1}{d^2}$. Using both analytical expressions, the decay of the fields as a function of depth d and Z demonstrated in the computations can be explained. Specifically, the decay of $|\mathbf{E}|$ with d can be slower than the decay of σ_z with d when Z is sufficiently large and the depth d of the object is sufficiently small. This qualitatively explains the computational results described above.

The force sensitivity defined as the minimum resolvable electrostatic force is indicated by the horizontal threshold line marked in figure 3.3a. It is mainly limited by the noise level dominated by the thermal noise of the microcantilever (η_{th}) due to Brownian motion and ii) the detector noise with the optical beam deflection sensor (η_{obd}) as the major contributor [146]. In Cypher AFM $\eta_{obd} = 25$ fm/H$^{1/2}$. The thermal noise is given by Equation (2.24). Within the frequency bandwidth range of

the lock-in amplifier (B), the minimum detectable amplitude due to thermal noise is then given by $A_{th} = \eta_{th}\sqrt{2B}$, which depends on the microcantilever geometry and the environment. With the parameters from the experiment, $f_0 = 53475$ Hz, $k = 1.23$ N/m, $Q = 99.05$, $B = 1000$ Hz, at an excitation frequency of 55000 Hz (assumed for detection), A_{th} is equal to 15.14 pm. Then the minimum detectable force due to thermal noise (F_{th}) is 1.09 pN. On the other hand, the minimum detectable amplitude and force due to η_{obd} is 1.12 pm and 0.081 pN, respectively. Therefore, the total minimum force is $F_{min} = \sqrt{F_{th}^2 + F_{obd}^2} = 1.09$ pN.

Contact resonance sensitivity is further analyzed from the frequency-stiffness relation [100]. The sensitivity can be defined as the frequency change with respect to the contact stiffness change, that is, $S_n = \frac{\partial(\omega_n/\omega_1^0)}{\partial(k^*/k_C)}$. The calculated sensitivity ratio defined in this way was compared with the measured frequency shift ratio among the first three eigenmodes. Within our experimental settings, the 3rd-eigenmode resonance demonstrated the best sensitivity to contact stiffness. The experimental frequency resolution is roughly estimated as 1 kHz. Using tip radius of 20 nm, normal force of 65 nN, microcantilever spring constant of 1.23 N/m and 1st free resonance frequency of 53.48 kHz, the corresponding stiffness resolution is determined to be approximately 0.84 nN/nm.

Based on simulations, the top surface of a buried CNT bundle of nanotubes with 20 nm radius and 300 nm length (not grounded) is within approximately 50 nm of the surface if it is to be imaged using KPFM or CR-AFM. Greater depths can be obtained in CR-AFM if the load is increased or in KPFM if the voltage on the tip is higher or the CNT bundle is longer or grounded [109]. CR-AFM senses a very localized change in elasticity and simulations show this technique has a lateral resolution independent of depth. In contrast, the resolution achieved by KPFM is about a factor of 2 less than in CR-AFM and does depend on depth.

3.3.4   Depth Estimation from Experiments and FEA

By examining a zoom-in on a single CNT bundle imaged using both techniques as shown in figure 3.5(a) and (b), it is clear that the apparent width of the bundle of CNTs is greater in KPFM than in CR-AFM, in agreement with the results presented in figure 3.3(b). Careful measurements of the FWHM give values of 37.7 ± 6.2 nm for CR-AFM and 67.0 ± 13.4 nm for KPFM. The ratio of these two numbers agrees with predictions based on the simulations plotted in figure 3.3(b).

To infer the depth of the CNT bundle, line scans across five separate locations were analyzed. From this data, the change in the KPFM signal and the frequency shift of the 3$^{\text{rd}}$ eigenmode could be determined as a function of position. In both cases, we compare the change in signal when the tip was directly above the CNT bundle to when the tip was located far from the CNT. The simulations in figure 3.3(a) were then used to convert these measured values into a depth below the surface ($R_{tip} = 20$ nm). If the simulations are accurate, both techniques should provide the same depth for this particular CNT bundle. A direct comparison is provided in figure 3.5(a) and shows that on average, for the KPFM data, the depth is 29.1 ± 2.8 nm while for the CR-AFM data, the average depth is 33.7 ± 2.6 nm. The agreement between the two depths is very satisfactory within the limits of the uncertainty.

In the process of inverting the observables to depth, there are systematic uncertainties to consider, which come from the model and experiments. For instance, assumptions in the FEA with respect to the boundary conditions and size of the CNT, and probe geometry, lead to the over- and under-prediction of the depth of the CNT, when inferred from k and $F_{2\omega_e}$ measurements, respectively, as reflected in the data (figure 3.5(a)). As a further validation of depth estimation, an additional region shown in figure 3.5(b), was analyzed following the same procedure. It is noted the same trend of over- and under-prediction of CNT depth using CR-AFM and KPFM, respectively. As such, the systematic difference in the prediction of depth is consistent and not an anomaly.

3.4   Summary

The results of this study allow a direct comparison between two techniques commonly used for subsurface imaging. CR-AFM relies on a nano-mechanical modulation of the surface elasticity due to buried objects. This technique is noteworthy because it requires no special restrictions on the sample like electronic conduction or magnetism. On the other hand, 2nd-harmonic KPFM, requires samples in which the matrix is insulating or weakly conducting. If this condition is not met, the electrostatic fields cannot penetrate to probe local changes in the dielectric properties due to buried subsurface objects. Another salient difference between the two techniques is that CR-AFM senses a very local change in sample stiffness due to a buried object while KPFM is limited by the non-local nature of the electrostatic field that develops between the tip and a buried object. As a result, the lateral spatial resolution of CR-AFM is about $\frac{1}{2}$ that achieved by KPFM. A brief summary of the advantages and disadvantages of each technique is presented in Table 3.2. Thus CR-AFM and KPFM both enable high sensitivity subsurface imaging, each based on the sensing of a distinct physical property. Additionally, in both techniques, quantitative three-dimensional reconstruction of subsurface features is possible through computer simulations that incorporate the important geometrical/electrical/mechanical features of the buried object and the surrounding matrix under study.
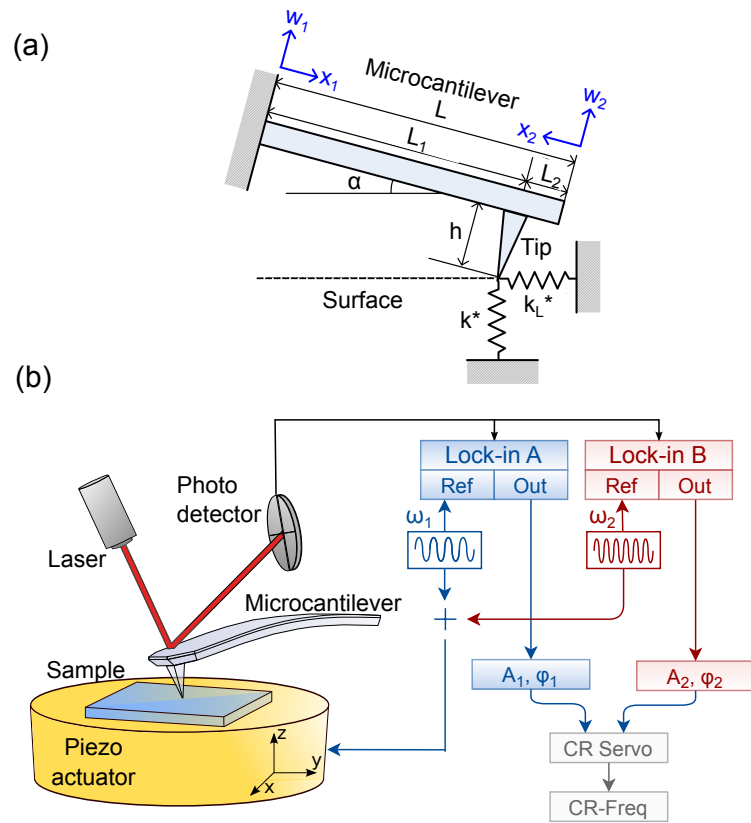
Figure 3.1. Representative diagrams for CR-AFM. (a) Schematic of the analytical model of a microcantilever in contact with the surface of the sample, used to find k^*. (b) Schematic of the experimental setup in DART mode. The CR-Freq map is monitored to map subsurface features.
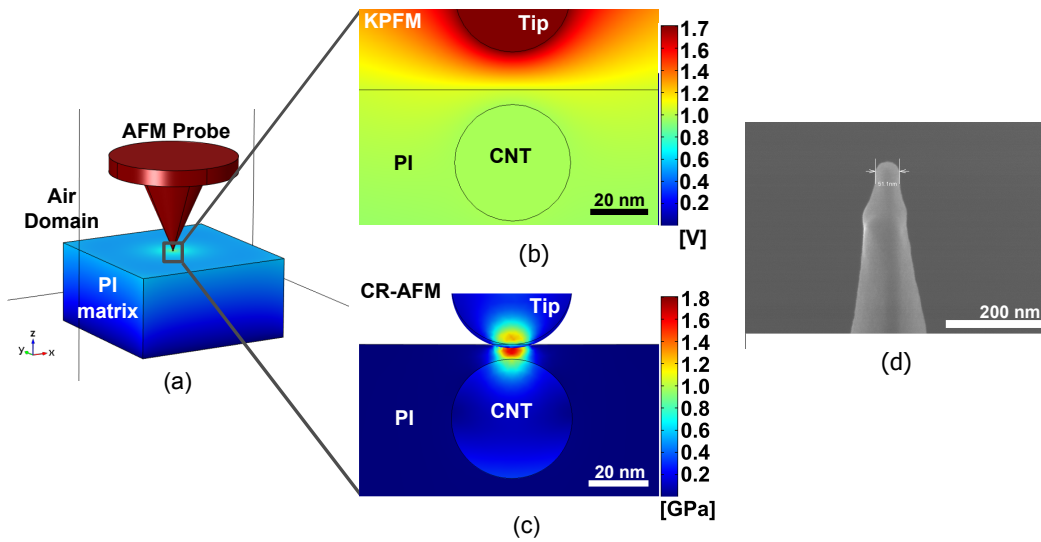
Figure 3.2. Finite element computations for an AFM tip near a PI-SWCNTs composite sample. In a), 3-dimensional visualization showing the geometry of the AFM probe positioned above the composite film resting on a ground plane which defines $V = 0$ V. In (b), a cross-section through the symmetry plane of the tip showing the calculated electrostatic potential field developed near the tip in KPFM. The bias voltage on the tip is 1.7 V and the tip-sample distance is 13 nm. In (c), a plot of the tip-sample elastic stress field induced by tip-sample contact in CR-AFM. The applied normal force is 65 nN. The location of the CNT below the interface is indicated by the circle in both b) and c). In (d), an SEM image of the tip used during experiments with a tip radius of 25.5 nm.
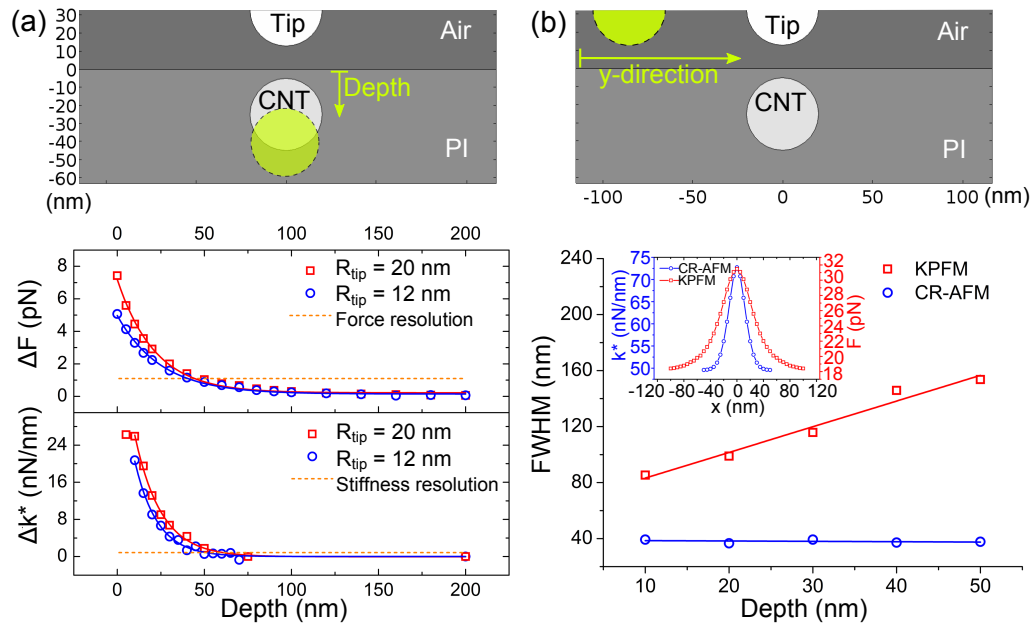
Figure 3.3.   Finite element results for an AFM tip near a polyimide/SWNT composite sample. In (a), the computed electrostatic force difference (ΔF) and stiffness difference (Δk^*) as a function of buried CNT bundle depth (radius = 20 nm, length = 300 nm). The simulations for two tip radii are included for comparison. In (b), the FWHM calculated from the profile across a CNT bundle as a function of CNT depth. A typical result, plotted in the inset, graphically illustrates the higher lateral resolution produced by the CR-AFM technique.
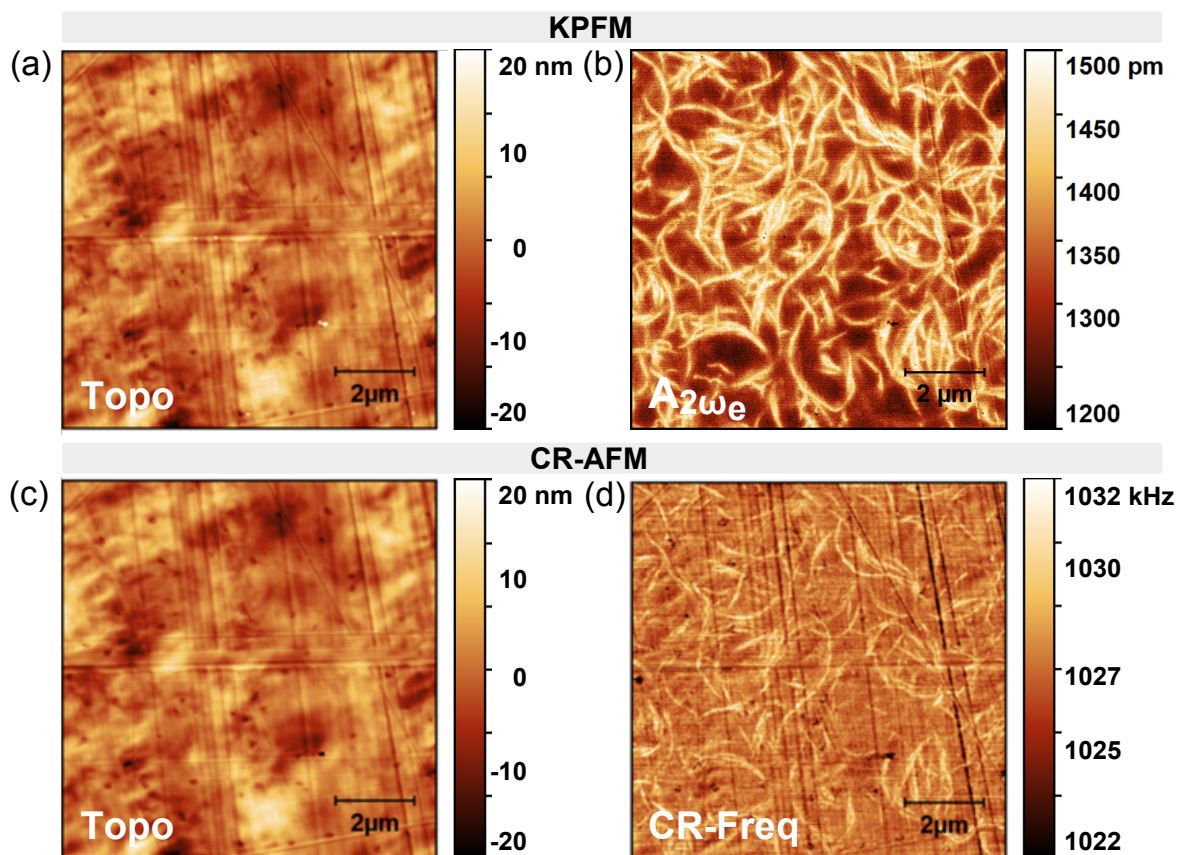
Figure 3.4. Subsurface maps of CNT bundles in a PI-SWCNTs film taken over the exact same region. In (a), the topography from the first-pass of KPFM in noncontact mode. In (b), the corresponding 2nd harmonic KPFM amplitude map. In (c), the topography from CR-AFM. In (d), the frequency map taken at the 3rd-eigenmode CR frequency.
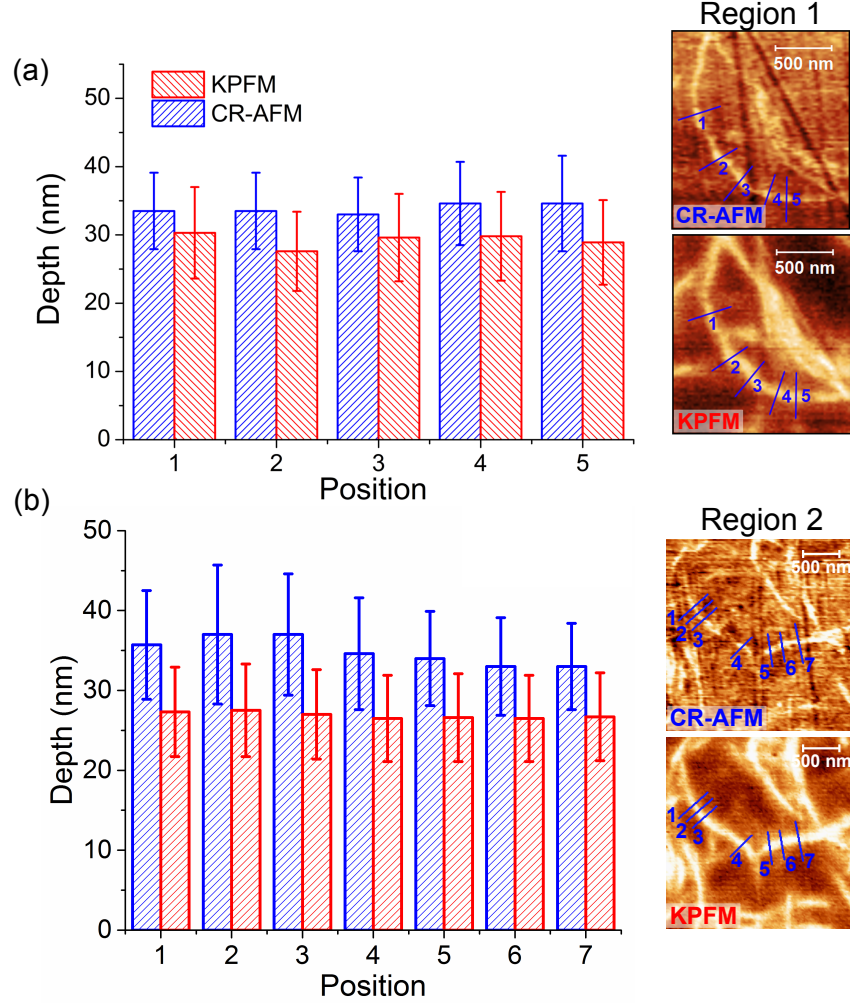
Figure 3.5. Comparison of CNT depth estimation for CR-AFM and KPFM using the results from the finite element analysis (figure 3.3(a)). In (a) and (b) estimation of CNT depth at positions numbered from 1 to 5 in region 1, and positions numbered from 1 to 7 in Region 2, respectively. In both cases, the subsurface images correspond to the 3rd-eigenmode CR-Freq from CR-AFM and $A_{2\omega_e}$ from KPFM.

Table 3.1. Relevant input parameters for FEA in COMSOL Multiphysics.

	Parameters	Symbol	Value
Common	CNT radius	R_{CNT}	20 nm
	CNT length	L_{CNT}	300 nm
	Tip radius	R_{tip}	20 nm
CR-AFM	PI dimension	$L \times W \times T$	$800nm \times 400nm \times 500nm$
	PI modulus	E_{PI}	3.6 GPa
	CNT modulus	E_{CNT}	400 GPa
	Tip modulus	E_{Tip}	165 GPa
	Poisson's ratio	ν	0.3
	Normal force	F_n	60 nN, 65 nN, 70 nN
KPFM	PI dimension	$L \times W \times T$	60 μm $\times$ 60 μm $\times$ 10 μm
	PI dielectric constant	ϵ_r	3.4
	Bias voltage	V	1.7 V
	Tip-sample distance	Z	13 nm
	Half cone angle	θ	25deg
	Tip length	L_{tip}	14 μm
	Microcantilever width	R_{cant}	13.5 μm
	Microcantilever thickness	T_{cant}	2.7 μm

Table 3.2. Comparison between CR-AFM and KPFM for subsurface imaging.

	CR-AFM	KPFM
Physical property for subsurface detection	Local stiffness (mechanical property)	Electrostatic force (dielectric property)
Sample limitation	Contrast between modulus of substrate vs. modulus of buried object	Contrast between dielectric of substrate vs. dielectric of buried object
Detectability limit	Determined by minimum difference in stiffness (typically 1 N/m)	Determined by minimum difference in electrostatic force (typically 1 pN)
Maximum depth[a]	Approx. 50 nm.	Approx. 50 nm.

[a] Applicable only for the particular sample analyzed in this study (parameters are given in Table I, and for ungrounded CNT. The maximum depth in KPFM changes significantly depending on electrical boundary condition applied to the buried CNT.

4. 3D RECONSTRUCTION OF 0D-NANOCOMPOSITES USING A SURROGATE MODEL BASED APPROACH IN AFM

The quantification of subsurface properties from a sample investigated by an AFM probe is not an easy task. A key challenge is to reconstruct the spatial distribution of the subsurface in three dimensions, with images that are typically acquired in two dimensions. This necessarily is an inverse problem where some type of model will be needed to relate a measured physical variable at each pixel to the properties of subsurface objects such as size, depth, orientation, physical properties etc., using AFM for subsurface reconstruction. Examples of subsurface reconstruction described in earlier chapters or prior work [109, 167] assume that all properties, include dimensions of the subsurface object are already known, and all that remains to be identified is the depth. Here we present an approach that can be used to reconstruct the unknown depth and size of the buried object, and can in principle be used to estimate other unknown properties of the buried object.

In this study, we use the electrostatic force measured in 2nd-harmonic KPFM as the basis for non-destructive reconstruction of subsurface features. This force constitutes the response variable of the microcantilever-system in the KPFM setup. Based on a surrogate model, we propose a method to solve the inverse problem of finding the spatial distribution of nanosized features embedded in a matrix, determined by their size and depth. The model is an approximation to define the relationship between the electrostatic force and some of the tip-sample properties relevant to the problem.

This chapter presents a description of the surrogate model based approach for non-destructive reconstruction purposes. The proposed method involves three main steps. First, it requires the creation of an interpolation function. This involves the development of a parametric study, defining the relevant variables to the problem and the computation of the response variable in terms of the input variables. The

latter achieved by a finite element model. Second, it requires the acquisition of a experimental subsurface data set, for which the surrogate model can be applicable. In this case, we use subsurface detection based on the electrostatic force interactions at varying Z distances. This is done by resonance-enhanced 2nd-harmonic KPFM in double-pass mode. Third, it requires the solution of the inverse problem of finding sample properties by means of the surrogate model and the experimental data set. This study focuses on 0D subsurface objects (spherical nanoparticles) buried in a matrix (polymer). The aim is to estimate their size and depth in a quantitative manner.

4.1 Surrogate Model

The physical phenomena of some systems can not be described by a mechanistic or analytical model. Such is the case of the electrostatic force interactions between the AFM probe and complex heterogeneous samples. As described in Chapter 2, the electrostatic force is proportional to the capacitance gradient with respect to tip-sample separation and the potential difference between the tip and the sample. Ideally, it would be affected only by variations in capacitance. However, it is also influenced by other parameters, such as the geometry of the probe and sample. For instance, non-local effects are generated by unknown contributions from the macroscopic parts of the probe (stray capacitances).

Analytical expressions for the electrostatic force have been derived for simplified geometries, considering flat (semi-) conductive substrates or thin dielectric films [135–140]. In the case of more complex substrates, other approaches use numerical methods to solve a boundary integral equation given by Green's function [168, 169], a self-consistent integral equation method [170] or finite element analysis [171]. Computational models have the advantage of calculating the interaction force using a geometry more approximated to real experimental scenarios. In Chapter 3, for example, we show how to solve the inverse problem of finding the depth of subsurface

single-walled carbon nanotubes (SWCNTs) using a finite element model. This was presented in the case of subsurface images obtained using contact-resonance AFM and KPFM. Similarly, a recent study uses finite element computations to estimate the depth sensitivity of KPFM, applied for imaging subsurface SWCNTs in a low dielectric polymer matrix [109].

Relevant parameters for the physics of the problem can be varied using computational models. From this type of analysis, a surrogate model can be derived to solve the inverse problem of finding quantitative sample properties. In general, a surrogate model, also known as response surface model (RSM), determines a functional analytical relationship between the outputs and inputs of multivariable complex systems [172]. A computational model mimics the system under study, which predicts the response of an output variable subject to certain input conditions. The computational data set is then used to derive an analytical expression approximating the behavior of the system. For instance, in this study, the response variable is the electrostatic force interactions (F) developed in the microcantilever-sample system. This force can be expressed by

$$F = f(x_i, \theta_j), \tag{4.1}$$

where x_i and θ_j correspond to the set of input or predictor variables and a set of parameters, respectively. In this study, the input variables are the depth (d), and radius (r_s) of the subsurface object and the distance from the apex of the tip to the surface of the sample (Z). The two variables d and r_s are the two unknowns of interest. The latter being the only geometric parameter defining a 0D object (sphere). The spheres mimic nanoparticles (NPs), which are considered dispersed on a medium, as in polymer composites. The Z distance is the known (controllable) experimental variable, which can be varied to collect a set of experimental data.

Since an exact analytical relationship describing F in Equation (4.1) is unknown, an interpolation function $g(x_i, \beta_k)$ is found that approximates closely the force. The β_k would correspond to the coefficients of the function. Parametric computations determine F numerically as a function of the x_i's. These in combination with a

regression algorithm are useful to create $g(x_i, \beta_k)$. The approximate analytical model $g(x_i, \beta_k)$, can the be used to solve the inverse problem and reconstruct the size and depth of the 0D objects. To this end, some assumptions must be considered in the model so that the response surface is locally smooth and single-valued.

The computational model assumes there is one single embedded 0D object right below the tip. It is considered that there are no other particles in a close range that influence the value of F. These conditions give single-valued responses, i.e. the force is unique for a combination of size, depth and tip-sample distance.

4.1.1 Parametric Computations

A full multiparameter sweep in Comsol Multiphysics leads to the calculation of the electrostatic force under a range of values for the x_i's. In this case, the ranges of interest for Z, d and r_s are between 10 to 100 nm with steps of 10 nm, 10 to 100 nm in steps of 10 nm and 15 to 55 nm in steps of 5 nm, respectively.

The geometry of our problem has a convenient symmetry. This fact allows us to simplify the 3D model to a 2D axisymmetric model, reducing the computational cost. Figure 4.1(a) indicates a revolution of the created geometry, around the vertical axis. Three main domains can be distinguished, the surrounding air (prescribed as an infinite element domain), the AFM probe and the sample. Similar as described in Chapter 2, the tip of the probe is composed by a hemispherical apex and a conical section, attached to the distal end of the micro microcantilever modeled as a disk, as shown in figure 4.1(b). The dimensions of these parts correspond to the probe used during the experimental run (NanoWorld, EFM Probe). A detailed description of the probe and simulation parameters are given in Appendix B.1.

The tip is at a variable distance Z above the surface of the sample. The latter consists of a block of a low dielectric matrix with an embedded sphere of radius r_s at a depth d. This geometry approximates the model sample with nanoparticles buried in a polymer matrix.

The physics of the model is defined by the following conditions:

1. Charge conservation is specified for all domains ($\mathbf{E} = -\nabla V$, $\nabla \cdot (\epsilon_0 \epsilon_r \mathbf{E} = \rho_v)$), where $\mathbf{E}$, V, ρ_v, ϵ_r are the electric field, electric potential, charge density and relative permittivity, respectively).

2. The axial symmetry condition is established around the z axis.

3. There is zero charge in the boundaries of the air domain ($\mathbf{n} \cdot \mathbf{D} = 0$, where $\mathbf{D}$ is the electric displacement field).

4. The initial value of the electric potential distribution in all the domains is equal to 0 V.

5. The boundaries of the probe are defined within a terminal node at an electric potential $V = V_t$.

6. The boundary at the bottom of the sample is grounded ($V = 0$ V).

Figure 4.1(b) shows a zoom-in of the 2D surface electric potential distribution. The contours correspond to the electric field lines between the apex of the probe and the buried sphere. The dielectric constants of the sphere and the surrounding matrix are 1500 and 2.5. These values are characteristic of the barium titanate nanoparticles ($BaTiO_3$ NPs) and the polydymethilsiloxane (PDMS), both used in the sample for experimental validation.

The computation of the electrostatic force (response variable) on the probe, for all the combinations of the x_i's is given by

$$\mathbf{F} = \int_{\partial\Omega} 2\pi r \mathbf{n} T dS \tag{4.2}$$

where $2\pi r$ is a volume factor accounting for the 2D axial symmetry condition and $\mathbf{T}$ is the Maxwell stress tensor as detailed in Appendix A.2.

4.1.2   Response Surface: Model-Building

Different approaches can be considered when building an adequate functional relationship between the response variable (F) and the predictor variables (Z, d and r_s). Suitable transformations to these variables, namely choice of metric, facilitate interpretation and comparison with experimental data [172]. For instance, a non-dimensionalization is applied to the electrostatic force using

$$\tilde{F} = \frac{F_{\text{sphere}}|_{Z_i}}{F_{\text{sphere}}|_{Z_{ref}}}, \tag{4.3}$$

where F_{sphere} is the force measured when the tip is above the embedded sphere. The subindex Z_i with $i = 1, 2, ...n$, refers to different values of tip-sample distances (¡ 100 nm), and Z_{ref} is a reference distance far from the surface of the sample, typically equal to 100 nm. The ratio given by Equation (4.3) is calculated over the sphere itself. The polymer is not considered, since it is not likely to encounter neat polymer in a composite without the influence of buried spheres. Furthermore, the non-dimensionality allows a direct conversion of the experimental variable ($A_{2\omega_e}$) to the force. This is because the ratio cancels the terms related to the microcantilever dynamics, when converting $A_{2\omega_e}$ to force, as discussed in Chapter 2.

The relationship between $\tilde{F}$ and the two inputs Z and d, can be represented by a smooth and single-valued surface, as shown in figure 4.2(a). This response surface corresponds to a fixed value of $r_s = 20$ nm. Furthermore, $\tilde{F}$ as a function of transformed variables $\hat{Z}$ and $\hat{d}$ as shown in figure 4.2(b), where $\hat{Z} = \ln(Z)$ and $\hat{d} = \ln(d)$, indicates that a close approximation can be obtained by using low degree polynomials. $\tilde{F}$ as a function of $\hat{Z}$, $\hat{d}$ and r_s can be locally approximated by a second order polynomial model of the form

$$g(x_i, \beta) = \beta_0 + \sum_{m=1}^{i} \beta_m x_m + \sum \sum_{m<n} \beta_{mn} x_m x_n + \sum_{m=1}^{i} \beta_{mm} x_m^2 + \zeta, \tag{4.4}$$

where $i = 3$ and ζ are the residuals. The above expression can be thought of as a truncated Taylor's series expansion of the true underlying theoretical function describing $\tilde{F}$ [173]. Estimates of the β_m coefficients are found using the method of least

squares [174] on the computational data set. Other approximations used for $g(x_i, \beta_m)$ are given in Appendix B.3.

Figures 4.2(c) and (d) show the predicted values of $\tilde{F}$ using the interpolation function given in Equation (4.4) and the obtained residuals. This plots indicate that it is possible to represent $\tilde{F}$ moderately well, i.e. the difference between the predicted and computed values $\tilde{F}$ is on the order of 10^{-2}, over the region of interest of the input variables.

4.2 Experimental Procedure

4.2.1 Subsurface Data Set

Resonance-enhanced 2nd-harmonic KPFM allows the observation of nanofillers in a matrix, based on capacitance gradient variations, as described in Chapter 2. The latter is influenced by probe geometry and the sample properties, such as shape, dimensions and spatial location of the embedded objects.

Double-pass mode allows the variation of one of the input variables, Z, in a relatively straightforward way, using the so called lift or nap height (ΔZ). Therefore, a set of two-dimensional subsurface maps, generated from the amplitude response of the microcantilever at the 2nd harmonic of the electrostatic force ($A_{2\omega_e}$), can be collected at different ΔZ_i (index i is used for the iterations). $\tilde{F}_{exp}$ is then calculated after identification of the subsurface nanoparticles, at each Z_i. The reference tip-sample distance Z_{ref} is defined equal to 100 nm.

4.2.2 Determination of Tip Radius

Electrostatic forces are associated with long range interactions, therefore the geometry of the probe must be considered within the analysis of quantitative data [175]. At small Z distances, on the order of the tip radius, the major contribution to the electrostatic force, comes from the tip-apex. This is defined by its radius, which can

be determined by: direct imaging, deconvolution techniques or fitting analytical expressions derived for conductive substrates [175]. Here, we use high-resolution SEM to determine the effective radius of the AFM probe. SEM images of the probe before collecting the experimental subsurface data set, are given in appendix B.1.

4.2.3 Model Sample

One relevant step within the development of the reconstruction approach is a system of validation. In this case, we propose the use of a model or calibration sample. This consists of nanoparticles (spheres) of known size, embedded in a polymer at a known depth, as shown in the schematic of figure 4.3(a).

We use barium titanate nanoparticles ($BaTiO_3$-NPs) (US Research Nanomaterials, Inc), with an specified nominal size of 50 nm and dielectric constant of 1500. A $0.05wt\%$ of these NPs is dispersed in a solution of ethanol, isopropanol and Triton X-100 by ultrasonication. Then, they are deposited on a gold coated glass substrate by spin coating. An AFM topography image of a region of interest (ROI) is shown in figure 4.3(b).

Subsequently, the NPs are coated with a thin film of PDMS (Sylgard 184, Dow Corning). The two components of the polymer (base and curing agent) are mixed in hexane, using a mass ratio of 1:10:1000, respectively. This solution is spin coated over the sample using 6000 rpm for 180 seconds. Lastly, the sample is heated at 120 ° C for 20 minutes. Figure 4.3(c) shows the topography of the ROI after the PDMS coating. The thickness of the PDMS film is measured from the topography taken at an interface between the substrate and the polymer as shown in figure 4.3(d). The thickness of this sample is approximately 106 ± 2.3 nm. The dielectric constant of the PDMS is 2.68 (at 100 kHz). Some challenges in sample fabrication are a flat surface topography with no particle features and a good dispersion of NPs.

4.3 Results and Discussion

The surrogate model obtained for $\tilde{F}$ as a function of the three input variables ($\hat{Z}$, $\hat{d}$, r_s), is given by

$$\tilde{F}_{pred}(\hat{Z}, \hat{d}, r_s) = b_0 + b_1\hat{Z} + b_2\hat{d} + b_3r_s + b_{12}\hat{Z}\hat{d} + b_{13}\hat{Z}r_s + b_{23}r_s + b_{11}\hat{Z} + b_{22}\hat{d} + b_{33}r_s, \quad (4.5)$$

where the coefficients b_{ij} are found with an n-dimensional polynomial fitting algorithm based on the method of least squares. The data is well represented by the above function, in the region defined by $10 < Z < 100$ nm, $10 < d < 100$ nm and $15 < r_s < 55$ nm, as indicated in figures 4.1(c-d). The coefficient of determination (R^2) is equal to 0.99, used as a general parameter to determine fit adequacy. Table 4.1 gives a summary of the fitting parameters.

Experimentally, $\tilde{F}$ is determined by the ratio of $A_{2\omega_e}$, measured when the tip is above the buried sphere at a distance Z and at a distance $Z_{ref} = 100$ nm. The variable Z is controllable using KPFM in double-pass mode and the remaining two unknowns are d and r_s. These quantities can be found solving the interpolation function given in Equation (4.5), with at least two experimental values of $\tilde{F}$ ($\tilde{F}_{exp}$) obtained at two different Z_i.

The validation of the proposed approach is performed on the model sample previously described. From the topography image taken before the PDMS coating (figure 4.3(b)), we can identify with certainty the size and location of the BaTiO$_3$ NPs (or isolated agglomerations) in the ROI. The height of the features marked from P1 to P8 are 54.2, 82.1, 58.9, 67.7, 107, 137.5, 51 and 36.3 nm, respectively.

After coating, the same ROI is located and imaged using KPFM. The two main observables are shown in figure 4.4(a-b), corresponding to the topography obtained during the 1st-pass and the subsurface map from the 2nd-pass, respectively. The polymer coating is approximately 106 nm (figure 4.3(c)). Therefore, it is expected P5 and P6 to appear on the surface topography, as it happens in figure 4.4(a). There is no evidence of other particles in topography, (P1, P3, P7, P8), but they do appear in the subsurface map. A light protuberance (< 5 nm) is exhibited for particles P2

and P4, which are detailed in the profiles in figure 4.4(c). For evaluation of size and depth, we use the particles marked from P1 to P5. P7 and P8 are not considered. Although they are detected in figure 4.4(b), this corresponds to the subsurface map taken at the lowest value of Z used during experiments. For higher Z, P7 and P8 exhibit a weak $A_{2\omega_e}$ response. These are the smaller NPs of the ROI buried at ≈ 60 and 70 nm.

A sequence of experimental data is collected at different values of ΔZ_i, during the 2nd-pass, as indicated in figure 4.5(a). The reference for ΔZ_i is Z_0, which is the setpoint used during the 1st-pass. The $A_{2\omega_e}$ maps are shown in figure 4.5(c). These are obtained using a conductive AFM probe (EFM from NanoWorld) with a tip radius of $r_t = 31.2 \pm 2.6$ nm. The latter estimated by SEM images (see Appendix B.1).

In the post-processing of the images, a mask is used to locate each of the spheres. $\tilde{F}_{exp}$ is calculated from the maximum values of $A_{2\omega_e}$, as a function of Z_i (Equation (4.3)). Figure 4.6(a) shows the obtained $\tilde{F}_{exp}$ corresponding to the particles P1 to P5 (scatter points). The surrogate model (Equation (4.5)) is then used to find the estimates of size and depth. A fitting algorithm using least squares is applied to the experimental data set. The predicted response is indicated by the curves (lines) in figure 4.6(a), which follow the experimental data. A good fit with $R^2 = 0.99$ is found in all cases. The residuals of the fit are in the order of 10^{-3}, as shown in figure 4.6(b).

Table 4.2 shows the estimated size and depth of P1 to P5 in the ROI. The expected r_s is calculated from the height of the particles measured in the model sample before coating. The expected d is calculated from the difference between the measured thickness of the PDMS coating (figure 4.3(d)) and the height of the particles. The error percentage for the estimates of r_s and d, in the case of the coated particles (P1 to P4), is between 1 to 6 %.

In principle, the proposed approach works for isolated or a cluster of particles separated from one another, as is the case of the model sample. This follows the assumptions made in the computational model, where the force is calculated for a single 0D object located under the tip, neglecting the influence of other particles in a

close vicinity. We would like to point out that in the case of a cluster of particles (for instance, P4 or P5), where at least two particles are together or overlap, they would appear as a spherical shaped object with a bigger apparent size. This is explained from a lack of lateral resolution due to the long-range character of the electrostatic force.

There are other type of scenarios that could be considered in the model, where instead of a single particle, multiple individual particles are distributed close to one another. In this case, the force measured over one particle would be the sum of individual contributions, up to a radius of influence, determined by the lateral separation of the particles. This issue would require an analysis of lateral thresholding with inclusion of other subsurface features within the model. Such more complicated situations may require multivalued response surfaces, where the solution may not be unique. Also, it is worth mentioning that although this study is focused on 0D objects described geometrically for one single parameter (radius), the approach can be extended for 1D (nanotubes) or 2D (platelets) objects. The latter, would require the inclusion of other variables within the model.

Within the framework of this study, there are some remaining challenges that we would like to addressed, as follows:

1. Other input variables are considered to be included within the surrogate model, for a more generalized interpolation function. These are the tip radius and dielectric constants of the sample components.

2. We can determine the range of values at which the input variables should be evaluated by means of a design of experiments method. This would reduce the number of simulations needed to build the surrogate model.

3. Ideally, a model sample would require individual particles, uniformly distributed over a conductive substrate. However, there is still a challenge in achieving this over the gold coated glass. We consider that the roughness of the latter affects the distribution of the particles. Therefore, particle dispersion and deposition is

one of the aspects to improve. Additionally, we consider a second set of samples including two different thickness of polymer coating.

4. As mentioned above, the model considers a region where there is a single particle with no closer particles, at least in a radius of influence to the interaction force sensed by the tip. From the simulations in Chapter 2, it is estimated that this radius should be at least two times the width of the object. Those simulations are for the case of similar cylinders at the same depth. An equivalent analysis should be performed for 0D objects to determine a lateral threshold, that defines until what extent the force pertains to one particle, i.e. the minimum separation between two NPs. This would be useful to establish a relation between lateral separation and the percentage of contribution, as a function of the depth.

5. After validation, the surrogate model based approach can be used in a (0D) polymer composite film, made of $BaTiO_3$ nanoparticles embedded in PDMS [150], to estimate the distribution of particles, size and depth. Subsurface images of this composite are presented in chapter 2.

6. Using image processing we would like to construct quantitative 3D volume images from the stack of 2D images, where depth and size are assigned.

4.4   Summary

The constructed surrogate model approximates the response of the electrostatic force as a function of the input variables, Z, d and r_s. The second order polynomial is a close representation, at least in the domain comprised by the given values of the input variables. From the experimental data set and the interpolation function, the estimates of size and depth obtained for the 0D objects embedded in the low dielectric matrix, are in agreement with the expected values in the validation sample. This approach could be extended for the quantitative determination of other sample

properties and other detection mechanisms. Therefore, we would like to continue with the exploration of the proposed method and estimate its limitations and applicability.
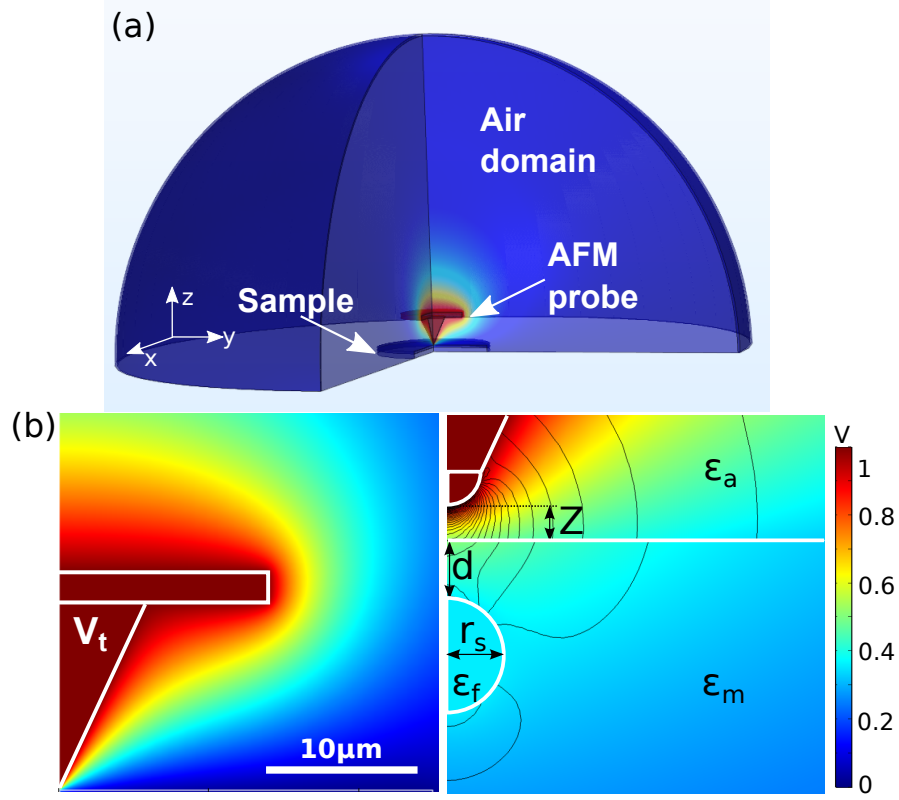
Figure 4.1. (a) Geometry of the 2D axisymmetric model in Comsol Multiphysics. (b) 2D surface plot of the electric potential distribution between the biased probe (at a voltage V_t) and the sample. (c) The zoom-in indicates the variables used in the parametric sweep: tip-sample distance (Z), radius (r_s) and depth (d) of the sphere. Other parameters are kept constant, such as the tip radius (r_t) and the dielectric constants of the surrounding air domain, the polymer matrix and the sphere, $\epsilon_a = 1$, $\epsilon_m = 2.5$, and $\epsilon_f = 1500$, respectively.
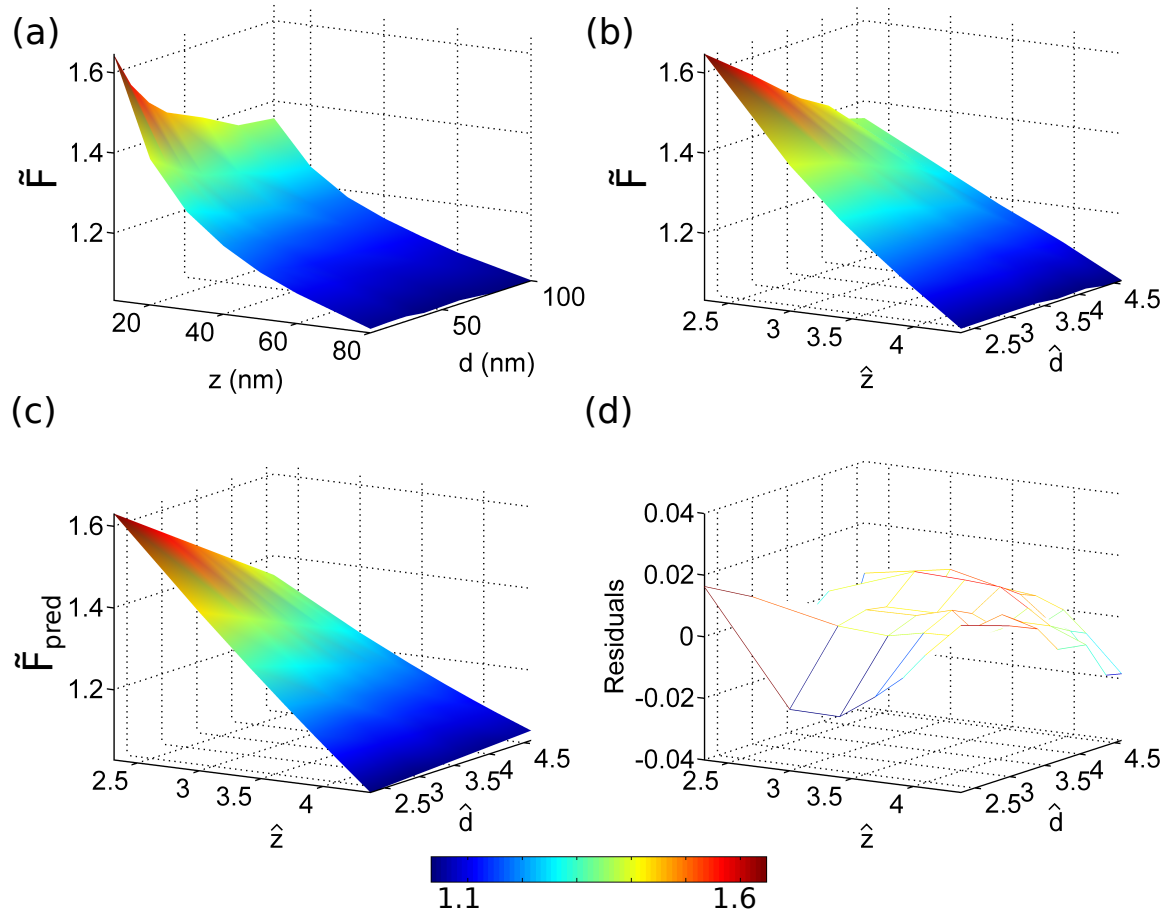
Figure 4.2. Response surfaces of $\tilde{F}$ as a function of input variables. For visualization purposes, one input variable is kept constant, $r_s = 20$ nm. (a-b) Computed $\tilde{F}$ obtained from the parametric sweep in Comsol, as a function of Z and d and the tranformed variables, $\hat{Z} = \ln(Z)$ and $\hat{d} = \ln(d)$, respectively. (c-d) Force ratio and residuals calculated using the surrogate model ($\tilde{F}_{pred}(\hat{Z}, \hat{d}, r_s)$), as a function of $\hat{Z}$ and $\hat{d}$.
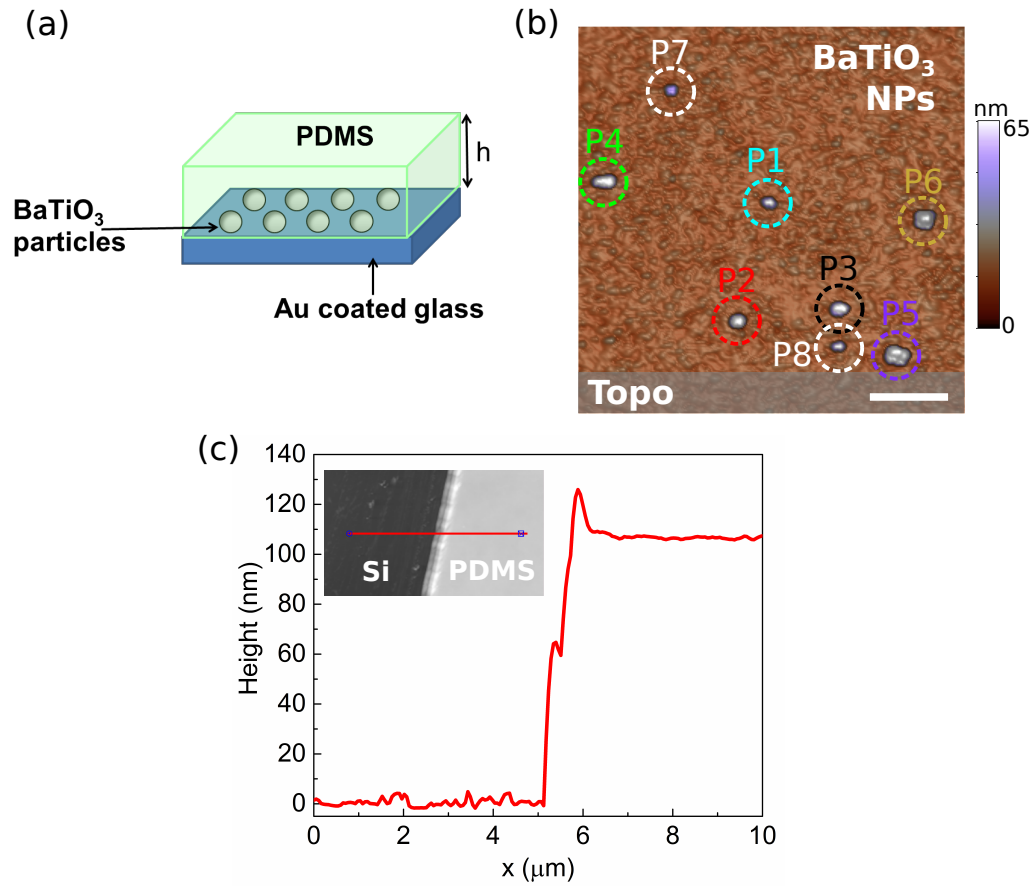
Figure 4.3. Model sample for validation of reconstruction approach. (a) It consists of $BaTiO_3$ nanoparticles deposited over a gold coated glass (substrate) and then coated with a thin layer of polymer (PDMS). (b) Topography of a selected region (ROI), it shows the nanoparticles over the substrate before coating. These are marked with the labels P1 to P8 (scale bar: 1 μm). (c) Measurement of thickness of the PDMS film. The inset shows the topography of the boundary (silicon/PDMS) where the value was measured. PDMS was spin coated under the same conditions in the model sample (6000 rpm / 180 secs, mass ratio: 1:10:200 of curing agent, base and hexane). The thickness of the PDMS is 106.5 ± 3 nm.
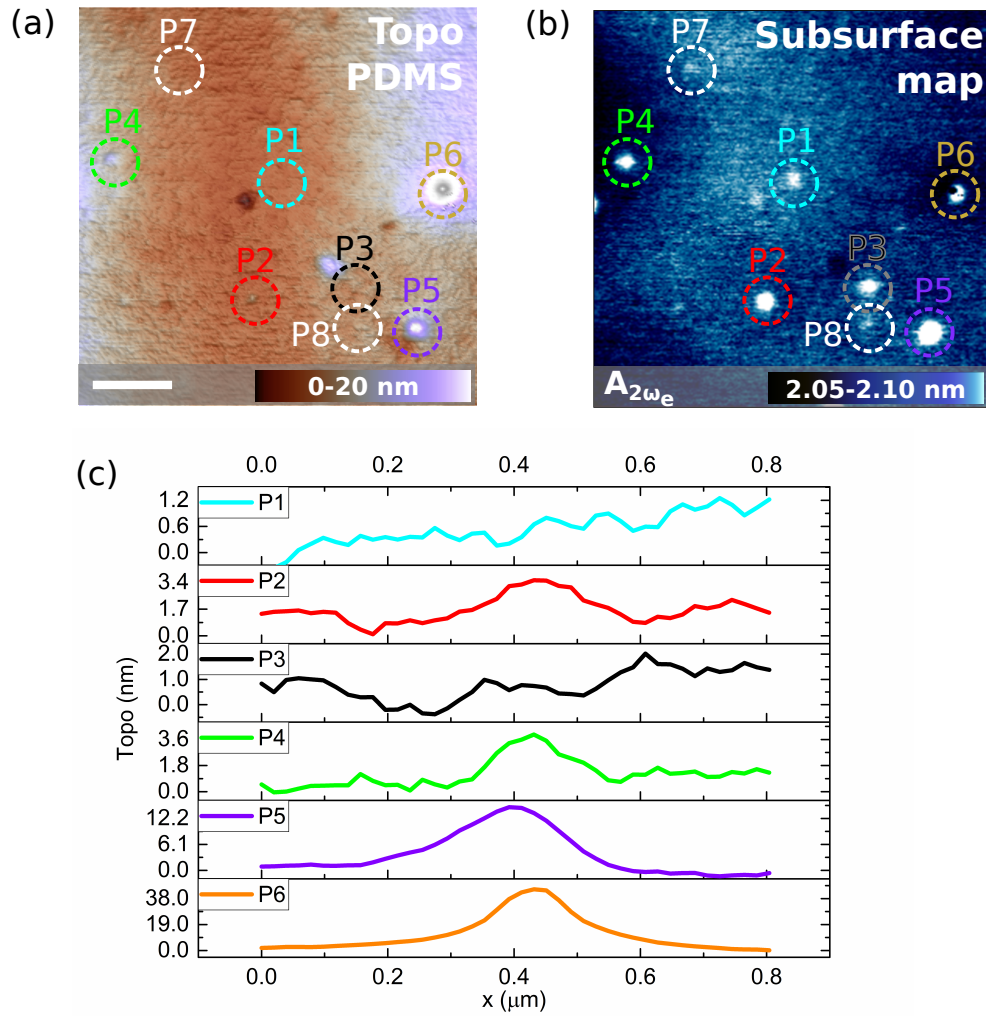
Figure 4.4. Identification of subsurface 0D objects in the ROI of the model sample using double-pass KPFM. (a) Topography after coating with a thin film of PDMS (scale bar: 1μm). (b) Subsurface map corresponding to $A_{2\omega_e}$. (c) Profiles taken in the topography image in (a), corresponding to the central positions where the spheres are buried.
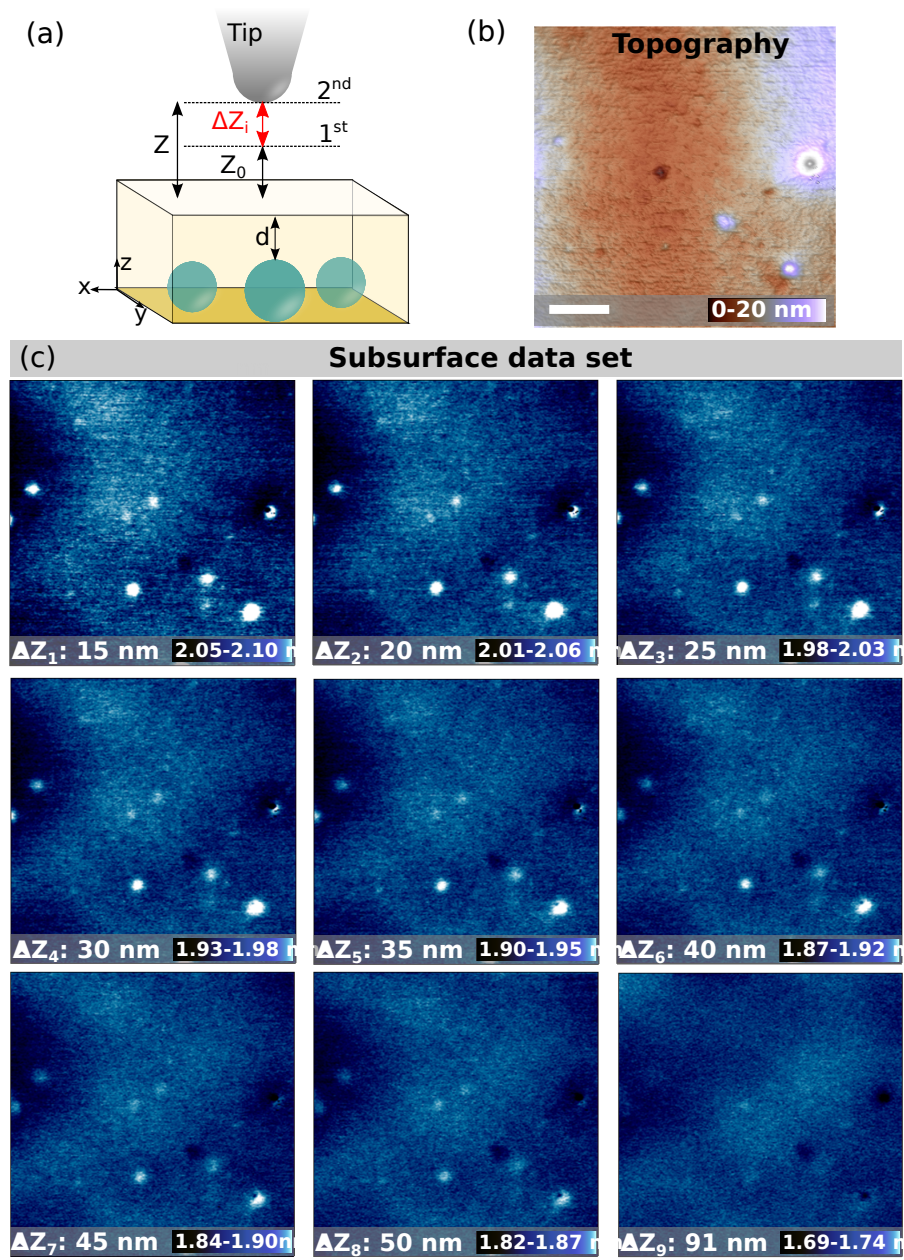
Figure 4.5. Experimental subsurface data set taken on the model sample at different nap heights (ΔZ_i). (a) Schematic diagram of experimental set-up in double-pass KPFM. (b) Topography of the ROI obtained during the 1st-pass at $Z_0 = 9.1$ nm (scale bar: 1 μ m). (c) Subsurface data set taken during the 2nd-pass, varying Z.
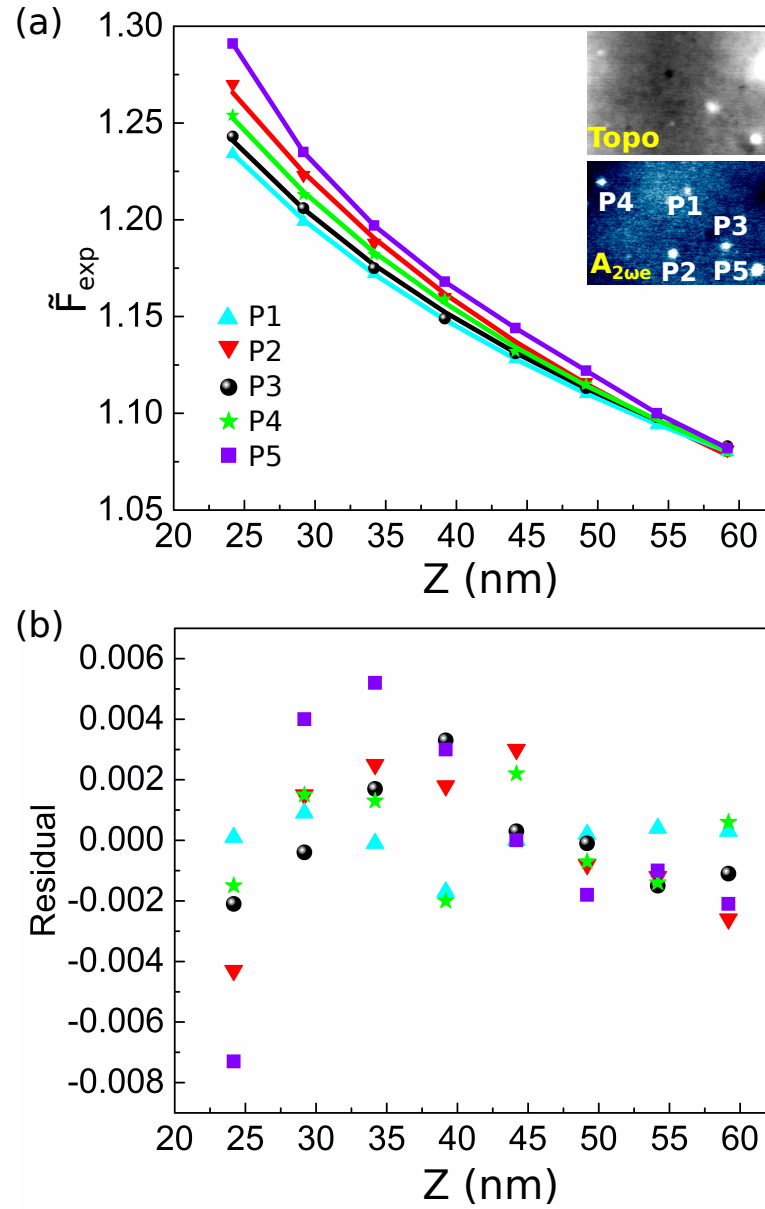
Figure 4.6. Validation of surrogate model from experimental data taken on model sample. (a) Force ratio as a function of Z for five of the particles indicated in the subsurface image of the inset. The scatter points and the lines correspond to the experimental data and the fitting from the experimental data set and the interpolation function, where $\hat{d}$ and r_s are the unknowns.

Table 4.1. Parameters obtained for the second-order polynomial function using least squares (σ: standard deviation, RMSE: root mean square error.)

		Values	σ
Coeff.	b0	3.087	0.034
	b1	-0.540	0.011
	b2	-0.239	0.010
	b3	-0.004	0.001
	b12	0.063	0.001
	b13	4.1×10^{-4}	1.3×10^{-4}
	b23	-3.7×10^{-5}	1.1×10^{-4}
	b11	0.014	0.001
	b22	-0.004	0.001
	b33	1.8×10^{-5}	1.4×10^{-5}
R^2		0.995	
RMSE		0.009	

Table 4.2. Estimation of size and depth of the BaTiO$_3$ NPs located in the ROI of the model sample.

	Expected values		Estimated values		% Error	
	r_s (nm)	d (nm)	r'_s (nm)	d' (nm)	r_s	d
P1	27.4	51.6	28.6	54.5	4.4	5.7
P2	41.4	23.7	42.1	22.2	1.8	6.1
P3	29.8	46.9	30.4	46.0	2.2	2.0
P4	34.2	38.1	32.6	36.5	4.7	4.2
P5	53.8	-1.2	48.7	13.9	9.6	—

5. 3D RECONSTRUCTION USING SUBSURFACE CONTACT RESONANCE ATOMIC FORCE MICROSCOPY (CR-AFM)

5.1 Introduction

Previous chapters have focused on exploring the physics of subsurface imaging with AFM and determining its depth and lateral resolution. However once the subsurface objects are revealed in images many properties remain to be determined: how deep is the object? what size and shape is the object? by how much are its physical properties different from the surrounding matrix? In this chapter we exploit surrogate modeling to reconstruct the properties of subsurface features from AFM data. Surrogate models are applied in different fields, to deal with systems where the exact relationship of the output or response variable and the input or predictor variables is not known or computationally expensive to ascertain [176–181]. Chapter 4 presents a preliminary surrogate model based approach with direct application to KPFM, which is based on the electrostatic force interactions between the AFM probe and a buried object. Preliminary results show that the approach is useful to estimate the size and depth of buried nanoparticles, within 1 to 6% of error.

In chapter 3 we present a direct comparison of CR-AFM with KPFM for subsurface imaging applications. The highly localized stress field that develops in CR-AFM, offers advantages in solving the inverse problem for 3D reconstruction compared to KPFM. Measurements of sample contact stiffness are very localized and are confined to the region of contact between the apex of the tip and the surface of the sample [167].

Hence, here we present a methodology to reconstruct the properties of subsurface objects from imaging with CR-AFM. Due to the complexity of the problem on its own, as a proof of concept, we chose a simplification on the subsurface geometry. We assume there is a 0D object (sphere), geometrically represented by one parameter, its

radius, located at a certain depth in a semi-infinite matrix. This mimics the configuration of nanocomposites where spherical nanometer-sized particles are embedded within a block of polymer. In particular, we consider the case where there is an interest to know the location of the nanoparticles and the quantification of their size and depth after the fabrication process.

We explore the mathematical form of two types of surrogate models to describe the functional relationship between the observable, in this case the contact stiffness, and the main physical parameters related to the tip-sample geometry and mechanical properties. The first model is based on a pure mathematical approach that considers a polynomial response surface [172], while the second model is built using physical principles in contact mechanics [182].

To develop these models, a data set is required which provides an output or response variable as a function of the main input or predictor variables. For this purpose, we use computer experiments, which are more feasible and less expensive in comparison to physical experiments [183]. These offer flexibility to recreate scenarios where the output variable can be computed over a range of input variables. Furthermore, to fully validate the surrogate model approach, we developed a well characterized sample that provided experimental results which could be directly compared to the surrogate model.

This chapter is divided as follows. Section 1 describes the construction of the surrogate models from computer experiments. Section 2 presents the methodology to estimate the geometrical properties of the subsurface 0D object using the surrogate models built in Section 1. This is shown in the case of calculated contact stiffness under simulated scenarios. Section 3 presents the validation on experimental data with CR-AFM using a model sample with particles at a known depth. Section 4 presents a discussion about the challenges and prospective improvements of the surrogate model approaches for 3D reconstruction in subsurface imaging using AFM.

5.2 Construction of the Surrogate Model

5.2.1 Computer Experiments

The first step in developing a successful surrogate model is the identification of the main input and output variables in the context of CR-AFM. As described in Chapter 3, CR-AFM relies on a nano-mechanical modulation of the surface elasticity due to buried objects. During experiments, the tip is brought into contact with the sample at a normal force, while an ultrasonic excitation is applied to the bottom of the sample. Using a dual AC resonance tracking (DART) mode in the Cypher AFM, we measure changes in the contact-resonance frequency (CR-Freq), which is proportional to the sample contact stiffness [100, 162, 163].

The main output variable in CR-AFM is the contact stiffness (k^*). It depends on the applied load (F), the tip radius (r_t), the elastic modulus of the buried sphere (E_p), the elastic modulus of the polymer (E_m), the elastic modulus of the tip (E_t), the radius of the 0D object (particle) (r_p) and its depth (d). These variables are identified in the schematic shown in figure 5.1(a). F is considered as the input controllable variable, analogous to the tip-sample distance used in KPFM (chapter 4).

Once the main variables are defined, the second step is to specify all the configurations to be simulated according to the ranges of each input variable. For this purpose we use Latin Hypercube sampling (LHS), which is a space filling statistical method to design experiments. In LHS each variable has the same number of levels (or points) which is equal to the number of runs in the design. LHS spaces the levels between the lower and the upper bound of every variable in an even manner. The levels are chosen with the criteria to maximize the minimum distance between them [184]. The LHS consists of 300 computer simulations, and it is defined using the ranges of the main input variables given in Table 5.1.

The configuration of input variables are then introduced in the finite element model implemented in Comsol Multiphysics. The geometry of the model as shown in figure 5.1(b) is defined by the tip of the probe, modeled as a silicon hemisphere

(apex), the sample matrix (block with defined width and height) and the embedded
0D object (sphere). The Young's modulus of the materials are assumed constant,
E = 170, 65 and 3 GPa, for the tip apex, the embedded spherical particle and the
polymer matrix, respectively. This model simulates the stress field generated when
the tip exerts a force on the sample as shown in figure 5.1(c). It computes the sample
deformation and the contact force, from which the contact stiffness is calculated.
Since the particles are stiffer, k^* is higher in comparison to the surrounding polymer.
Details on the parameters and boundary conditions are given in Appendix C.2

5.2.2 Surrogate Model Based on a Polynomial Response Surface

One way to model the functional relationship between k^* and the input variables
is to use a polynomial function. A general motivation of polynomials is that they
can be considered as a Taylor's series expansion of the true underlying theoretical
function [172, 176]. Higher order terms are truncated depending of the degree of the
polynomial.

We use a second degree polynomial with a mathematical form defined as [176]

$$y = f(\mathbf{x}, \theta) \tag{5.1}$$

$$= b_0 + \sum_{i=1}^{n} b_i x_i + \sum_{i=1}^{n} \sum_{j=i}^{n} \theta_{ij} x_i x_j, \tag{5.2}$$

where n = 4, y is the output variable (k^*) and x_i are the input variables ($x_1 = r_t$,
$x_2 = r_p$, $x_3 = d$ and $x_4 = F$). The form of the second-order model in Equation
(5.2) describes the main effects of the x_i and the two-way interactions between them.
Equation (5.2) is defined as SM 1. The parameters b_i, also known as regression coef-
ficients, are found by the method of least squares [176]. We use the computed values
of k^* for the different configurations of the x_i defined by the LHS. The variables are
conveniently transformed using the natural logarithm, which improves the represen-
tational capability [172]. The notation for the transformed variables is $\hat{k}$, $\hat{r}_t$, $\hat{r}_p$, $\hat{d}$,
$\hat{F}$.

Table 5.2 indicates the estimated values, the standard error (SE) and the p-value (derived from the t-statistics under the assumption of normal errors). The latter is useful to test the significance of each individual regression coefficient in the model, based on the hypotheses $H_0 : b_i = 0$ and $H_1 : b_i \neq 0$. If H_0 is not rejected, then it indicates that x_i can be deleted from the model [176]. For instance, all the terms, except b_{44}, which corresponds to $\widehat{F}^2$, are significant within a 5% level.

To check the model adequacy, we use the diagnostic plots shown in figure 5.2. Figure 5.2(a) corresponds to the actual $(\widehat{k^*})$ versus the predicted values of the response variable $(\widehat{k^*}_{\text{predicted}})$ which follows a line with slope 1. This means that the predicted response is close to the actual response. Figure 5.2(b) indicates the distribution of the residuals $(r_i = \widehat{k^*} - \widehat{k^*}_{\text{predicted}}, \; i = 1, 2, ..., n)$ with respect to $\widehat{k^*}_{\text{predicted}}$. The r_i are randomly spread around a horizontal line (at zero), suggesting the computational experiments are well modeled by a linear relationship between $\widehat{k^*}$ and the input variables and the variance of the observations is constant for all values of $\widehat{k^*}$. Therefore, it is considered that over the region defined by the ranges of the input variables, SM 1 represents the true function in an adequate manner. Figure 5.2(c) corresponds to the case when the variables are scaled back from the logarithmic transformation.

The response surface in figure 5.3 shows the relationship between the contact stiffness (k^*) and the two variables of the sphere (r_p) and (d), when r_t and F are constant. As expected, maximum values of k^* are achieved at lower d and higher r_p, i.e. bigger particles near to the surface.

5.2.3   Surrogate Model Based on Dimensional Analysis

Dimensional analysis is another approach that has been used to determine relationships between variables when the exact functional relationship is unknown. It relies more on a physical reasoning and a functional form can be defined based on the comprehension of the problem. It is also applied to reduce the number of variables by balancing the dimensions of the variables [179, 184, 185].

We use the Buckingham π theorem to construct a surrogate model using non-dimensional parameters π [184, 186]. These are useful to find a functional dependence of k^* and the input variables. The physical variables involved in the problem and its dimensions are shown in Table 5.1. According to this theorem, the relationship between these variables can be written as some function G such that

$$G\left(\pi_1, \pi_2, \ldots, \pi_p\right) = 0. \tag{5.3}$$

where π_i are dimensionless ratios (π parameters) and p is the number of π products. To find these products we proceed as follows [187].

Considering the variables and its dimensions from Table 5.1, a dimensional matrix is defined as

	k^*	d	r_t	F	E^*	r_p
m	-1	1	1	0	-2	1
N	1	0	0	1	1	0

In this problem, the number of variables is $N_v = 6$, the number of dimensions is $N_d = 2$, the rank of the dimensional matrix is $r = 2$ and $p = N_v - r = 4$. Assume we seek a relation involving the 6 variables and the 2 dimensions that satisfy

$$\left[(k^*)^{e_1} \cdot d^{e_2} \cdot r_t^{e_3} \cdot F^{e_4} \cdot (E^*)^{e_5} \cdot r_p^{e_6}\right] = m^0 \cdot N^0, \tag{5.4}$$

which can be written as

$$\begin{bmatrix} -1 & 1 & 1 & 0 & -2 & 1 \\ 1 & 0 & 0 & 1 & 1 & 0 \end{bmatrix} \cdot \begin{bmatrix} e_1 \\ e_2 \\ e_3 \\ e_4 \\ e_5 \\ e_6 \end{bmatrix} = \begin{bmatrix} 0 \\ 0 \end{bmatrix}. \tag{5.5}$$

The dimensional matrix can be divided into two submatrices as follows

$$\mathbf{A} = \begin{bmatrix} -2 & 1 \\ 1 & 0 \end{bmatrix}, \mathbf{B} = \begin{bmatrix} -1 & 1 & 1 & 0 \\ 1 & 0 & 0 & 1 \end{bmatrix}. \tag{5.6}$$

The linearly independent columns form $\mathbf{A}$ and the remaining columns constitute $\mathbf{B}$. Using these two matrices, the relation in Equation (5.5) can be expressed as

$$
\begin{bmatrix} e_1 \\ e_2 \\ e_3 \\ e_4 \\ e_5 \\ e_6 \end{bmatrix} = \begin{bmatrix} \mathbf{I} & \mathbf{0} \\ -\mathbf{A}^{-1}\mathbf{B} & \mathbf{A}^{-1} \end{bmatrix} \cdot \begin{bmatrix} e_1 \\ e_2 \\ e_3 \\ e_4 \\ 0 \\ 0 \end{bmatrix}.
\tag{5.7}
$$

The first matrix in the right side is known as the exponent matrix ($\mathbf{E}$). Since the number of dimensionless products of variables we can form is four, the relation in Equation (5.7) can be expressed as $\mathbf{P} = \mathbf{E} \cdot \mathbf{Z}$, where

$$
\mathbf{Z} = \begin{bmatrix} e_{11} & e_{12} & e_{13} & e_{14} \\ e_{21} & e_{22} & e_{23} & e_{24} \\ e_{31} & e_{32} & e_{33} & e_{34} \\ e_{41} & e_{42} & e_{43} & e_{44} \\ 0 & 0 & 0 & 0 \\ 0 & 0 & 0 & 0 \end{bmatrix}.
\tag{5.8}
$$

Each row of $\mathbf{P}$ corresponds to the physical variables in the following order: k^*, d, r_t, F, E^* and r_p and each column corresponds to dimensionless products.

To find the dimensionless products, we calculate $\mathbf{E}$ replacing $\mathbf{A}$ and $\mathbf{B}$, and define the arbitrary e_i's in $\mathbf{Z}$ using physical reasoning that comes from the Hertzian contact mechanics model. This model describes the force between an elastic spherical tip with radius r_t in contact with an elastic half space as $F = \frac{4}{3}E^*\sqrt{r_t\delta^3}$, where δ is the indentation [182]. The tip sample contact stiffness is analytically known to be

$$
k^* = \sqrt[3]{6r_t(E^*)^2F}.
\tag{5.9}
$$

Equation (5.9) suggests a mathematical form between k^* and two of the independent variables, F and r_t, given by the cubic root. Therefore, the matrix with the arbitrary $e_i's$ in our problem is defined as

$$\mathbf{Z} = \begin{bmatrix} 3 & 0 & 0 & 0 \\ 0 & 1 & 0 & 0 \\ 0 & 0 & 1 & 0 \\ 0 & 0 & 0 & 1 \\ 0 & 0 & 0 & 0 \\ 0 & 0 & 0 & 0 \end{bmatrix}$$

The final π products we found are

$$\pi_1 = \frac{(k^*)^3}{(E^*)^3 r_t^3}, \quad \pi_2 = \frac{d}{r_t}, \tag{5.10}$$

$$\pi_3 = \frac{r_p}{r_t}, \quad \pi_4 = \frac{F}{E^* r_t^2} \tag{5.11}$$

Combining physical intuition given by the Hertz contact model, the computational experiments, and the dimensionless products, we find a surrogate model that describes k^* in terms of F and r_t such as in Equation (5.9), but also includes the geometrical parameters of the embedded sphere. In terms of the π products, the model is given by

$$\pi_1 = \beta_1 \pi_4 + \beta_2 \frac{\pi_4}{\pi_2} + \beta_3 \pi_3 \pi_4 \tag{5.12}$$

where the β_i's corresponds to regression parameters. Replacing variables, the expression for the surrogate model is

$$(k^*_{\text{predicted}})^3 = c_1 F r_t + \frac{c_2 F r_t}{d} + \frac{c_3 F r_t r_p}{d} + c_4. \tag{5.13}$$

It is noted that now the parameters c_i encapsulate the effective Young's modulus, which is a constant term that depends on the modulus and the Poisson's ratio of the tip, the particle and the matrix [158]. These parameters are found using the method of least squares. The estimates are given in Table 5.3. The independent term represents sources of variability not accounted for k^*. This model is from now on referred as SM 2.

In Figure 5.4 we evaluate the adequacy of the model. Figure 5.4(a) shows that the predicted k^* using SM 2 are close to the actual k^*, this indicates that the model is a good representation of the functional relationship in the region of interest. Figure 5.4(b) presents the residuals with respect to the predicted k^*. They are randomly distributed around the horizontal line (at zero), indicating low variability and that no significant non-linear relationships have been left out in the surrogate model.

5.3 Test of the Surrogate Models Using Computer Experiments

As described above, in a CR-AFM experiment, the main observable is the contact resonance frequency which is quantitatively related to the contact stiffness. The controllable variable is the force applied to the AFM tip. In order to use the two surrogate models to extract the properties of the subsurface object, we propose to measure the contact stiffness at several applied forces and use the mathematical relations given by either SM 1 (Equation (5.2)) or SM 2 (Equation (5.13)) to estimate[1] r_p and d.

First we test this approach using simulations that mimic the case of a real experiment. We calculate k^* at different applied forces, assuming a spherical tip of radius r_t and a sample with an embedded sphere of radius r_p and depth d. As an example, we calculated k^* for the case of having an embedded particle with $r_p = 40$ nm at different values of d. The force applied by the tip with $r_t = 50$ nm is varied starting from 30 nN to 90 nN. The results are shown in figure 5.6, indicated by the scatter points.

Assuming we do not have a previous knowledge of d and r_p, we can use the surrogate models to find them. We consider two cases: 1) where there is only one unknown, the particle depth and 2) when two variables are unknown, the particle radius and depth.

---

[1]Estimated values uses the notation $\widetilde{r_p}$ and $\widetilde{d}$

5.3.1   Case 1: One Unknown

For demonstration purposes we assume no prior knowledge of the depth of the particle. For the cases shown in figure 5.6, we estimate d by SM 1 and SM 2 using least squares fitting of k^* as a function of F. The results are shown in Table 5.4. Both SM 1 and SM 2 are able to effectively predict the value of the depth of the sphere (known from simulations). We calculate the percentage error, which for SM 1 is $< 5\%$ and for SM 2 is $\leq 10\%$.

5.3.2   Case 2: Two Unknowns

Now we test the models in the case where both r_p and d are unknown. We use SM 1 and SM2 for the simulations in figure 5.6 ($r_p = 40$ nm and $d = 15, 25, 35, 45, 55$ nm). we estimate r_p and d using least square fitting. The results are indicated in Table 5.5.

In this case, finding two unknowns is a global optimization problem that often needs a good initial guess for the parameters to converge to a reasonable fit. To overcome this problem we have developed an optimized procedure as described below:

1. Define a lower and upper bound for r_p ($[r_p^{low} \ r_p^{up}]$).

2. Find d using the surrogate model at the lower and upper bounds of r_p ($[d^{low} \ d^{up}]$).

3. Define the initial guess of r_p and d within the lower and upper bound given by $[r_p^{low} \ d^{low}]$ and $[r_p^{high} \ d^{high}]$.

4. Use least squares with the function given by the surrogate model introducing the defined initial guess and bounds.

In figure 5.6(a-b), the solid lines corresponds to the fitting of SM 1 and SM 2, respectively, using the estimated values of d and r_p. For all the spheres, SM 1 and

SM 2 fit the simulations with $R^2 = 0.99$. The dotted line in both figures corresponds to k^* calculated on the polymer matrix in the absence of a particle, with $r_t = 50$ nm.

We include other simulation cases in which r_p and d are varied, as shown in figure 5.7(a). The scatter points correspond to k^* calculated as a function of F. Using the same procedure as before, we use least square fitting to obtain the estimates of the unknowns, which are given in Table 5.6. The solid lines in figure 5.7(a) correspond to $k^*_{\text{predicted}}$ as a function of F. The R^2 is 0.999 in all cases. Figure 5.7(b) shows a 3D representation of each sphere with the estimated r_p and d, assuming they are laterally separated by 80 nm in the x direction.

5.4   Validation on Experimental Data

5.4.1   Model Sample

For validation purposes using CR-AFM data, we fabricated a well characterized composite sample in a sandwich type structure as shown in figure 5.8(a). The fabrication process is as follows:

1. Substrate preparation: a silicon wafer was used as a rigid support substrate. This was cleaned with IPA/acetone/DI water and exposed to UV.

2. Barium titanate $BaTiO_3$ particle deposition: a 0.025wt% solution of $BaTiO_3$ (US Research Nanomaterials, Inc), DI water and surfactant was ultrasonicated for 45 min. After this process, the dispersion was centrifuged at 2000 rpm for 30 min. Then the solution was spin coated on the silicon substrate, previously exposed to UV to increase adhesion of the nanoparticles. The particles are well dispersed on the silicon as it is shown in figure 5.8(b), with an average diameter of 44.6 $\pm$ 17.7 nm. A histogram of the particle size distribution is given in Appendix C.1

3. Thick layer of polystyrene (PS): a 20 wt% solution of PS (Sigma-Aldrich, average MW ~ 350.000) in toluene was spin coated at 3000 rpm for 60 s over the nanoparticles in the silicon substrate. Then annealed for 1 h at 150 °C.

4. Flipping step: the PS layer was peeled off from the silicon substrate. Some of the $BaTiO_3$ particles stuck to this layer as shown in figure 5.8(c).

5. PS coating: a first layer of PS (1.5wt%) was spin coated on top of the flipped side of the sample. The topography is shown in figure 5.8(c), which exhibits protrusions where the $BaTiO_3$ particles are located. To bury the nanoparticles, a second layer of PS is deposited on top. Figure 5.8(d) shows the final topography of the sample.

A calibration sample relies on accurate height measurements which is a difficult task because wetting effects on different substrates produce PS layers of different thickness. To avoid this effect and accurately calibrate the thickness of the PS layer, we rely on measurements of the height of the particles. In figure 5.8(b) the average height of the particles protruding above the anchor layer is 16.4 ± 7.7 nm. After applying a first coat of PS, the particles protruding have a height of 2.7 ± 1.1 nm. This implies the first coat of PS is 13.7 ± 7.8 nm. A second layer was applied and its thickness was measured using a silicon substrate with a PS layer of known thickness. The difference in the thickness of the PS coating after the second coat was applied is 28.1 ± 4.1 nm. Taken together, this means the thickness of the two PS coatings is 41.8 ± 9.3 nm. Since the particles protruded 16.4 nm above the anchor layer, the estimated depth is 19.5 ± 12.8 nm. The largest uncertainty in the measurements comes from the particle size distribution.

5.4.2 CR-AFM Subsurface Data Set

CR-AFM is a dynamic contact mode technique based on measurements of the resonance frequency of a surface coupled AFM microcantilever. As the stiffness of the

sample contact changes, the contact resonance frequency (CR-Freq) varies proportionally. We use the DART mode in Cypher AFM to track the CR-Freq [163], while the tip scans over the sample surface using a scan rate of 0.3 Hz. The experimental setup is described in Chapter 3.

During experiments we use a compliant microcantilever (FORTA from AppNano) with a spring constant of 1.4 N/m and Q = 107.8. The measured free eigenmode frequencies are $f_1^0 = 55.7$ kHz, $f_2^0 = 355.1$ kHz and $f_3^0 = 1.01$ MHz. The optimal eigenmode for subsurface detection needs to be identified and depends on the experimental range of contact stiffness [188]. In this case, we use the third eigenmode frequency of the microcantilever. All measurements were made under ambient conditions.

Subsurface images of the $PS/BaTiO_3/PS$ sample are shown in figure 5.9. There is no evidence of nanoparticles on the surface (figure 5.9(a)), but they are clearly identified on the CR-Freq map (figure 5.9(b)). The surrounding PS appear darker in contrast, i.e. a lower frequency and in turn lower contact stiffness in comparison to the $BaTiO_3$ particles. There are some line marks in the CR-Freq map that indicates tip modification, a common issue in CR-AFM. The tip is prone to wear during experiments in contact with the sample surface [189]. This is a relevant aspect in our experiment, since we scan the same region of the sample several times to get the data at different applied forces. Therefore, the complete data set is acquired in the smaller area shown in figure 5.9 (c-d).

As described in section 2, the required set of data corresponds to k^* as a function of F. A series of CR-Freq maps where taken at F = 20, 30, ..., 70 nN, with steps of 10 nN in between. The sequence of maps is shown in figure 5.10. As expected, CR-Freq increases with higher forces [100].

After the acquisition of the data set, we calculate k^* on each nanoparticle and the surrounding polymer region from each map. For this purpose, we use the theoretical model in [162], detailed in Chapter 3. This model considers the total length of the microcantilever (L), the tip offset (L_1), tip height (h), a lateral stiffness (k_L) and

the tilt angle (α) as shown in figure 3.1. The effective values of the microcantilever geometric parameters are typically found using a calibration sample [158, 190]. In this case, we use the PS region surrounding the nanoparticles. The tip radius is estimated from a high resolution SEM image taken before the experiment, as shown in figure 5.11(a). Figure 5.11(b) shows k^* with respect to force from the experimental data and a simulation using $r_t = 70$ nm. The parameters used in the CR-AFM model are $L = 240\mu m$, $L_1 = 228\mu m$, $h = 12\mu m$, $k_L/k_c = 0.85$, $\alpha = 11°$.

The mean value of k^* as a function of force, for each nanoparticle, is shown in figure 5.12(a). To reconstruct the size and depth of the nanoparticles we can then apply the surrogate models previously discussed. The expected results are: $r_p = 22.3 \pm 8.8$ nm, $d = 19.5 \pm 12.8$ nm. The surrogate model predictions are shown in Table 5.7. The estimation of r_p and d are obtained using SM 1 and SM 2 when F = 30 to 60 nN. At these applied forces, the subsurface maps have a more stable CR-Freq on the polymer regions throughout the scan. With SM 1 and SM 2 the estimations agree with the expected values. Figure 5.12(b) shows a graphical 3D representation of the buried nanoparticles with the estimated size and depth.

5.5 Discussion

The surrogate models SM 1 and SM 2 described in section 2 provide a functional relationship for k^* that explicitly depends on the main input parameters. This relation is expressed in a mathematical form that can be used to find unknown variables. For instance, in section 3, SM 1 and SM 2 are used to find one unknown (d) or two unknowns (r_p and d), given k^*, F and r_t. In principle, the methodology to construct these models is applicable to other AFM techniques. Two main requirements are: a quantifiable observable and the knowledge of the influential predictor variables.

There are still some challenges in the reconstruction approach based on these types of surrogate models. For instance, we face a global optimization problem where there can be multiple local solutions. To overcome this issue we apply constraint bounds to

the variables in the least square algorithm. There are other optimization algorithms for multidimensional systems that can be explored such as particle swarm optimization [191, 192] or genetic algorithms [193]. An alternative solution is to analyze other independent observable aside from k^*. This could be the apparent width of the object given by the full width half maximum (FWHM). Chapter 3 presents a preliminary study where we determine the FWHM as a function of the depth of a buried 1D object [167], when its size is fixed. For the parameters assumed in the simulation, the FWHM is almost constant as a function of depth ($d < 50$ nm). Therefore, using computer experiments with the tip scanning above the embedded object, we can determine FWHM as a function of the input variables, as in the case of k^*. These set of parametric simulations allow the creation of a new surrogate model seek to be linearly independent to the model of $k^* = g(r_t, F, r_p, d)$ built in section 2.

In the acquisition of the experimental subsurface data, we found that CR-AFM is a robust quantitative AFM technique where a highly localized stress field gives the advantage of higher local resolution to resolve subsurface features. However, there are also some remaining challenges. i) The tip is prone to wear while scanning in contact the surface of the sample. ii) There is some cross-talk from topography in the CR-Freq maps. iii) The theoretical model to quantify k^* from the contact resonance frequency requires careful consideration of a calibration sample to find the effective parameters of the microcantilever.

5.6   Summary

This chapter describes a method developed to reconstruct the properties of subsurface objects imaged with CR-AFM. This is based on surrogate models created using computer experiments where a design of the needed configurations is done by LHS. It shows satisfactory results in the estimation of the geometrical parameter describing a 0D object and the distance at which it is located under the surface of the sample. We believe this approach can be applied in more general situations to estimate other

properties and be extended to other geometrical objects such as nanowires, nanorods, or nanoplatelets. The latter involving multi-parameter geometric representations together with large scale computations.
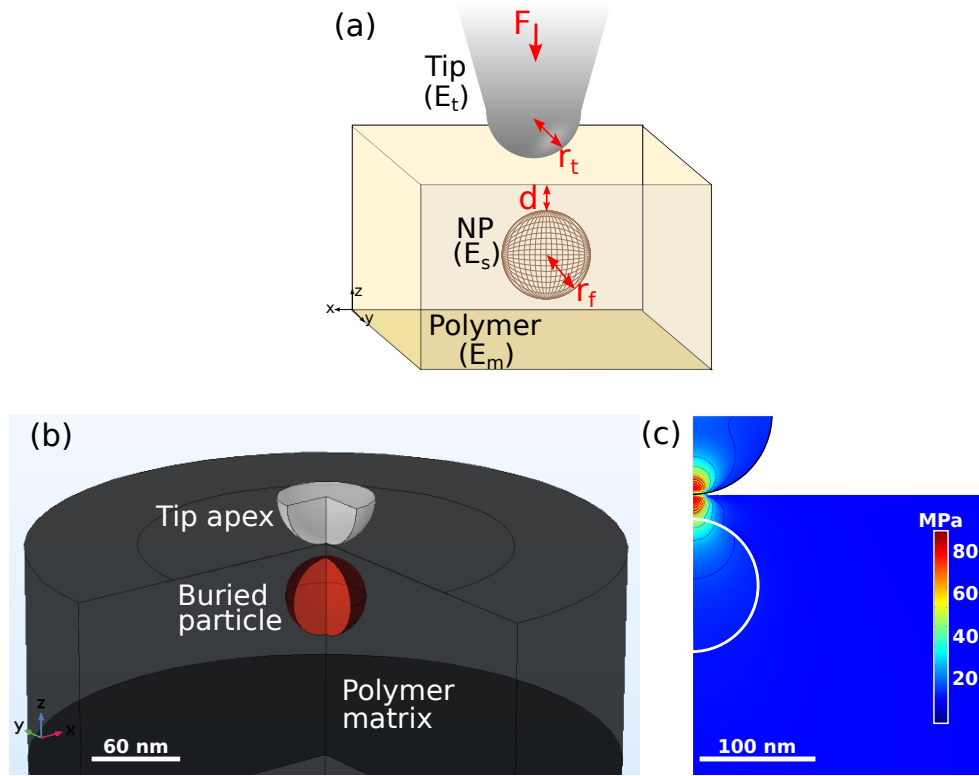
Figure 5.1. Tip-sample geometry. a. Schematic illustrating the main design parameters: applied force (F), tip radius (r_t), nanoparticle depth (d) and radius (r_f). 2D axisymmetric model in Comsol, assuming $F = 40$ nN, $r_t = 65$ nm, $r_f = 54$ nm and $d = 20$ nm. b. 3D representation from the revolution of the 2D axisymmetric geometry in (c). The colors corresponds to the Young's modulus and Poisson's ratio assigned for each material, $E_m = 3$ GPa, $E_f = 67$ GPa, $E_t = 170$ Gpa, $\nu_t = 0.28$, $\nu_m = \nu_f = 0.3$. (c) Von Mises stress surface plot.
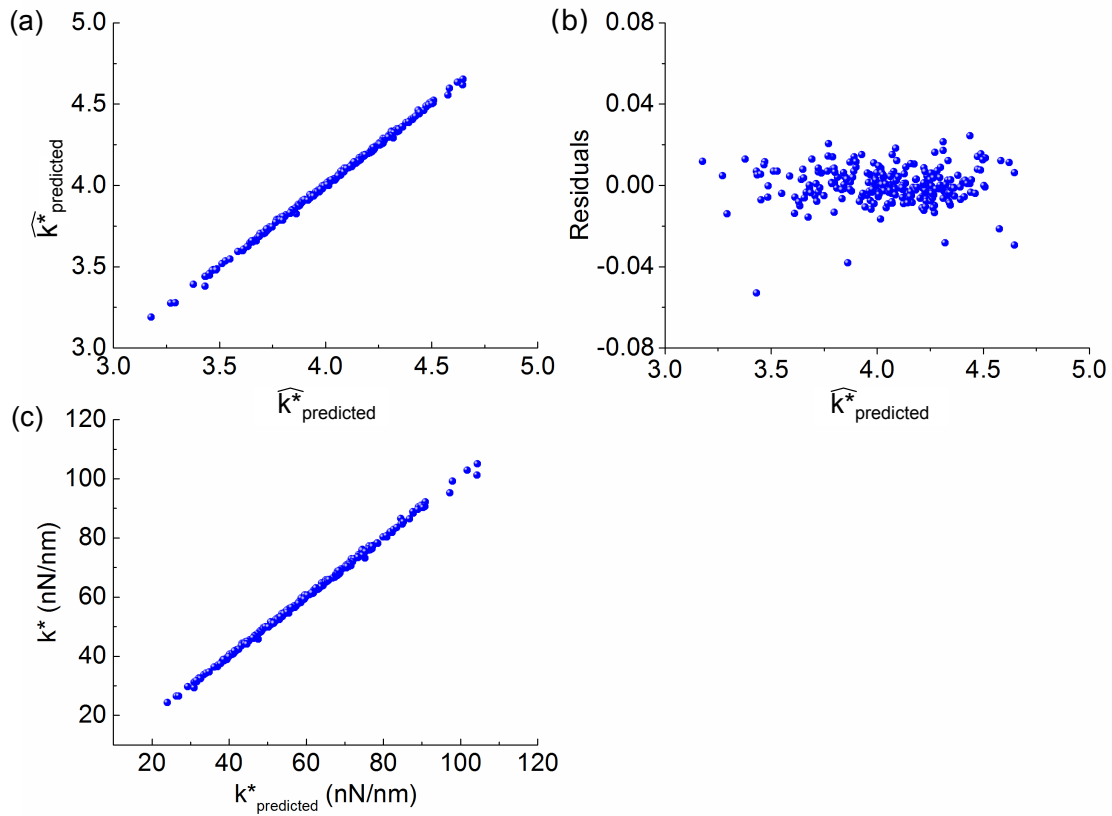
Figure 5.2. Analysis of SM 1 using the predicted response and residuals from least squares regression. (a) Predicted ($\widehat{k^*}_{\text{predicted}}$) versus actual ($\widehat{k^*}_{\text{actual}}$) contact stiffness using transformed variables. (b) Residuals versus $\widehat{k^*}_{\text{predicted}}$ using transformed variables. (c) k^* versus $k^*_{\text{predicted}}$ after transforming the variables back to meaningful experimental quantities.
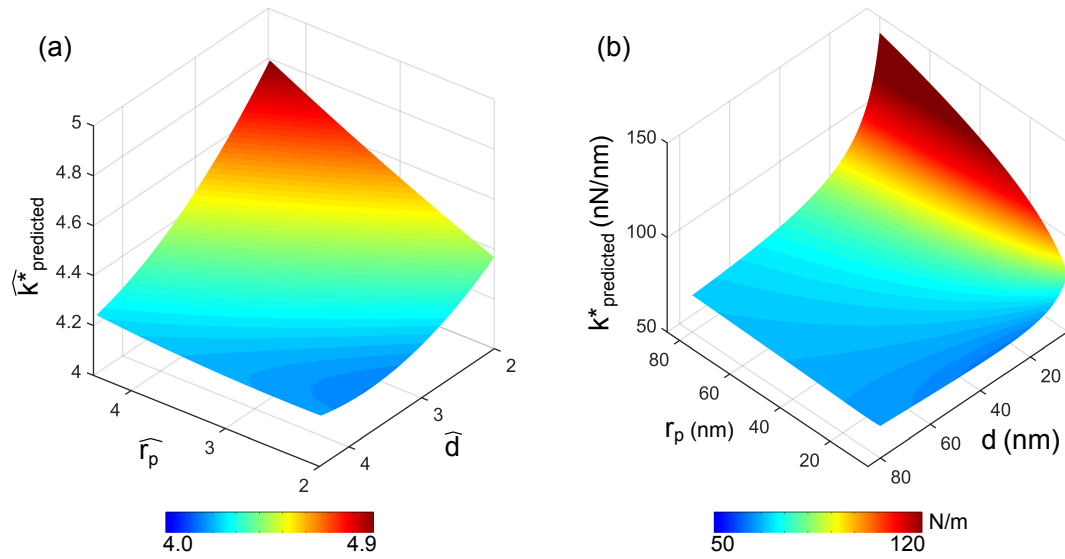
Figure 5.3. Response surfaces from surrogate model given in Equation (5.2). These plots are obtained using a constant $F = 50$ nN and $r_t = 100$ nm. (a) $\hat{k}_{predicted}$ with respect to $\widehat{r_p}$ and $\widehat{d}$. (b) $k_{predicted}$ with respect to r_p and d.
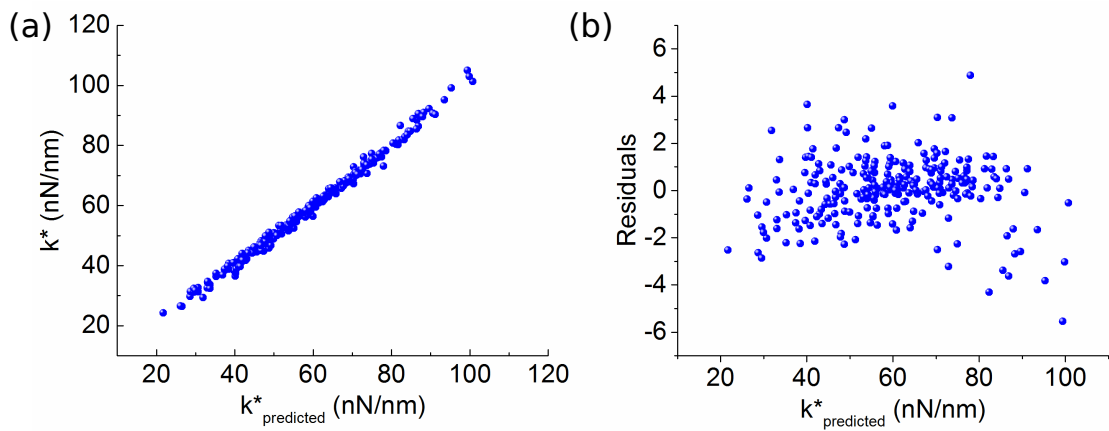
Figure 5.4. Analysis of SM 2. (a) Predicted versus actual k^*. (b) Residuals versus predicted k^*.
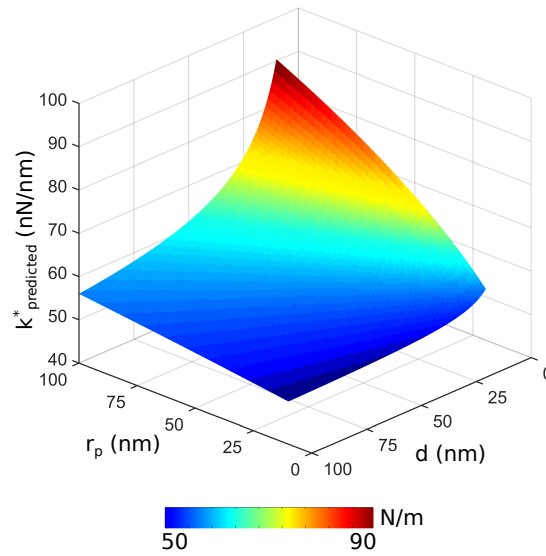
Figure 5.5. Response surface given by $k_{\text{predicted}}$ with respect to r_p and d. This is obtained using SM 2 given in Equation (5.13) using a constant $F = 50$ nN and $r_t = 50$ nm.
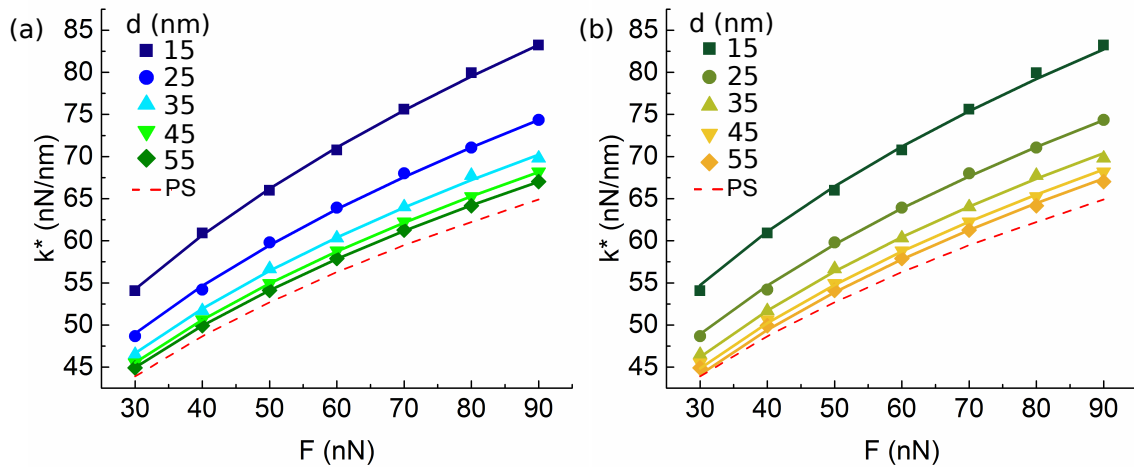
Figure 5.6. Contact stiffness versus applied force in computer experiments assuming $r_t = 50$ nm, $r_p = 40$ nm and $d = 15, 25, 35, 45, 55$ nm. The scatter points correspond to the calculated k^* and the solid line is the corresponding $k^*_{\text{predicted}}$ using (a) SM 1 and (b) SM 2. The dotted line correspond to k^* in the absence of a particle (just the polymer matrix).
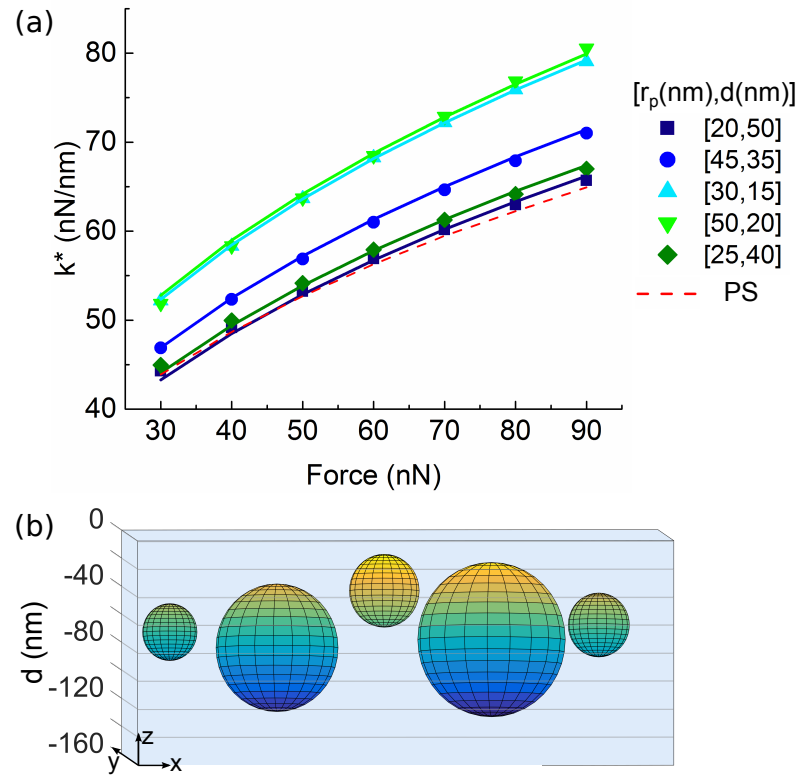
Figure 5.7. (a) Contact stiffness versus applied force in computer experiments assuming $r_t = 50$ nm. Different values are assumed for r_p and d as shown in the legend. The scatter points correspond to the calculated k^* and the solid line is the corresponding $k^*_{predicted}$ using SM 2. The dotted line correspond to k^* in the absence of a particle (just the polymer matrix). (b) 3D graphic where each sphere is plotted with the corresponding estimated r_p and d (z), assuming they are located 80 nm apart from each other in the x axis.
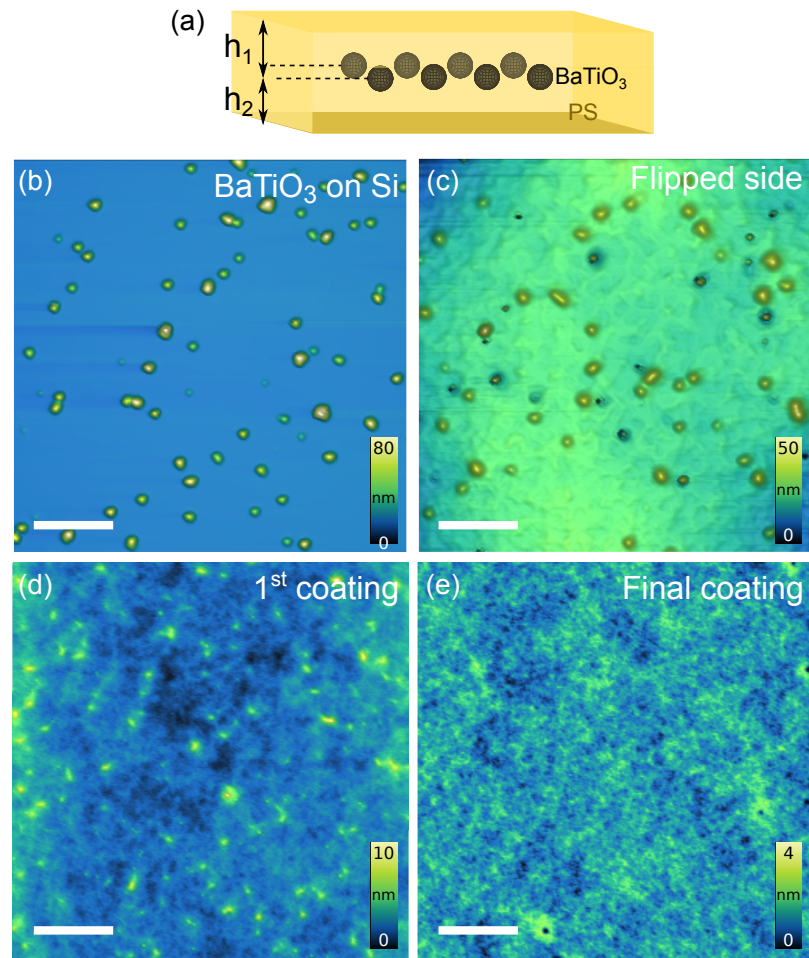
Figure 5.8. Schematic of the model sample and topography maps taken during fabrication steps. (a) Cartoon of the sandwich-type structure. (b) BaTiO$_3$ particles on silicon substrate, the average diameter is 44.6 $\pm$ 17.7 nm (scale bar: 2 μm). (b) Flipped side of the sample indicating stuck BaTiO$_3$ particles in the PS thick layer (scale bar: 2 μm). (c) Surface after first PS coating layer (scale bar: 4 μm) with a thickness of 13.7 $\pm$ 7.8 nm. There are small protrusions wherever a particle is located. (d) Surface after second (final) PS coating with a thickness of 28.1 $\pm$ 4.1 nm. The final thickness of the top PS layer (h) is 41.8 $\pm$ 9.3 nm (scale bar: 4 μm). The sample exhibits a smooth surface with no topographical features related to buried particles.
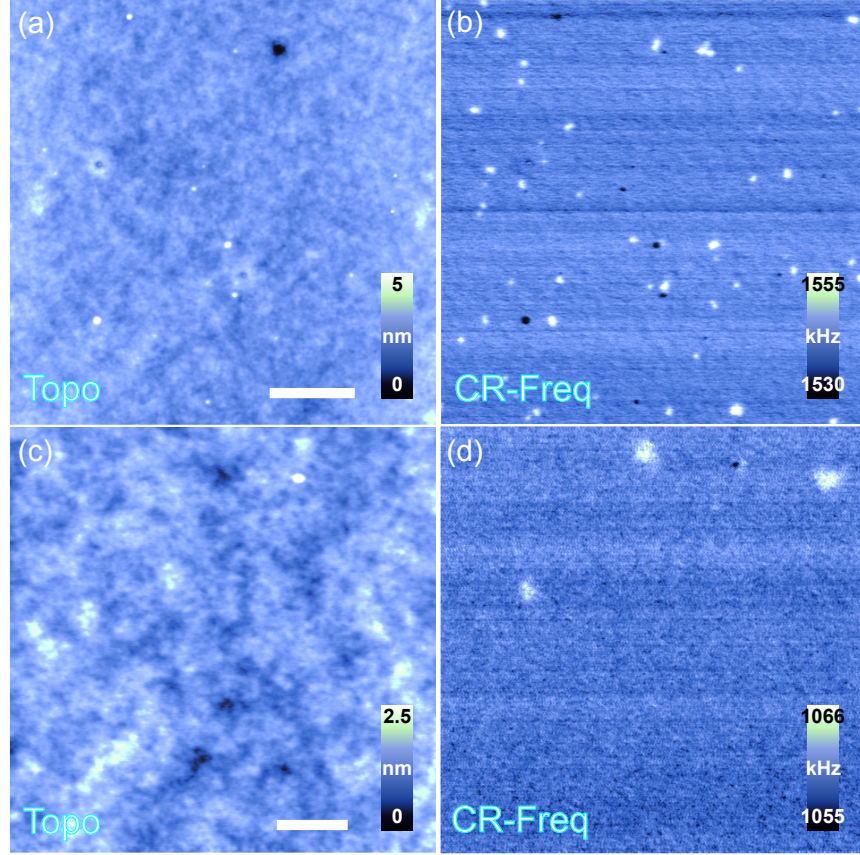
Figure 5.9. Contact-resonance subsurface imaging on model sample. Main observables are (a) topography and (b) CR-Freq (scale bar 2 μm, F = 40 nN, f_3^0 = 1.5 MHz, k_c = 3.7 nN/nm). (c-d) Smaller scanned region for data set acquisition (scale bar 500 nm, F = 70 nN, f_3^0 = 1.01 MHz, k_c = 1.4 nN/nm).

Table 5.1. Main physical variables in CR-AFM, range of input variables for LHS and dimensions.

Variable	Symbol	Range	Dimension
Contact stiffness	k*	–	N·m^{-1}
Effective Young's modulus	E*	–	N·m^{-2}
Tip radius	r_t	10-100 nm	m
Particle radius	r_p	10-80 nm	m
Depth	d	10-100 nm	m
Force	F	20-100 nN	N
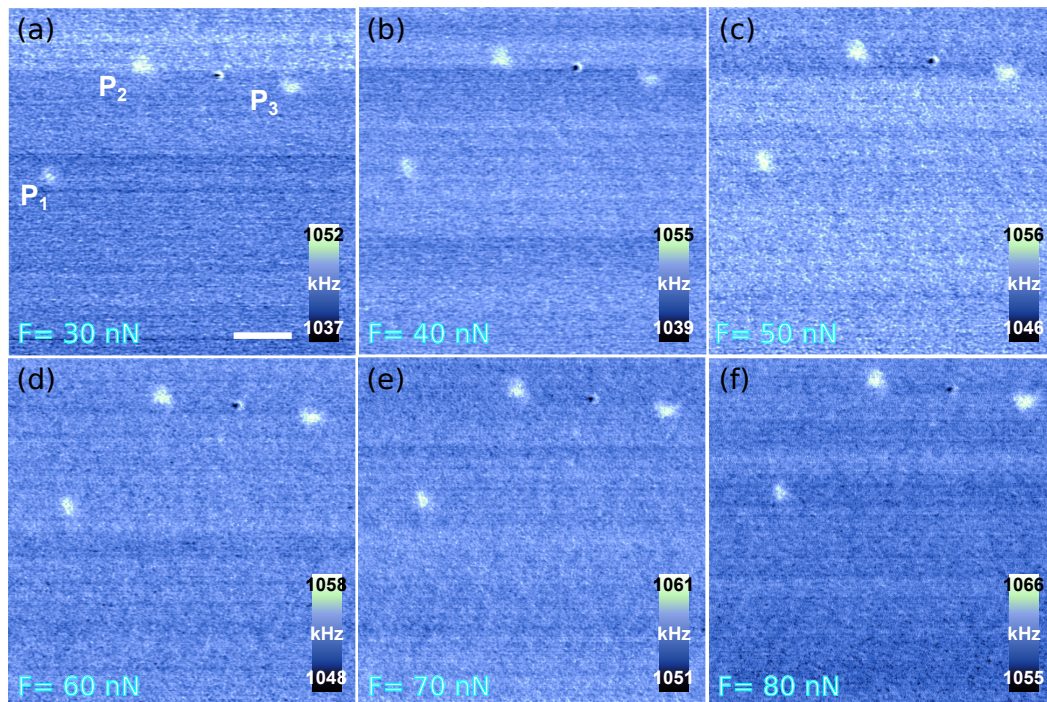
Figure 5.10. Subsurface data set: CR-Freq maps at different applied force, (a-f) F = 20 to 70 nN with steps of 10 nN in between. (Scale bar: 500 nm, $f_3^0 = 1.01$ MHz, $k_c = 1.4$ nN/nm.
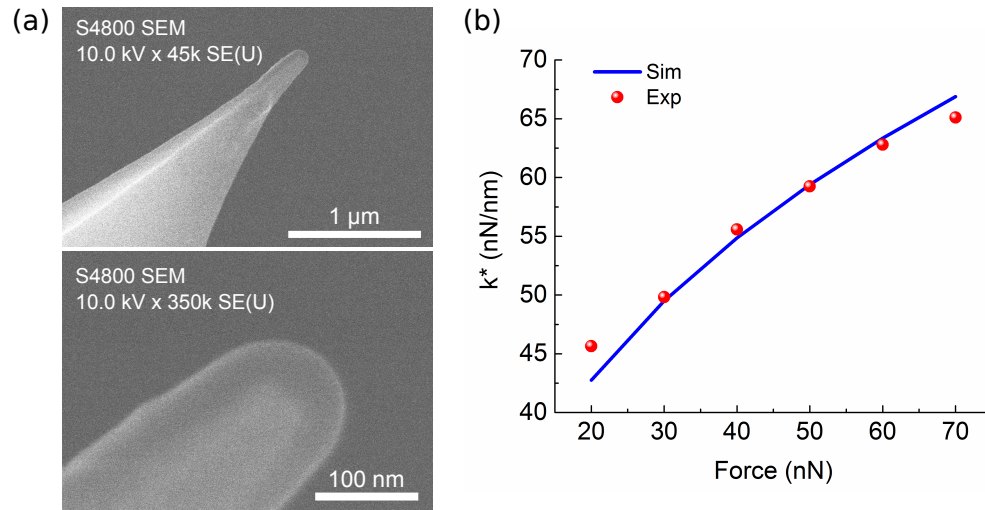
Figure 5.11. (a) SEM (Hitachi S-4800) images of the tip from the FORTA probe (AppNano) used to collect the experimental subsurface data set in the model sample. The estimated value of $r_t = 70$nm. (a) k^* of PS with respect to force, the scatter points corresponds to experimental data, the solid line is the result from a simulation with $r_t = 70$ nm.
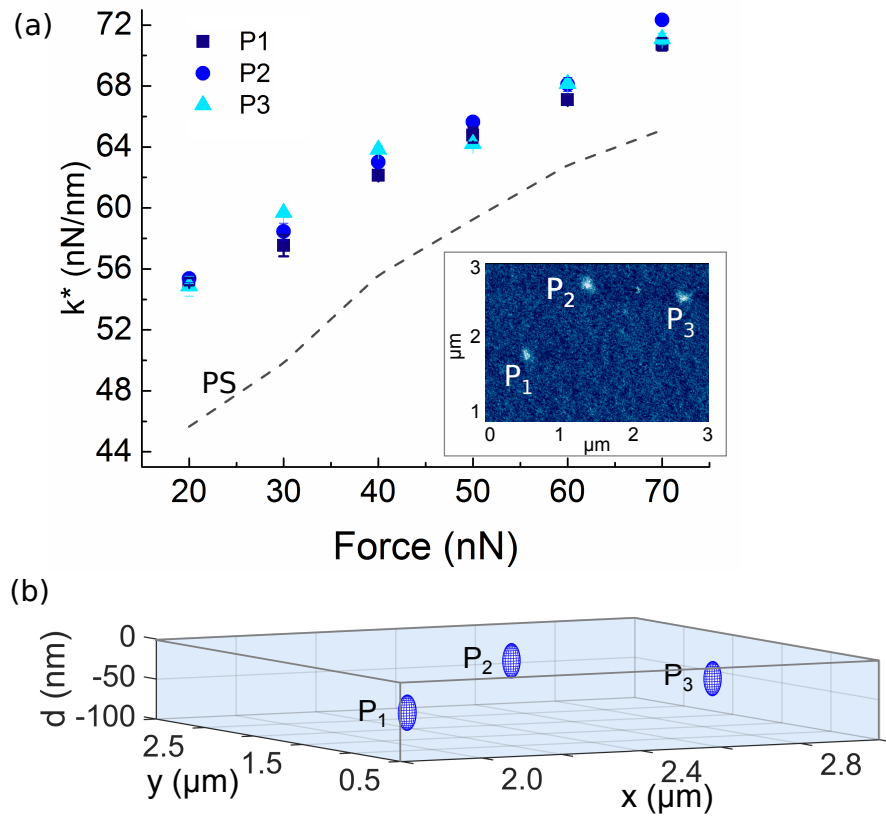
Figure 5.12. Experimental results using CR-AFM on model sample. (a) k^* as a function of force. The scatter points correspond to the mean value of k^* on the particles. The error bars corresponds to the standard deviation. (b) 3D representation of subsurface nanoparticles. Due to the difference in the order of magnitude between the lateral axes (x and y) and z, the spheres appear with an elongated shape.

Table 5.2. Estimates of the b_i parameters for the polynomial function given in Equation (5.2) using least squares ($R^2 = 0.999$).

Parameters	Estimate	SE	p-Value
b_0	0.791	0.096	1.03E-14
b_1	0.591	0.019	8.28E-85
b_2	0.134	0.018	4.37E-12
b_3	-0.144	0.017	5.40E-16
b_4	0.356	0.029	1.11E-27
b_{12}	0.015	0.002	5.26E-14
b_{13}	-0.025	0.002	2.13E-31
b_{14}	0.015	0.002	1.01E-09
b_{23}	-0.068	0.002	4.64E-105
b_{24}	0.012	0.002	2.94E-07
b_{34}	-0.019	0.002	5.77E-17
b_{11}	-0.030	0.002	2.14E-41
b_{22}	0.010	0.002	8.77E-09
b_{33}	0.063	0.002	6.68E-104
b_{44}	-0.003	0.003	0.429

Table 5.3. Estimates of the c_i parameters for the surrogate model (SM 2) given in Equation (5.2) using least squares ($R^2 = 0.992$).

Parameters	Estimates	Confidence intervals
c_1	73.5	[70.4, 76.6]
c_2	568.3	[494.2, 642.5]
c_3	18.0	[16.7, 19.3]
c_4	-8.5	[-9.3, -7.7]

Table 5.4. Estimated particle depth ($\tilde{d}$) using SM 1 (Equation (5.2)) and SM 2 (Equation (5.13), from simulated cases where k^* is calculated as a function of applied load ($F = 30 - 90$) nN. In this case, $r_t = 50$ nm and $r_p = 40$ nm.

d (nm)	SM 1		SM 2	
(actual)	$\tilde{d}$ (nm)	% Error	$\tilde{d}$ (nm)	% Error
15	14.5	3.5	13.5	10.0
25	24.8	0.8	24.4	2.5
35	35.9	2.6	36.0	2.8
45	46.6	3.7	46.2	2.7
55	57.0	3.6	54.3	1.2

Table 5.5. Example 1: estimated particle radius ($\tilde{r}_p$) and depth ($\tilde{d}$) using SM 1 (equation (5.2)) and SM 2 (equation (5.2)), from simulated cases where k^* is calculated as a function of applied load ($F = 30 - 90$ nN). In this case, the tip radius is assumed to be known ($r_t = 50$ nm).

r_p (nm)	d (nm)	SM1				SM2			
		$\tilde{r}_p$ (nm)	%Error	$\tilde{d}$ (nm)	%Error	$\tilde{r}_p$ (nm)	%Error	$\tilde{d}$ (nm)	%Error
40.0	15.0	42.2	5.4	14.5	0.5	42.5	6.2	14.0	6.8
40.0	25.0	42.6	6.5	25.0	2.8	42.5	6.2	25.2	0.9
40.0	35.0	41.6	3.9	35.6	5.0	42.5	6.3	37.2	6.4
40.0	45.0	41.4	3.6	45.7	5.9	41.7	4.2	47.3	5.1
40.0	55.0	36.0	10.0	52.4	3.4	37.2	7.0	52.2	5.1

Table 5.6. Example 2: estimated particle radius $(\tilde{r}_p)$ and depth $(\tilde{d})$ using SM 1 (equation (5.2)) and SM 2 (equation (5.2)), from simulated cases where k^* is calculated as a function of applied load $(F = 30 - 90$ nN). In this case, the tip radius is assumed to be known $(r_t = 50$ nm).

r_p (nm)	d (nm)	SM1				SM2			
		$\tilde{r}p$ (nm)	%Error	$\tilde{d}$ (nm)	%Error	$\tilde{r}p$ (nm)	%Error	$\tilde{d}$ (nm)	%Error
20	50	21.4	7.2	48.9	2.2	20.3	1.6	48.6	2.8
45	35	41.0	9.0	33.9	3.3	45.5	1.1	34.6	1.2
30	15	28.0	6.6	14.3	4.6	26.0	13.4	13.5	9.7
50	20	59.8	19.6	21.3	6.7	55.0	10.0	19.4	3.0
25	40	26.1	4.3	42.2	5.5	22.8	8.9	41.2	3.0

Table 5.7. Estimation of r_p and d of the BaTiO$_3$ nanoparticles in the model sample.

Particle	SM 1		SM 2	
	$\tilde{r}_p$	$\tilde{d}$	$\tilde{r}_p$	$\tilde{d}$
P_1	22.4	20.1	26.5	24.0
P_2	21.8	18.1	26.4	21.7
P_3	21.7	17.7	25.7	21.2

6. SUMMARY AND FUTURE WORK

6.1 Summary: Contributions of This Thesis

In this thesis we investigated the capability of the AFM for non-destructive high resolution subsurface imaging and develop methods for a quantitative 3D reconstruction. Chapter one presented a review of the state of the start on this matter, classifying the existing dynamic AFM techniques depending on the detection mechanism. Within the available techniques, our work focuses on the detection of electrostatic force interactions and local mechanical properties, using 2nd-harmonic KPFM and CR-AFM, respectively. These are two robust quantitative dynamic AFM techniques where we can relate the experimental observable to a physical variable.

In chapter 2, we exploit resonance-enhanced 2nd-harmonic KPFM as a sensitive high resolution technique for subsurface imaging applications. It provides a better signal-to-noise ratio (SNR) due to the resonance amplification, without resorting to larger voltages. This in turn results in a significant higher contrast resolution (image quality) when compared to the off-resonance case. This mode provides high resolution subsurface images on a variety of polymer composites.

Resonance-enhanced 2nd-harmonic KPFM is suitable for the two common configurations of KPFM, double-pass and single-pass, as shown in chapter 2. We noted that double-pass is advantageous when operating under ambient conditions. It works in a monomodal configuration where the first eigenmode frequency of the microcantilever is optimal for both mechanical and electrostatic force detection. The quantitative interpretation of the experimental observables is performed by modeling the microcantilever dynamics as a single-degree of freedom oscillator.

CR-AFM is by itself a resonance detection technique. A direct comparison with resonance-enhanced 2nd-harmonic KPFM is presented in chapter 3. This study dis-

cerns the advantages and disadvantages of each technique. We highlighted the higher lateral resolution in CR-AFM based upon the highly localized stress field. Meanwhile, the lateral resolution in KPFM decreases due to the broadening effect of the electric field lines. This was an influential consideration to develop the reconstruction approach in Chapter 5. Furthermore, this study opens up the possibility of using a combination of multiple excitation fields for subsurface imaging applications.

CR-AFM and KPFM both enable high sensitivity subsurface imaging. Although the physics behind them is different, similar computational approaches can be used for reconstruction purposes. An example is presented in chapter 3, where we estimate the depth of the same subsurface features imaged with both techniques, finding a satisfactory agreement between the two. The depth in this case is directly estimated from master curves obtained by finite element models that assume knowledge of all the other tip-sample parameters. Finite element analysis is an indispensable tool used through out this thesis. It provides i) a deeper understanding of the physical principles behind the techniques and their limitations, ii) a quantitative comparison between theoretical expectations and experiments and iii) a quantification of sample properties.

The relation of the experimental observables to a physical variable in both techniques opens up a procedure for 3D reconstruction. The goal is to recreate the spatial distribution and shape of the subsurface features within the volume of the sample. An ad-hoc reconstruction approach is proposed in chapter 4 based on surrogate modeling. This describes the functional relationship between the electrostatic force and the main independent parameters as a polynomial function. The mathematical expression can then be used to estimate the size and depth of the subsurface object, which is demonstrated in the case of 0D objects embedded within a low dielectric matrix. This model assumes that there is only one object in the close vicinity of interaction with the tip.

Finally, the reconstruction approach based on surrogate models is extended to CR-AFM in chapter 5. As described in chapter 3, CR-AFM has the advantage of a more

localized interaction between the tip and the subsurface object. Aside from an empirical polynomial function, we proposed a model based on dimensional analysis which relies more on physical intuition and provides a reduced expression. Both approaches show to be useful from the validation made with simulations and experimental data acquired on a model sample.

6.2 Future Research Directions

This thesis discussed the use of AFM techniques for high-resolution non-destructive subsurface imaging and a method to reconstruct nanoscale subsurface features from the AFM data. There is still work to be done and remaining challenges to be addressed. Here are some suggestions on future directions in this area.

6.2.1 Application to Other Nanoscale Materials and Devices

Throughout this work we use a variety of polymer nanocomposites that incorporate 0D-nanoparticles, 1D-nanotubes, or 2D-platelets dispersed in a polymer matrix. However, the AFM techniques in combination with reconstruction approaches can be used to characterize other types of materials and devices, currently under development. For instance, 3D structures and multilayer materials, where there is still a demand for innovative non-destructive 3D metrology tools [194, 195].

In this context, the International Roadmap for Devices and Systems (2017) projects reduced device feature sizes less than 5 nm within the next 10 years and an increasing use of complex 3D structures fabricated using new materials and processes. The IRDS emphasizes the need for new tools capable of the detection of defects and analysis of interconnects covered by overlays. This is relevant during process control and failure analysis of devices that incorporate nanometer size features [196]. Based on the work performed in this thesis, both KPFM and CR-AFM should be tested on these complex 3D structures of interest to the device community.

6.2.2 Complex Shapes and Generalization of Surrogate Model

Our aim in chapter 4 and 5 is to demonstrate a methodology for reconstruction of subsurface properties from AFM data using surrogate models. This is done in the case of buried 0D objects in a uniform matrix. The proposed approach can be expanded to more complex shapes such as 1D or 2D objects, which are geometrically described by more than 1 parameter. This expansion requires the identification and inclusion of other input parameters, which in turn implies multiparametric models and large scale computations. It would also require the exploration of other independent observables to create numerically independent models.

The critical task is the creation of global surrogate models for complete blind reconstruction. This would be of benefit for the application to a larger range of samples. We suggest the exploration of supervised learning algorithms such as artificial neural networks or genetic algorithms [197].

6.2.3 Combination of Detection Mechanisms

The comparison between the subsurface imaging capabilities of CR-AFM and KPFM presented in chapter 3 offers an insight in how a combination of different excitation fields can yield complementary results. For example, depending on the sample properties, either one technique or both can be used. CR-AFM is appropriate in the case where there are weak electrostatic force interactions between the tip and the sample or when dielectric properties of the inclusions and the matrix are so similar they can not be discriminated. On the contrary, KPFM is useful for soft or sticky samples or when the sample components exhibit similar elastic properties. However, both can be combined when there is interest to extract either dielectric or mechanical properties or when challenging samples are studied. Furthermore, other detection mechanisms can be explored using magnetic fields or thermal spectroscopy [24, 198].

6.2.4 Improved Subsurface Data Acquisition

The AFM is able to generate a 2D image while the tip scans above the sample moving along the x and y directions. The location of the tip and the sample are fixed in terms of orientation, which becomes a limitation to generate 3D volume reconstruction. As a solution in chapters 4 and 5 we propose to acquire a set of 2D maps where the observable is measured at different values of a controllable predictor variable. Therefore we scan the same region of interest several times while increasing the nap height or the applied force in the case of 2nd-harmonic KPFM or CR-AFM, respectively.

A significant improvement to this approach would be the acquisition of a data set using just one single scan. A possibility is to use a similar approach as the recently implemented multidimensional mapping mode by Bruker [199]. In this mode, force spectra are acquired at each pixel of the image as in fast force mapping [200], but additionally it allows to hold the tip at a defined setpoint force, and vary other operating parameter. In the case of 2nd-harmonic KPFM, this would allow to ramp the voltage while the tip is engaged with the sample to measure electrostatic force spectra. In the case of CR-AFM, CR-Freq spectra could be measured with respect to the applied force. This generates data cubes for each pixel of the image at one single scan with the needed information.

Such an approach will contribute to i) faster experimental data acquisition, ii) the reduction of lateral force, which in turn reduces tip wear or modification of the surface of the sample in CR-AFM and iii) avoid the drifts that appear in consecutive scans.

REFERENCES

REFERENCES

[1] D. R. Paul and L. M. Robeson. Polymer nanotechnology: nanocomposites. *Polymer*, 49(15):3187–3204, 7 2008.

[2] L. Yu, C. Shearer, and J. Shapter. Recent development of carbon nanotube transparent conductive films. *Chemical Reviews*, 116(22):13413–13453, 11 2016.

[3] B. Dan, G. C. Irvin, and M. Pasquali. Continuous and scalable fabrication of transparent conducting carbon nanotube films. *ACS Nano*, 3(4):835–843, 4 2009.

[4] T. Kobayashi, M. Bando, N. Kimura, K. Shimizu, K. Kadono, N. Umezu, K. Miyahara, S. Hayazaki, S. Nagai, Y. Mizuguchi, Y. Murakami, and D. Hobara. Production of a 100-m-long high-quality graphene transparent conductive film by roll-to-roll chemical vapor deposition and transfer process. *Applied Physics Letters*, 102(2):023112, 1 2013.

[5] L. Hu, H. S. Kim, J.-Y. Lee, P. Peumans, and Y. Cui. Scalable coating and properties of transparent, flexible, silver nanowire electrodes. *ACS Nano*, 4(5):2955–2963, 5 2010.

[6] C. F. Guo and Z. Ren. Flexible transparent conductors based on metal nanowire networks. *Materials Today*, 18(3):143–154, 4 2015.

[7] V. L. Pushparaj, S. Sreekala, O. Nalamasu, and P. M. Ajayan. Flexible energy storage devices using nanomaterials. In *Semiconductor nanomaterials for flexible technologies*, pages 227–245. Elsevier Ltd., first edit edition, 2010.

[8] X. Li, F. Gittleson, M. Carmo, R. C. Sekol, and A. D. Taylor. Scalable fabrication of multifunctional freestanding carbon nanotube/polymer composite thin films for energy conversion. *ACS Nano*, 6(2):1347–1356, 2 2012.

[9] R. V. Salvatierra, C. E. Cava, L. S. Roman, and A. J. G. Zarbin. ITO-free and flexible organic photovoltaic device based on high transparent and conductive polyaniline/carbon nanotube thin films. *Advanced Functional Materials*, 23(12):1490–1499, 2013.

[10] M. V. Kiamahalleh, S. H. S. Zein, G. Najafpour, S. A. Sata, and S. Buniran. Multiwalled carbon nanotubes based nanocomposites for supercapacitors: a review of electrode materials. *Nano*, 07(02):1230002, 4 2012.

[11] D.-m. Sun, M. Y. Timmermans, Y. Tian, A. G. Nasibulin, E. I. Kauppinen, S. Kishimoto, T. Mizutani, and Y. Ohno. Flexible high-performance carbon nanotube integrated circuits. *Nature Nanotechnology*, 6(3):156–161, 2011.

[12] A. Hirohata, Y. Yamamoto, B. A. Murphy, and A. J. Vick. Non-destructive imaging of buried electronic interfaces using a decelerated scanning electron beam. *Nature Communications*, 7:12701, 2016.

[13] International Roadmap Committee. International technology roadmap for semiconductors 2.0. Technical report, ITRS, 2015.

[14] H. Stahlberg and T. Walz. Molecular electron microscopy: state of the art and current challenges. *ACS Chemical Biology*, 3(5):268–281, 5 2008.

[15] S. Kirk, J. Skepper, and A. Donald. Application of environmental scanning electron microscopy to determine biological surface structure. *Journal of Microscopy*, 233(2):205–224, 2 2009.

[16] J. Pierson, M. Sani, C. Tomova, S. Godsave, and P. J. Peters. Toward visualization of nanomachines in their native cellular environment. *Histochemistry and Cell Biology*, 132(3):253–262, 9 2009.

[17] L. Tetard, A. Passian, K. T. Venmar, R. M. Lynch, B. H. Voy, G. Shekhawat, V. P. Dravid, and T. Thundat. Imaging nanoparticles in cells by nanomechanical holography. *Nature nanotechnology*, 3(8):501–5, 8 2008.

[18] G. Möbus and B. J. Inkson. Nanoscale tomography in materials science. *Materials Today*, 10(12):18–25, 2007.

[19] E. Fogelqvist, M. Kördel, V. Carannante, B. Önfelt, and H. M. Hertz. Laboratory cryo x-ray microscopy for 3D cell imaging. *Scientific Reports*, 7(1):13433, 12 2017.

[20] K. Thompson, J. H. Bunton, J. S. Moore, and K. S. Jones. Compositional analysis of Si nanostructures: SIMS3D tomographic atom probe comparison. *Semiconductor Science and Technology*, 22(1):S127–S131, 1 2007.

[21] G. Möbus, R. C. Doole, and B. J. Inkson. Spectroscopic electron tomography. *Ultramicroscopy*, 96(3):433–451, 2003.

[22] A. Zankel, J. Wagner, and P. Poelt. Serial sectioning methods for 3D investigations in materials science. *Micron*, 62:66–78, 7 2014.

[23] T. F. Kelly and M. K. Miller. Atom probe tomography. *Review of Scientific Instruments*, 78(3):031101, 3 2007.

[24] A. Alekseev, A. Efimov, J. Loos, N. Matsko, and J. Syurik. Three-dimensional imaging of polymer materials by scanning probe tomography. *European Polymer Journal*, 52:154–165, 3 2014.

[25] D. B. Williams and C. B. Carter. The transmission electron microscope. In *Transmission electron microscopy: a textbook for materials science*, chapter 1, pages 3–17. Springer US, Boston, MA, 2009.

[26] T. L. Hayes. Biophysical aspects of scanning electron microscopy. *Scanning electron microscopy*, 1:1–10, 1980.

[27] L. Reimer. Introduction. In *Scanning Electron Microscopy: physics of image formation and microanalysis*, chapter 1, pages 1–12. Springer Berlin Heidelberg, 1998.

[28] A. B. Morgan and J. W. Gilman. Characterization of polymer-layered silicate (clay) nanocomposites by transmission electron microscopy and X-ray diffraction: A comparative study. *Journal of Applied Polymer Science*, 87(8):1329–1338, 2 2003.

[29] I. Kvien, B. S. Tanem, and K. Oksman. Characterization of cellulose whiskers and their nanocomposites by atomic force and electron microscopy. *Biomacromolecules*, 6(6):3160–3165, 2005.

[30] X. Kornmann. Synthesis of epoxyclay nanocomposites. Influence of the nature of the curing agent on structure. *Polymer*, 42(10):4493–4499, 2 2001.

[31] S. Wang. Preparation and characterization of flame retardant ABS/montmorillonite nanocomposite. *Applied Clay Science*, 25(1-2):49–55, 4 2004.

[32] S. Stankovich, D. A. Dikin, G. H. B. Dommett, K. M. Kohlhaas, E. J. Zimney, E. A. Stach, R. D. Piner, S. T. Nguyen, and R. S. Ruoff. Graphene-based composite materials. *Nature*, 442(7100):282–6, 7 2006.

[33] L. Holzer, F. Indutnyi, P. Gasser, B. Munch, and M. Wegmann. Three-dimensional analysis of porous BaTiO3 ceramics using FIB nanotomography. *Journal of Microscopy*, 216(1):84–95, 10 2004.

[34] M. Schaffer, J. Wagner, B. Schaffer, M. Schmied, and H. Mulders. Automated three-dimensional X-ray analysis using a dual-beam FIB. *Ultramicroscopy*, 107(8):587–597, 8 2007.

[35] K. L. Briggman and D. D. Bock. Volume electron microscopy for neuronal circuit reconstruction. *Current Opinion in Neurobiology*, 22(1):154–161, 2 2012.

[36] M. A. Mangan, P. D. Lauren, and G. J. Shiflet. Three-dimensional reconstruction of Widmanstatten plates in Fe-12.3Mn-0.8C. *Journal of Microscopy*, 188(1):36–41, 10 1997.

[37] G. Spanos, D. Rowenhorst, A. Lewis, and A. Geltmacher. Combining serial sectioning, EBSD analysis, and image-based finite element modeling. *MRS Bulletin*, 33(06):597–602, 2008.

[38] A. Zankel, B. Kraus, P. Poelt, M. Schaffer, and E. Ingolic. Ultramicrotomy in the ESEM, a versatile method for materials and life sciences. *Journal of Microscopy*, 233(1):140–148, 1 2009.

[39] M. Vázquez, D. Moore, X. He, B. A. Aymen, E. Nesterenko, P. Nesterenko, B. Paull, and D. Brabazon. Focussed ion beam serial sectioning and imaging of monolithic materials for 3D reconstruction and morphological parameter evaluation. *Analyst*, 139(1):99–104, 2014.

[40] P. T. Lillehei, J.-W. Kim, L. J. Gibbons, and C. Park. A quantitative assessment of carbon nanotube dispersion in polymer matrices. *Nanotechnology*, 20(32):325708, 8 2009.

[41] W. Li, S. T. Buschhorn, K. Schulte, and W. Bauhofer. The imaging mechanism, imaging depth, and parameters influencing the visibility of carbon nanotubes in a polymer matrix using an SEM. *Carbon*, 49(6):1955–1964, 2011.

[42] M. Zhao, B. Ming, J.-W. Kim, L. J. Gibbons, X. Gu, T. Nguyen, C. Park, P. T. Lillehei, J. S. Villarrubia, A. E. Vladár, and J. A. Liddle. New insights into subsurface imaging of carbon nanotubes in polymer composites via scanning electron microscopy. *Nanotechnology*, 26(8):085703, 2 2015.

[43] C. R. Misiego and R. B. Pipes. Dispersion and its relation to carbon nanotube concentration in polyimide nanocomposites. *Composites Science and Technology*, 85:43–49, 8 2013.

[44] E. Tkalya, M. Ghislandi, A. Alekseev, C. Koning, and J. Loos. Latex-based concept for the preparation of graphene-based polymer nanocomposites. *Journal of Materials Chemistry*, 20(15):3035, 2010.

[45] M. Nagase, A. Fujiwara, K. Kurihara, and H. Namatsu. Nanometrology of Si nanostructures embedded in SiO2 using scanning electron microscopy. *Japanese Journal of Applied Physics*, 42(Part 1, No. 1):318–325, 1 2003.

[46] T. Koike, T. Ikeda, H. Abe, and F. Komatsu. Investigation of scanning electron microscope overlay metrology. *Japanese Journal of Applied Physics*, 38(Part 1, No. 12B):7159–7163, 12 1999.

[47] H.-B. Zhang, R.-J. Feng, and K. Ura. Utilizing the charging effect in scanning electron microscopy. *Science Progress*, 87(4):249–268, 11 2004.

[48] P. A. Midgley and R. E. Dunin-Borkowski. Electron tomography and holography in materials science. *Nature Materials*, 8(4):271–280, 4 2009.

[49] F. Dalmas, N. Genevaz, M. Roth, J. Jestin, and E. Leroy. 3D dispersion of spherical silica nanoparticles in polymer nanocomposites: a quantitative study by electron tomography. *Macromolecules*, 47(6):2044–2051, 3 2014.

[50] N. Kawase, M. Kato, H. Nishioka, and H. Jinnai. Transmission electron microtomography without the missing wedge for quantitative structural analysis. *Ultramicroscopy*, 107(1):8–15, 1 2007.

[51] R. Egerton, P. Li, and M. Malac. Radiation damage in the TEM and SEM. *Micron*, 35(6):399–409, 2004.

[52] A. E. Weston, H. E. J. Armer, and L. M. Collinson. Towards native-state imaging in biological context in the electron microscope. *Journal of Chemical Biology*, 3(3):101–112, 8 2010.

[53] V. Migunov, H. Ryll, X. Zhuge, M. Simson, L. Strüder, K. J. Batenburg, L. Houben, and R. E. Dunin-Borkowski. Rapid low dose electron tomography using a direct electron detection camera. *Scientific Reports*, 5:14516, 10 2015.

[54] N. de Jonge and F. M. Ross. Electron microscopy of specimens in liquid. *Nature Nanotechnology*, 6(11):695–704, 10 2011.

[55] P. K. Hansma, V. B. Elings, O. Marti, and C. E. Bracker. Scanning tunneling microscopy and atomic force microscopy: application to biology and technology. *Science*, 242(4876), 1988.

[56] G. Binnig, C. F. Quate, and C. Gerber. Atomic force microscope. *Physical Review Letters*, 56(9):930–933, 3 1986.

[57] T. R. Albrecht and C. F. Quate. Atomic resolution imaging of a nonconductor by atomic force microscopy. *Journal of Applied Physics*, 62(7):2599–2602, 10 1987.

[58] F. J. Giessibl. Atomic resolution of the silicon (111)-(7x7) surface by atomic force microscopy. *Science*, 267(5194):68–71, 1 1995.

[59] A. Raman, S. Trigueros, A. Cartagena, A. P. Z. Stevenson, M. Susilo, E. Nauman, and S. A. Contera. Mapping nanomechanical properties of live cells using multi-harmonic atomic force microscopy. *Nature Nanotechnology*, 6(12):809–814, 11 2011.

[60] R. Wagner, R. Moon, J. Pratt, G. Shaw, and A. Raman. Uncertainty quantification in nanomechanical measurements using the atomic force microscope. *Nanotechnology*, 22(45):455703, 11 2011.

[61] R. Garcia and R. Proksch. Nanomechanical mapping of soft matter by bimodal force microscopy. *European Polymer Journal*, 49(8):1897–1906, 2013.

[62] L. Fumagalli, D. Esteban-Ferrer, A. Cuervo, J. L. Carrascosa, and G. Gomila. Label-free identification of single dielectric nanoparticles and viruses with ultraweak polarization forces. *Nature materials*, 11(9):808–16, 9 2012.

[63] L. Fumagalli, G. Gramse, D. Esteban-Ferrer, M. A. Edwards, and G. Gomila. Quantifying the dielectric constant of thick insulators using electrostatic force microscopy. *Applied Physics Letters*, 96(18):183107, 5 2010.

[64] M. M. Kummali, L. A. Miccio, G. A. Schwartz, A. Alegría, J. Colmenero, J. Otegui, A. Petzold, and S. Westermann. Local mechanical and dielectric behavior of the interacting polymer layer in silica nano-particles filled SBR by means of AFM-based methods. *Polymer*, 54(18):4980–4986, 8 2013.

[65] M. J. Cadena, S. H. Sung, B. W. Boudouris, R. Reifenberger, and A. Raman. Nanoscale mapping of dielectric properties of nanomaterials from kilohertz to megahertz using ultrasmall cantilevers. *ACS Nano*, 10(4):4062–4071, 4 2016.

[66] Y. Sugimoto, P. Pou, M. Abe, P. Jelinek, R. Pérez, S. Morita, and O. Custance. Chemical identification of individual surface atoms by atomic force microscopy. *Nature*, 446(7131):64–67, 3 2007.

[67] S. Jesse, A. Kumar, T. M. Arruda, Y. Kim, S. V. Kalinin, and F. Ciucci. Electrochemical strain microscopy: Probing ionic and electrochemical phenomena in solids at the nanometer level. *MRS Bulletin*, 37(07):651–658, 7 2012.

[68] A. Kumar, F. Ciucci, A. N. Morozovska, S. V. Kalinin, and S. Jesse. Measuring oxygen reduction/evolution reactions on the nanoscale. *Nature chemistry*, 3(9):707–13, 9 2011.

[69] C. A. J. Putman, K. O. Van der Werf, B. G. De Grooth, N. F. Van Hulst, and J. Greve. Tapping mode atomic force microscopy in liquid. *Applied Physics Letters*, 64(18):2454–2456, 5 1994.

[70] S. Basak and A. Raman. Dynamics of tapping mode atomic force microscopy in liquids: Theory and experiments. *Applied Physics Letters*, 91(6):064107, 8 2007.

[71] F. J. Giessibl. Advances in atomic force microscopy. *Reviews of Modern Physics*, 75(3):949–983, 7 2003.

[72] W. Hebenstreit, J. Redinger, Z. Horozova, M. Schmid, R. Podloucky, and P. Varga. Atomic resolution by STM on ultra-thin films of alkali halides: experiment and local density calculations. *Surface Science*, 424(2-3):L321–L328, 4 1999.

[73] E. Stolyarova, K. T. Rim, S. Ryu, J. Maultzsch, P. Kim, L. E. Brus, T. F. Heinz, M. S. Hybertsen, and G. W. Flynn. High-resolution scanning tunneling microscopy imaging of mesoscopic graphene sheets on an insulating surface. *Proceedings of the National Academy of Sciences of the United States of America*, 104(22):9209–12, 5 2007.

[74] G. Binning, H. Rohrer, C. Gerber, and E. Weibel. Surface studies by scanning tunneling microscopy. *Physics Review Letters*, 49(1):57–61, 1982.

[75] R. Reifenberger. *Fundamentals of atomic force microscopy. Part I: foundations.* World Scientific, 11 2015.

[76] S. N. Magonov and D. H. Reneker. Characterization of polymer surfaces with atomic force microscopy. *Annu. Rev. Mat. Sci.*, 27:175–222, 1997.

[77] T. Kajiyama, K. Tanaka, S.-R. Ge, and A. Takahara. Morphology and mechanical properties of polymer surfaces via scanning force microscopy. *Progress in Surface Science*, 52(1):1–52, 1996.

[78] T. R. Albrecht, P. Grutter, D. Horne, and D. Rugar. Frequency modulation detection using high-Q cantilevers for enhanced force microscope sensitivity. *Journal of Applied Physics*, 69(2):668, 1 1991.

[79] R. Magerle. Nanotomography. *Physical Review Letters*, 85(13):2749–2752, 9 2000.

[80] A. Schulze, T. Hantschel, A. Dathe, P. Eyben, X. Ke, and W. Vandervorst. Electrical tomography using atomic force microscopy and its application towards carbon nanotube-based interconnects. *Nanotechnology*, 23(30):305707, 8 2012.

[81] O. Kolosov and K. Yamanaka. Nonlinear detection of ultrasonic vibrations in an atomic force microscope. *Japanese Journal of Applied Physics*, 32(Part 2, No. 8A):L1095–L1098, 8 1993.

[82] K. Yamanaka and S. Nakano. Ultrasonic atomic force microscope with overtone excitation of cantilever. *Japanese Journal of Applied Physics*, 35(Part 1, No. 6B):3787–3792, 6 1996.

[83] T. Tsuji and K. Yamanaka. Observation by ultrasonic atomic force microscopy of reversible displacement of subsurface dislocations in highly oriented pyrolytic graphite. *Nanotechnology*, 12(3):301–307, 9 2001.

[84] M. T. Cuberes, H. E. Assender, G. A. D. Briggs, and O. V. Kolosov. Heterodyne force microscopy of PMMA/rubber nanocomposites: nanomapping of viscoelastic response at ultrasonic frequencies. *Journal of Physics D: Applied Physics*, 33(19):2347–2355, 10 2000.

[85] G. S. Shekhawat and V. P. Dravid. Nanoscale imaging of buried structures via scanning near-field ultrasound holography. *Science (New York, N.Y.)*, 310(5745):89–92, 10 2005.

[86] L. Tetard, A. Passian, R. M. Lynch, B. H. Voy, G. Shekhawat, V. Dravid, and T. Thundat. Elastic phase response of silica nanoparticles buried in soft matter. *Applied Physics Letters*, 93(13):133113, 2008.

[87] G. Shekhawat, A. Srivastava, S. Avasthy, and V. Dravid. Ultrasound holography for noninvasive imaging of buried defects and interfaces for advanced interconnect architectures. *Applied Physics Letters*, 95(26):263101, 2009.

[88] S. A. Cantrell, J. H. Cantrell, and P. T. Lillehei. Nanoscale subsurface imaging via resonant difference-frequency atomic force ultrasonic microscopy. *Journal of Applied Physics*, 101(11):114324, 2007.

[89] G. J. Verbiest, J. N. Simon, T. H. Oosterkamp, and M. J. Rost. Subsurface atomic force microscopy: towards a quantitative understanding. *Nanotechnology*, 23(14):145704, 4 2012.

[90] L. Tetard, A. Passian, and T. Thundat. New modes for subsurface atomic force microscopy through nanomechanical coupling. *Nature Nanotechnology*, 5(2):105–109, 2 2010.

[91] R. Garcia. Probe microscopy: images from below the surface. *Nature nanotechnology*, 5(2):101–2, 2 2010.

[92] E. C. Spitzner, C. Riesch, and R. Magerle. Subsurface imaging of soft polymeric materials with nanoscale resolution. *ACS Nano*, 5(1):315–320, 1 2011.

[93] A. Knoll, R. Magerle, and G. Krausch. Tapping Mode Atomic Force Microscopy on Polymers: Where Is the True Sample Surface? *Macromolecules*, 34:4159–4165, 2001.

[94] J. Lozano and R. Garcia. Theory of Multifrequency Atomic Force Microscopy. *Physical Review Letters*, 100(7):076102, 2 2008.

[95] A. P. Perrino, Y. K. Ryu, C. A. Amo, M. P. Morales, and R. Garcia. Subsurface imaging of silicon nanowire circuits and iron oxide nanoparticles with sub-10 nm spatial resolution. *Nanotechnology*, 27(27):275703, 7 2016.

[96] J. P. Killgore, J. Y. Kelly, C. M. Stafford, M. J. Fasolka, and D. C. Hurley. Quantitative subsurface contact resonance force microscopy of model polymer nanocomposites. *Nanotechnology*, 22(17):175706, 4 2011.

[97] K. Kimura, K. Kobayashi, K. Matsushige, and H. Yamada. Imaging of Au nanoparticles deeply buried in polymer matrix by various atomic force microscopy techniques. *Ultramicroscopy*, 133:41–49, 2013.

[98] Z. Parlak and F. L. Degertekin. Contact stiffness of finite size subsurface defects for atomic force microscopy: Three-dimensional finite element modeling and experimental verification. *Journal of Applied Physics*, 103(11):114910, 2008.

[99] D. C. Hurley, M. Kopycinska-Müller, E. D. Langlois, A. B. Kos, and N. Barbosa. Mapping substrate/film adhesion with contact-resonance-frequency atomic force microscopy. *Applied Physics Letters*, 89(2):021911, 2006.

[100] J. P. Killgore, D. G. Yablon, A. H. Tsou, A. Gannepalli, P. A. Yuya, J. A. Turner, R. Proksch, and D. C. Hurley. Viscoelastic property mapping with contact resonance force microscopy. *Langmuir : the ACS journal of surfaces and colloids*, 27(23):13983–7, 12 2011.

[101] H. T. Thompson, F. Barroso-Bujans, J. G. Herrero, R. Reifenberger, and A. Raman. Subsurface imaging of carbon nanotube networks in polymers with DC-biased multifrequency dynamic atomic force microscopy. *Nanotechnology*, 24(13):135701, 4 2013.

[102] M. J. Cadena, R. Misiego, K. C. Smith, A. Avila, B. Pipes, R. Reifenberger, and A. Raman. Sub-surface imaging of carbon nanotube polymer composites using dynamic AFM methods. *Nanotechnology*, 24(13):135706, 4 2013.

[103] S. Magonov and J. Alexander. Advanced atomic force microscopy: exploring measurements of local electric properties. Technical report, Agilent Technologies, 2008.

[104] S. Sadewasser. Experimental technique and working modes. In *Kelvin probe force microscopy*, chapter 1, pages 7–24. Springer Berlin Heidelberg, 2012.

[105] S. Magonov, J. Alexander, and S. Wu. Advancing characterization of materials with atomic force microscopy based electric techniques. In S. V. Kalinin and A. Gruverman, editors, *Scanning probe microscopy of functional materials*, pages 233–300. Springer New York, New York, NY, 2011.

[106] T. S. Jespersen and J. Nygård. Charge trapping in carbon nanotube loops demonstrated by electrostatic force microscopy. *Nano letters*, 5(9):1838–41, 9 2005.

[107] M. Nonnenmacher, M. P. O' Boyle, and H. K. Wickramasinghe. Kelvin probe force microscopy. *Applied Physics Letters*, 58(25):2921, 1991.

[108] J. Lü, E. Delamarche, L. Eng, R. Bennewitz, E. Meyer, and H. Güntherodt. Kelvin probe force microscopy on surfaces: investigation of the surface potential of self-assembled monolayers on gold. *Langmuir*, 15:8184–8188, 1999.

[109] O. A. Castañeda-Uribe, R. Reifenberger, A. Raman, and A. Avila. Depth-sensitive subsurface imaging of polymer nanocomposites using second harmonic Kelvin probe force microscopy. *ACS Nano*, 9(3):2938–2947, 3 2015.

[110] M. Fujihira. Kelvin probe force microscopy of molecular surfaces. *Annual Review of Materials Science*, 29(1):353–380, 8 1999.

[111] S. Magonov and J. Alexander. Single-pass Kelvin force microscopy and dC/dZ measurements in the intermittent contact: applications to polymer materials. *Beilstein journal of nanotechnology*, 2:15–27, 1 2011.

[112] H. Takano, S.-S. Wong, J. A. Harnisch, and M. D. Porter. Mapping the subsurface composition of organic films by electric force microscopy. *Langmuir*, 16:5231–5233, 2000.

[113] M. Zhao, X. Gu, S. E. Lowther, C. Park, Y. C. Jean, and T. Nguyen. Subsurface characterization of carbon nanotubes in polymer composites via quantitative electric force microscopy. *Nanotechnology*, 21(22):225702, 6 2010.

[114] S. Patel, C. W. Petty, K. Krafcik, B. Loyola, G. OBryan, and R. W. Friddle. Imaging latex carbon nanotube composites by subsurface electrostatic force microscopy. *Nanotechnology*, 27(41):415705, 10 2016.

[115] M. Marzec, K. Awsiuk, A. Bernasik, J. Rysz, J. Haberko, W. Łużny, and A. Budkowski. Buried polymer/metal interfaces examined with Kelvin probe gorce microscopy. *Thin Solid Films*, 531:271–276, 2013.

[116] G. S. Shekhawat and V. P. Dravid. Nanoscale imaging of buried structures via scanning near-field ultrasound holography. *Science*, 310(5745):89–92, 10 2005.

[117] A. Alekseev, D. Chen, E. E. Tkalya, M. G. Ghislandi, Y. Syurik, O. Ageev, J. Loos, and G. De With. Local organization of graphene network inside graphene/polymer composites. *Advanced Functional Materials*, 22(6):1311–1318, 3 2012.

[118] A. P. Perrino, Y. K. Ryu, C. A. Amo, M. P. Morales, and R. Garcia. Subsurface imaging of silicon nanowire circuits and iron oxide nanoparticles with sub-10 nm spatial resolution. *Nanotechnology*, 27(27):275703, 7 2016.

[119] T. S. Jespersen and J. Nygard. Mapping of individual carbon nanotubes in polymer/nanotube composites using electrostatic force microscopy. *Applied Physics Letters*, 90(18):183108, 2007.

[120] M. R. Weaver and D. W. Abraham. High resolution atomic force microscopy potentiometry. *J. Vac. Sci. Techno!. B*, 9(3):1559–1561, 1991.

[121] T. Hochwitz, A. K. Henning, C. Levey, C. Daghlian, J. Slinkman, J. Never, P. Kaszuba, R. Gluck, R. Wells, J. Pekarik, and R. Finch. Imaging integrated circuit dopant profiles with the force-based scanning Kelvin probe microscope. *Journal of Vacuum Science & Technology B: Microelectronics and Nanometer Structures*, 14(1):440–446, 1996.

[122] F. Müller, A.-D. Müller, M. Hietschold, and S. Kämmer. Detecting electrical forces in noncontact atomic force microscopy. *Measurement Science and Technology*, 9(5):734738, 1998.

[123] P. A. Rosenthal, E. T. Yu, R. L. Pierson, and P. J. Zampardi. Characterization of Al x Ga 1x As/GaAs heterojunction bipolar transistor structures using cross-sectional scanning force microscopy. *Journal of Applied Physics*, 87(4):1937, 2 2000.

[124] X. Xu, J. Mares, L. J. Groven, S. F. Son, R. G. Reifenberger, and A. Raman. Nanoscale characterization of mock explosive materials using advanced atomic force microscopy methods. *Journal of Energetic Materials*, 33(1):51–65, 1 2015.

[125] Y. Martin, D. W. Abraham, and H. K. Wickramasinghe. High-resolution capacitance measurement and potentiometry by force microscopy. *Applied Physics Letters*, 52(13):1103, 1988.

[126] D. Abraham and C. Williams. Lateral dopant profiling in semiconductors by force microscopy using capacitive detection. *Journal of Vacuum Science & Technology B: Microelectronics and Nanometer Structures*, 9(2):703–706, 1991.

[127] L. Kelvin. V. Contact electricity of metals. *Philosophical Magazine Series 5*, 46(278):82–120, 1898.

[128] A. Raman, J. Melcher, and R. Tung. Cantilever dynamics in atomic force microscopy. *Nano Today*, 3(1-2):20–27, 2 2008.

[129] L. Meirovitch. *Fundamentals of vibrations*. McGraw-Hill, 2001.

[130] J. Melcher, S. Hu, and A. Raman. Equivalent point-mass models of continuous atomic force microscope probes. *Applied Physics Letters*, 91(5):053101, 2007.

[131] X. Xu and A. Raman. Comparative dynamics of magnetically, acoustically, and Brownian motion driven microcantilevers in liquids. *Journal of Applied Physics*, 102(3):034303, 8 2007.

[132] T. Glatzel, S. Sadewasser, and M. Lux-Steiner. Amplitude or frequency modulation-detection in Kelvin probe force microscopy. *Applied Surface Science*, 210(1):84–89, 2003.

[133] S. Kitamura and M. Iwatsuki. High-resolution imaging of contact potential difference with ultrahigh vacuum noncontact atomic force microscope. *Applied Physics Letters*, 72(24):3154–3156, 6 1998.

[134] H. Diesinger, D. Deresmes, and T. Mélin. Capacitive crosstalk in AM-mode KPFM. In *Kelvin probe force microscopy: measuring and compensating electrostatic forces*, pages 25–44. 2012.

[135] S. Belaidi, P. Girard, and G. Leveque. Electrostatic forces acting on the tip in atomic force microscopy: Modelization and comparison with analytic expressions. *Journal of Applied Physics*, 81(3):1023, 1997.

[136] E. Bonaccurso, F. Schönfeld, and H.-J. Butt. Electrostatic forces acting on tip and cantilever in atomic force microscopy. *Physical Review B*, 74(8):085413, 8 2006.

[137] S. Gómez-Moñivas, L. S. Froufe-Pérez, A. J. Caamaño, and J. J. Sáenz. Electrostatic forces between sharp tips and metallic and dielectric samples. *Applied Physics Letters*, 79(24):4048–4050, 12 2001.

[138] S. Hudlet, M. Saint Jean, B. Roulet, J. Berger, and C. Guthmann. Electrostatic forces between metallic tip and semiconductor surfaces. *Journal of Applied Physics*, 77(7):3308, 1995.

[139] L. Fumagalli, G. Ferrari, M. Sampietro, and G. Gomila. Dielectric-constant measurement of thin insulating films at low frequency by nanoscale capacitance microscopy. *Applied Physics Letters*, 91(24):243110, 2007.

[140] A. Gil, J. Colchero, J. Gómez-Herrero, and A. M. Baró. Electrostatic force gradient signal: resolution enhancement in electrostatic force microscopy and improved Kelvin probe microscopy. *Nanotechnology*, 14(2):332–340, 2 2003.

[141] C. Riedel, A. Alegria, G. A. Schwartz, R. Arinero, J. Colmenero, and J. J. Saenz. On the use of electrostatic force microscopy as a quantitative subsurface characterization technique: A numerical study. *Applied Physics Letters*, 99(2):023101, 2011.

[142] C. Riedel, R. Arinero, A. Alegria, J. Colmenero, and J. J. Saenz. Three-dimensional tomography of single charge inside dielectric materials using electrostatic force microscopy. *MRS Proceedings*, 1421:11–1421, 1 2012.

[143] R. Arinero, C. Riedel, and C. Guasch. Numerical simulations of electrostatic interactions between an atomic force microscopy tip and a dielectric sample in presence of buried nano-particles. *Journal of Applied Physics*, 112(11):114313, 12 2012.

[144] G. Gramse, G. Gomila, and L. Fumagalli. Quantifying the dielectric constant of thick insulators by electrostatic force microscopy: effects of the microscopic parts of the probe. *Nanotechnology*, 23(20):205703, 5 2012.

[145] D. J. Griffiths. *Introduction to electrodynamics.* Prentice Hall, 3rd edition, 1999.

[146] R. Garcia. *Amplitude modulation atomic force microscopy.* Wiley-VCH, 2011.

[147] S. Rast, C. Wattinger, U. Gysin, and E. Meyer. The noise of cantilevers. *Nanotechnology*, 11(3):169–172, 9 2000.

[148] A. Kikukawa, S. Hosaka, and R. Imura. Vacuum compatible high-sensitive Kelvin probe force microscopy. *Review of Scientific Instruments*, 67(4):1463, 4 1996.

[149] C. Sommerhalter, T. W. Matthes, T. Glatzel, A. Jager-Waldau, and M. C. Lux-Steiner. High-sensitivity quantitative Kelvin probe microscopy by noncontact ultra-high-vacuum atomic force microscopy. *Applied Physics Letters*, 75(2):286, 7 1999.

[150] S. Batra. *Field assisted self assembly for preferential vertical alignment of particles and phases using a novel roll-to-roll processing line.* PhD thesis, University of Akron, 2014.

[151] W. Park, J. Hu, L. A. Jauregui, X. Ruan, and Y. P. Chen. Electrical and thermal conductivities of reduced graphene oxide/polystyrene composites. *Applied Physics Letters*, 104(11):113101, 3 2014.

[152] D. Kiracofe and A. Raman. On eigenmodes, stiffness, and sensitivity of atomic force microscope cantilevers in air versus liquids. *Journal of Applied Physics*, 107(3):033506, 2010.

[153] R. Garcia and E. T. Herruzo. The emergence of multifrequency force microscopy. *Nature Nanotechnology*, 7(4):217–26, 4 2012.

[154] C. Sommerhalter, T. Glatzel, T. Matthes, A. Jäger-Waldau, and M. Lux-Steiner. Kelvin probe force microscopy in ultra high vacuum using amplitude modulation detection of the electrostatic forces. *Applied Surface Science*, 157(4):263–268, 2000.

[155] M. Welvaert and Y. Rosseel. On the definition of signal-to-noise ratio and contrast-to-noise ratio for fMRI data. *PLoS ONE*, 8(11), 2013.

[156] R. E. Hendrick. Signal, noise, signal-to-noise, and contrast-to-noise ratios. In *Breast MRI*, pages 93–111. Springer New York, New York, NY, 2008.

[157] S. Sadewasser and T. Glatzel. *Kelvin Probe Force Microscopy*, volume 48 of *Springer Series in Surface Sciences*. Springer Berlin Heidelberg, Berlin, Heidelberg, 2012.

[158] D. C. Hurley and J. A. Turner. Measurement of Poisson's ratio with contact-resonance atomic force microscopy. *Journal of Applied Physics*, 102(3):033509, 2007.

[159] G. Stan, S. Krylyuk, A. V. Davydov, M. D. Vaudin, L. A. Bendersky, and R. F. Cook. Contact-resonance atomic force microscopy for nanoscale elastic property measurements: Spectroscopy and imaging. *Ultramicroscopy*, 109(8):929–36, 7 2009.

[160] R. Wagner, R. J. Moon, and A. Raman. Mechanical properties of cellulose nanomaterials studied by contact resonance atomic force microscopy. *Cellulose*, 23(2):1031–1041, 4 2016.

[161] U. Rabe. Atomic Force Acoustic Microscopy. In *Applied scanning probe methods II: scanning probe microscopy techniques*, pages 37–90. Springer Berlin Heidelberg, 2006.

[162] U. Rabe, S. Amelio, E. Kester, V. Scherer, S. Hirsekorn, and W. Arnold. Quantitative determination of contact stiffness using atomic force acoustic microscopy. *Ultrasonics*, 38(1):430–437, 2000.

[163] A. Gannepalli, D. Yablon, A. Tsou, and R. Proksch. Mapping nanoscale elasticity and dissipation using dual frequency contact resonance AFM. *Nanotechnology*, 22(35):355705, 9 2011.

[164] Z. M. Ma, L. Kou, Y. Naitoh, Y. J. Li, and Y. Sugawara. The stray capacitance effect in Kelvin probe force microscopy using FM, AM and heterodyne AM modes. *Nanotechnology*, 24(22):225701, 6 2013.

[165] P. Lorrain, D. R. Corson, and F. Lorrain. *Fundamentals of Electromagnetic Phenomena*. W. H. Freeman, 2000.

[166] K. Johnson. *Contact Mechanics*. Cambridge University Press, 1985.

[167] M. J. Cadena, Y. Chen, R. G. Reifenberger, and A. Raman. Sub-surface AFM imaging using tip generated stress and electric fields. *Applied Physics Letters*, 110(12):123108, 3 2017.

[168] Y. Shen, D. M. Barnett, and P. M. Pinsky. Simulating and interpreting Kelvin probe force microscopy images on dielectrics with boundary integral equations. *The Review of scientific instruments*, 79(2 Pt 1):023711, 2 2008.

[169] Y. Shen, D. Barnett, and P. Pinsky. Modeling electrostatic force microscopy for conductive and dielectric samples using the boundary element method. *Engineering Analysis with Boundary Elements*, 32(8):682–691, 8 2008.

[170] Z.-Y. Li, B.-Y. Gu, and G.-Z. Yang. Scanning-electrostatic-force microscopy: Self-consistent method for mesoscopic surface structures. *Physical Review B*, 57(15):9225–9233, 4 1998.

[171] S. Belaidi, F. Lebon, P. Girard, G. Leveque, and S. Pagano. Finite element simulations of the resolution in electrostatic force microscopy. *Applied Physics A*, 66:S239–S243, 1998.

[172] G. E. Box and N. R. Draper. *Empirical Model/building and response surfaces.* New York : Wiley, 1987.

[173] A. I. Khuri and S. Mukhopadhyay. Response surface methodology. *Wiley Interdisciplinary Reviews: Computational Statistics*, 2(2):128–149, 3 2010.

[174] N. R. Draper and H. Smith. *Applied Regression Analysis.* John Wiley & Sons, Inc., Hoboken, NJ, USA, 4 1998.

[175] G. M. Sacha, A. Verdaguer, J. Martinez, J. J. Saenz, D. F. Ogletree, and M. Salmeron. Effective tip radius in electrostatic force microscopy. *Applied Physics Letters*, 86(12):123101, 2005.

[176] R. Myers and D. C. Montgomery. *Response surface methodology.* John Wiley & Sons, Inc, 2nd edition, 2002.

[177] K.-T. Fang, R. Li, and A. Sudjianto. *Design and Modeling for Computer Experiments.* Taylor & Francis Group, 2006.

[178] T. Simpson, J. Poplinski, P. N. Koch, and J. Allen. Metamodels for Computer-based Engineering Design: Survey and recommendations. *Engineering with Computers*, 17(2):129–150, 7 2001.

[179] F. Sanchez, M. Budinger, and I. Hazyuk. Dimensional analysis and surrogate models for the thermal modeling of Multiphysics systems. *Applied Thermal Engineering*, 110:758–771, 1 2017.

[180] W. Du, N. Xue, A. Gupta, A. M. Sastry, J. R. R. A. Martins, and W. Shyy. Optimization of LiMn 2 O 4 electrode properties in a gradient- and surrogate-based framework. 29:335–347, 2013.

[181] S. A. I. Bellary, R. Adhav, M. H. Siddique, B.-H. Chon, F. Kenyery, and A. Samad. Application of computational fluid dynamics and surrogate-coupled evolutionary computing to enhance centrifugal-pump performance. *Engineering Applications of Computational Fluid Mechanics*, 10(1):171–181, 1 2016.

[182] H.-J. Butt, B. Cappella, and M. Kappl. Force measurements with the atomic force microscope: Technique, interpretation and applications. *Surface Science Reports*, 59(1-6):1–152, 10 2005.

[183] J. Sacks, W. J. Welch, T. J. Mitchell, and H. P. Wynn. Design and Analysis of Computer Experiments. *Statistical Science*, 4(4):409–423, 11 1989.

[184] I. Hazyuk, M. Budinger, F. Sanchez, and C. Gogu. Optimal design of computer experiments for surrogate models with dimensionless variables. *Structural and Multidisciplinary Optimization*, 56(3):663–679, 9 2017.

[185] D. Lacey and C. Steele. The use of dimensional analysis to augment design of experiments for optimization and robustification. *Journal of Engineering Design*, 17(1):55–73, 1 2006.

[186] A. A. Sonin. A generalization of the Pi-theorem and dimensional analysis. *Proceedings of the National Academy of Sciences of the United States of America*, 101(23):8525–6, 6 2004.

[187] T. Szirtes and P. Rózsa. Structure of physical relations. In *Applied Dimensional Analysis and Modeling*, chapter 7, pages 133–161. Elsevier, 2007.

[188] J. A. Turner and J. S. Wiehn. Sensitivity of flexural and torsional vibration modes of atomic force microscope cantilevers to surface stiffness variations. *Nanotechnology*, 12(3):322–330, 9 2001.

[189] M. Kopycinska-Müller, R. H. Geiss, and D. C. Hurley. Contact mechanics and tip shape in AFM-based nanomechanical measurements. *Ultramicroscopy*, 106(6):466–74, 4 2006.

[190] D. G. Yablon, A. Gannepalli, R. Proksch, J. Killgore, D. C. Hurley, J. Grabowski, and A. H. Tsou. Quantitative viscoelastic mapping of polyolefin blends with contact resonance atomic force microscopy. *Macromolecules*, 45(10):4363–4370, 5 2012.

[191] M. Clerc and J. Kennedy. The particle swarm - explosion, stability, and convergence in a multidimensional complex space. *IEEE Transactions on Evolutionary Computation*, 6(1):58–73, 2002.

[192] S. Ebbesen, P. Kiwitz, and L. Guzzella. A generic particle swarm optimization Matlab function. In *2012 American Control Conference*, pages 1519–1524, 2012.

[193] D. B. Parkinson. Robust design employing a genetic algorithm. *Quality and Reliability Engineering International*, 16(3):201–208, 5 2000.

[194] Z. Ma and D. G. Seiler. *Metrology and diagnostic techniques for nanoelectronics*. Pan Stanford Publishing Pte, Ltd., Taylor & Francis Group, 1st edition, 11 2016.

[195] A. Sugimoto, Y. Kembo, K. Watanabe, and T. Yaguchi. Current status and outlook of 3D inspection analysis for semiconductor devices. Technical report, 2007.

[196] IEEE. International Roadmap for Devices and Systems. Technical report, 2017.

[197] R. E. Marks and H. Schnabl. Genetic algorithms and neural networks: a comparison based on the repeated prisoners dilemma. In *Computational techniques for modelling learning in economics*, pages 197–219. Springer, Boston, MA, 1999.

[198] A. Yao, K. Kobayashi, S. Nosaka, K. Kimura, and H. Yamada. Visualization of Au nanoparticles buried in a polymer matrix by scanning thermal noise microscopy. *Scientific reports*, 7:42718, 2 2017.

[199] P. De Wolf, Z. Huang, B. Pittenger, M. Febvre, D. Mariolle, and N. Chevalier. Multidimensional mapping of electrical properties using fast force volume. In *APS March Meeting 2018*. American Physical Society, 2018.

[200] Asylum Research. The NanomechPro toolkit: nanomechanical AFM techniques for diverse materials. Technical report.

[201] J. Lekner. Electrostatic calibration of spheresphere forces. *Meas. Sci. Technol*, 23:85007–4, 2012.

[202] COMSOL Multiphysics. Structural mechanics module: user's guide. Technical report, 2017.

APPENDICES

A. ADDITIONAL INFORMATION ON CHAPTER 2

A.1   Microcantilever Dynamics

The microcantilever motion driven by an external force F_{drive} can be described by the Euler Bernoulli beam partial differential Equation (A.1)

$$EIw''''(x,t) + c^*\dot{w} + \rho A\ddot{w}(x,t) = F_{drive}(x,t). \tag{A.1}$$

where EI, $w(x,t)$, c* ρ and A are the flexural rigidity, transverse displacement, damping, mass density and cross-sectional area of the beam, respectively. It assumes the microcantilever is a slender beam where the bending stress dominates the shear force and rotatory inertia is negligible.

To solve Equation (A.1), first, we consider the case of the undamped free response given by

$$EIw''''(x,t) + \rho A\ddot{w}(x,t) = 0. \tag{A.2}$$

Assuming a separable solution of the form $w(x,t) = W(x)T(t)$ and replacing in Equation (A.2), we get

$$EIT(t)W''''(x) + \rho AW(X)\ddot{T}(t) = 0. \tag{A.3}$$

Rearranging terms

$$\frac{\ddot{T}(t)}{T(t)} = \frac{-EI}{\rho A}\frac{W''''(x)}{W(x)}. \tag{A.4}$$

The above equation must be true for all x and t, therefore each side is equal to a constant $-\omega^2$. It results into the following ordinary differential equations

$$\ddot{T}(t) + \omega^2 T(t) = 0, \tag{A.5}$$

$$W''''(x) - \alpha^4 W(x) = 0, \tag{A.6}$$

where $\alpha^4 = \omega^2 \frac{\rho A}{EI}$. The solution to Equations (A.33) and (A.6) are given by

$$T(t) = C\cos(\omega t) + S\sin(\omega t), \tag{A.7}$$

$$W(x) = a\cosh(\alpha x) + b\sinh(\alpha x) + c\cos(\alpha x) + d\sin(\alpha x). \tag{A.8}$$

Enforcing boundary conditions, we can find the coefficients in Equation (A.8). In this case, it is considered a fixed microcantilever at $x = 0$ and free at $x = L$. Therefore,

$$w(0,t) = 0 \text{ (no motion)}, \tag{A.9}$$

$$w'(0,t) = 0 \text{ (zero slope)}, \tag{A.10}$$

$$w''(L,t) = 0 \text{ (zero moment)}, \tag{A.11}$$

$$w'''(L,t) = 0 \text{ (zero shear force)}. \tag{A.12}$$

Using Equations (A.9) and (A.10), it is found that $a = -c$, $b = -d$. From Equations (A.11) and (A.12)

$$\begin{bmatrix} \cosh(\alpha L) + \cos(\alpha L) & \sinh(\alpha L) + \sin(\alpha L) \\ \sinh(\alpha L) - \sin(\alpha L) & \cosh(\alpha L) + \cos(\alpha L) \end{bmatrix} \begin{bmatrix} c \\ d \end{bmatrix} = \begin{bmatrix} 0 \\ 0 \end{bmatrix}. \tag{A.13}$$

Non-trivial solutions give the characteristic equation given by

$$\cos(\alpha L)\cos(\alpha L) + 1 = 0, \tag{A.14}$$

where $\alpha_i = 1.875,\ 4.694,\ 7.855...$, for $i = 1, 2, 3....$

The modal functions are given by

$$\psi_i(x) = \cos\left(\alpha_i \frac{x}{L}\right) - \cosh\left(\alpha_i \frac{x}{L}\right) + \left(\frac{\sin(\alpha_i) - \sinh(\alpha_i)}{\cos(\alpha_i) + \cosh(\alpha_i)}\right)\left(\sin\left(\alpha_i \frac{x}{L}\right) + \sin\left(\alpha_i \frac{x}{L}\right)\right), \tag{A.15}$$

where it is chosen the normalization of the eigenfunctions $\psi_i(L) = 1$, relevant in the discretization of the forced response as shown below [130]. The eigenfrequencies are given by

$$\omega_i = \alpha_i^2 \sqrt{\frac{EI}{\rho A}}. \tag{A.16}$$

The general solution to Equation (A.2) is

$$w(x,t) = \sum_{i=1}^{\infty} \psi_i(x)[C_i\cos(\omega_i t) + S_i\sin(\omega_i t)]. \tag{A.17}$$

Now we consider the response under the presence of an excitation force, which in this case refers to the electrostatic force. It is considered as a point force applied at the end of the microcantilever. Therefore, F_{drive} in Equation (A.1) is equal to $F\delta(x - L)$, where δ is the Dirac delta function. Equation (A.1) is discretized using Galerkin's method [129]. This approach assumes a solution in the form

$$w(x,t) = \sum_{j=1}^{\infty} \psi_j(x)q_j(t), \tag{A.18}$$

where $\psi_j(x)$ are the orthogonal basis functions of the normalized eigenmodes found in Equation (A.15), and $q_j(t)$ are the generalized coordinates of the basis functions.

Then, we substitute $w(x,t)$ into Equation (A.1), multiply by $\psi_i(x)$ and integrate over the microcantilever length (L), so that

$$\int_0^L \psi_i(x)\left[EI\sum_j \psi_j''''(x)q_j(t) + c^*\sum_j \psi_j(x)\dot{q}(t) + \rho A\sum_j \psi_j(x)\ddot{q}_j(t)\right]dx$$

$$= \int_0^L \psi_i(x)F\delta(x - L). \tag{A.19}$$

Recall that $\psi_i(L) = 1$, which ensures $q(t)$ is the actual tip deflection. Using orthogonality of the eigenfunctions the above equation is equal to

$$\left(EI\int_0^L \psi_i(x)\psi_i''''(x)dx\right)q_i(t) + \left(c^*\int_0^L \psi_i^2(x)dx\right)\dot{q}_i(t)$$

$$+ \left(\rho A\int_0^L \psi_i^2(x)\right)\ddot{q}_i(t) = F\psi_i^2(L). \tag{A.20}$$

This equation can be reduced to

$$m_i\ddot{q}_i(t) + c_i\dot{q}_i(t) + k_i(t) = F(t), \tag{A.21}$$

where i = 1, 2, 3, ..., N, $m_i = \rho A\int_0^L \psi_i^2(x)dx$, $c_i = c * \int_0^L \psi_i^2(x)dx\dot{q}_i(t)$, and $k_i = EI\int_0^L \psi_i(x)\psi_i''''(x)dx$ are the modal mass, and equivalent damping and stiffness, respectively. Dividing Equation (A.21) by k_i,

$$\frac{\ddot{q}_i(t)}{\omega_i^2} + \frac{\dot{q}_i(t)}{\omega_i Q_i} + q_i(t) = \frac{F(t)}{k_i}, \tag{A.22}$$

where ω_i and Q_i are the natural frequency and quality factor, respectively. Equation (A.22) corresponds to the point-mass model used in this work.

A.2 Electrostatic Force Calculation Using the Maxwell Stress Tensor

The electromagnetic force on an arbitrary charge distribution with a volume V having a position dependent charge density $\rho(x, y, z)$, in the presence of an electric field $\mathbf{E}$ and magnetic field $\mathbf{B}$ is given by

$$\mathbf{F} = \int_V (\mathbf{E} + \mathbf{v} \times \mathbf{B})\rho dV, \tag{A.23}$$

$$= \int_V (\rho\mathbf{E} + \mathbf{J} \times \mathbf{B})dV, \tag{A.24}$$

where $dV = dxdydz$ and $\mathbf{J}$ is defined as the current density due to the velocity v of the charge distribution ρ. Then, the force per unit volume in a region of space could be defined as

$$\mathbf{f} = \rho\mathbf{E} + \mathbf{J} \times \mathbf{B}. \tag{A.25}$$

Using Maxwell's equations

$$\nabla \cdot \mathbf{E} = \frac{\rho}{\epsilon_0}, \tag{A.26}$$

$$\nabla \times \mathbf{B} = \mu_0\mathbf{J} + \mu_0\epsilon_0\frac{\partial\mathbf{E}}{\partial t}, \tag{A.27}$$

and

$$\frac{\partial}{\partial t}(\mathbf{E} \times \mathbf{B}) = \left(\frac{\partial\mathbf{E}}{\partial t} \times \mathbf{B}\right) + \left(\mathbf{E} \times \frac{\partial\mathbf{E}}{\partial t}\right) \tag{A.28}$$

combined with Faraday's law

$$\frac{\partial\mathbf{B}}{\partial t} = -\nabla \times \mathbf{E}, \tag{A.29}$$

we can re-write Equation (A.25) in terms of the fields alone as

$$\mathbf{f} = \epsilon_0\left[(\nabla \cdot \mathbf{E})\mathbf{E} - \mathbf{E} \times (\nabla \times \mathbf{E})\right] - \frac{1}{\mu_0}\left[\mathbf{B} \times (\nabla \times \mathbf{B})\right] - \epsilon_0\frac{\partial}{\partial t}(\mathbf{E} \times \mathbf{B}). \tag{A.30}$$

Using the vector identity $\nabla(E^2) = 2(\mathbf{E} \cdot \nabla)\mathbf{E} + 2\mathbf{E} \times (\nabla \times \mathbf{E})$ and Maxwell's second equation $\nabla \cdot \mathbf{B} = 0$, $\mathbf{f}$ in a symmetrical form is equal to

$$\mathbf{f} = \epsilon_0 \left[(\nabla \cdot \mathbf{E})\mathbf{E} + (\mathbf{E} \cdot \nabla)\mathbf{E} \right] + \frac{1}{\mu_0} \left[(\nabla \cdot \mathbf{B})\mathbf{B} + (\mathbf{B} \cdot \nabla)\mathbf{B} \right]$$
$$- \frac{1}{2}\nabla \left[\epsilon_0 \mathbf{E^2} + \frac{1}{\mu_0}B^2 \right] - \epsilon_0 \frac{\partial}{\partial t}(\mathbf{E} \times \mathbf{B}). \quad (A.31)$$

Limiting to problems where B is neglected, Equation (A.31) can be simplified as

$$\mathbf{f} = \epsilon_0 \left[(\nabla \cdot \mathbf{E})\mathbf{E} + (\mathbf{E} \cdot \nabla)\mathbf{E} \right] - \frac{1}{2}\nabla(\epsilon_0 E^2). \quad (A.32)$$

The Maxwell Stress Tensor is defined as [145]

$$\mathbf{T} = T_{ij} \equiv \epsilon_0 \left(E_i E_j - \frac{1}{2}\delta_{ij}E^2 \right), \quad (A.33)$$

where i, j refer to the coordinates x, y, z. It can be shown that

$$(\nabla \cdot \mathbf{T})_j = \epsilon_0 \left[(\nabla \cdot \mathbf{E})E_j + (\mathbf{E} \cdot \nabla)E_j \right] - \frac{1}{2}\nabla_j(E^2), \quad (A.34)$$

which implies that the for per unit volume given by Equation (A.32) can be written in a simple form $\mathbf{f} = (\nabla \cdot \mathbf{T})$.

Therefore, the force $\mathbf{F}$ on an arbitrary charge distribution is given by

$$\mathbf{F} = \int_V (\nabla \cdot \mathbf{T})dV. \quad (A.35)$$

Using the divergence theorem, Equation (A.35) is equal to

$$\mathbf{F} = \oint_S \mathbf{T} \cdot d\mathbf{s}, \quad (A.36)$$

which means that instead of solving the volume integral given in Equation (A.24), we can calculate the force by a surface integral over an arbitrary surface (Equation (A.36)). Physically, $\mathbf{T}$ represents the force per unit area acting on the surface S. Thus T_{xx}, T_{yy}, T_{zz} represent normal forces and T_{xy}, T_{xz}, etc. represent shear forces.

B. ADDITIONAL INFORMATION ON CHAPTER 4

B.1 Probe Parameters

The probe used to collect the subsurface data set using KPFM is the NanoWorld Pointprobe EFM. SEM images shown in figure B.1, were taken on the probe before collecting the data on the model sample presented in Chapter 2. The tip radius was found from the high resolution image at the bottom right. The dimensions of the probe are given in table B.1.

The stiffness, quality factor and resonance frequency of the microcantilever are 4.7 N/m, 224.7 and 79.9 kHz, respectively. These values are found from the standard experimental calibration procedure.

Table B.1. Dimensions of EFM probe (NanoWorld).

	Data	Value
microcantilever	Length	225 (220 - 230) μm
	Width	28 (22.5 - 32.5) μm
	Thickness	3.0 (2.5 - 3.5) μm
Tip	Tip height	12.5 $\pm$ 2.5 μm
	Tip radius	31.6 $\pm$ 2.5 nm
	Angle	25°

B.2 Parameters Used in Finite Element Model

The relevant parameters of the computational model built for the parametric sweep computations are summarized in table B.2.
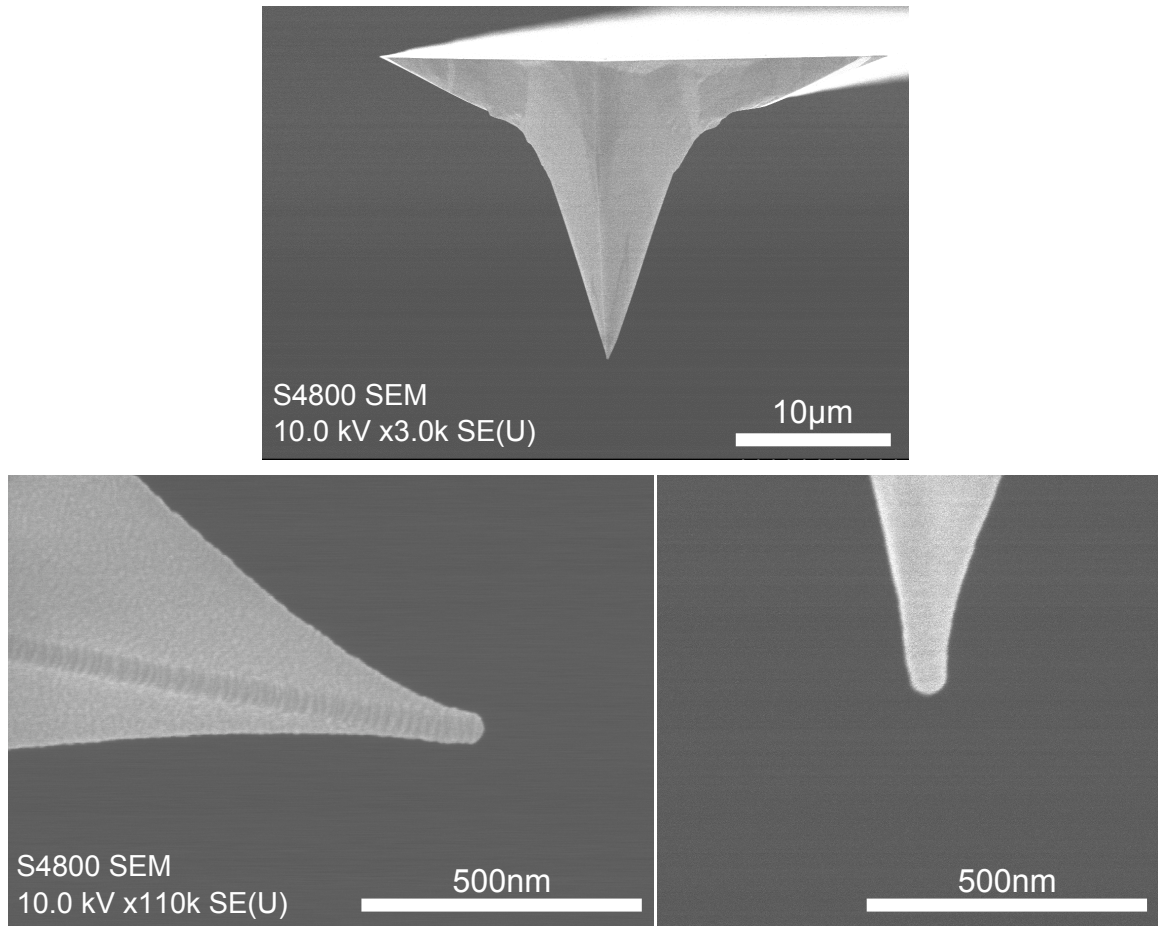
Figure B.1. SEM images of NanoWorld Pointprobe EFM probe used to collect the experimental subsurface data set in model sample. The estimated tip radius is 31.2 ± 3 nm

B.3 Surrogate Models

Other functions were evaluated in the process of building the surrogate-model based on the computational data. Table B.3 summarizes some of them.

Table B.2. Parameters used in 2D axisymmetric model in Comsol Multiphysics.

	Data	Value
microcantilever (disk)	Radius	14 μm
	Thickness	3.0 μm
Tip (cone)	Height	12.5 μm
	Angle	25
Tip (apex)	Radius	30 nm
Sample (buried sphere)	Radius (r_s)	Variable, 15 - 55 nm
	Dielectric constant (ϵ_f)	1500
	Depth (d)	Variable, 10 - 100 nm
Sample (polymer matrix)	Width	25 μm
	Thickness	Variable
	Dielectric constant (ϵ_m)	2.5
Tip-sample distance	Z	Variable, 10 - 100 nm
Bias voltage	V_t	1 V

Table B.3.   Other models used in the investigation of an adequate surrogate models.

Model	$\tilde{F}(Z,d)$	R^2
Sphere-sphere approx.[a]	$\tilde{F} = 1 + \left(\frac{b_1 r_s}{b2 + r_s}\right)^2 \left(\frac{b_3}{(Z + b_4 d + b5)^2}\right)$	0.967

$$\tilde{F}(\hat{Z}, \hat{d})$$

Model	$\tilde{F}(\hat{Z},\hat{d})$	R^2
1$^{\text{st}}$-order pol.	$\tilde{F} = b_0 + b_1 \hat{Z} + b_2 \hat{d}$	0.926
2$^{\text{nd}}$-order pol.	$\tilde{F} = b_0 + b_1 \hat{Z} + b_2 \hat{d} + b_{12} \hat{Z}\hat{d} + b_{11}\hat{Z}^2 + b_{22}\hat{Z}^2$	0.995

$$\tilde{F}(\hat{Z}, \hat{d}, r_s)$$

Model	$\tilde{F}(\hat{Z},\hat{d},r_s)$	R^2
2$^{\text{nd}}$-order pol.	$\tilde{F} = b_0 + b_1 \hat{Z} + b_2 \hat{d} + b_3 r_s + b_{12}\hat{Z}\hat{d} +$ $b_{13}\hat{Z}r_s + b_{23}\hat{d}r_s + b_{11}\hat{Z}^2 + b_{22}\hat{d}^2 + b_{33}r_s^2$	0.995

[a] This approach follows the derivation of an expression derived for the electrostatic force between two spheres [201].

C. ADDITIONAL INFORMATION ON CHAPTER 5

C.1 Particle Size Distribution in Model Sample

The size of the $BaTiO_3$ particles is estimated by measuring their height from topography maps obtained using AFM. These were taken after the particle dispersion was deposited on a silicon substrate. Figure C.1 shows the histogram of the particle size distribution from 100 particles. The solid line corresponds to a normal distribution curve. The mean particle diameter is 44.6 ± 17.7 nm.
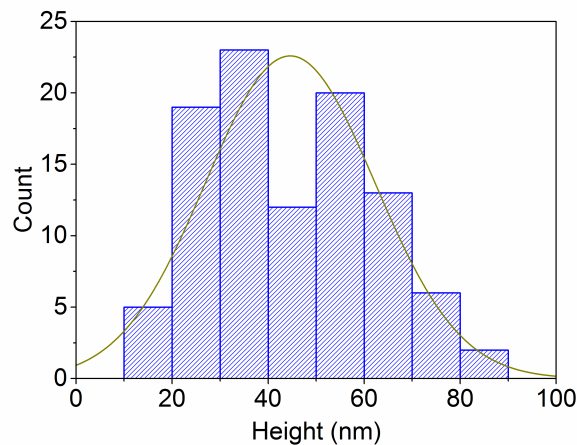

Figure C.1. $BaTiO_3$ particles size distribution.

C.2 2D Axisymmetric Model in Comsol Multiphysics

The contact mechanics problem involving the tip and the 0D buried object embedded in a polymer matrix is solved using the 2D axisymmetric solid mechanics interface from the structural mechanics module in Comsol Multiphysics.

The model assumes all the objects are linear elastic, homogeneous and isotropic and only includes the frictionless part. The geometry of the model is shown in figure

C.2. A contact pair is defined by the boundary of the apex of the tip and the top boundary of the polymer matrix. The load is applied on the top boundary of the tip apex, and there is a fixed constraint at the bottom of the polymer matrix. The stationary problem is solved with a force boundary condition. For stability, we added a spring foundation node to the boundary load. It assumes an initial spring before the tip apex establishes contact with the base object and it is removed afterwards [202]. Table C.1 shows the main settings used in the model.
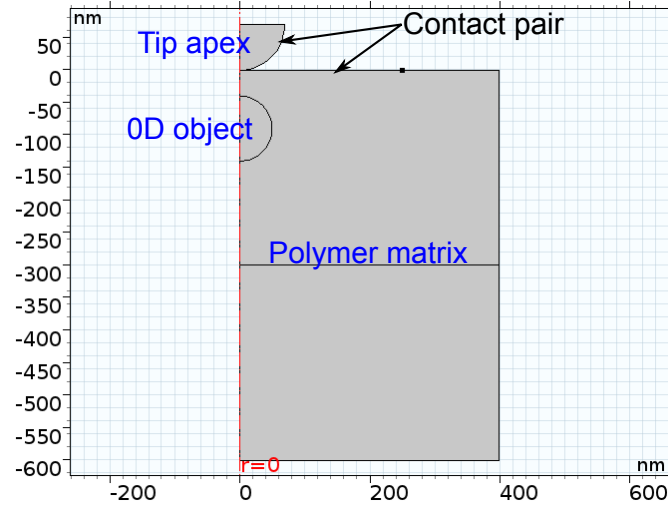
Figure C.2. Model geometry

Table C.1. Parameters used in the 2D axisymmetric model.

Parameter	Value	Description
E_m	3 Gpa	Young's modulus of polymer matrix
ν_m	0.3	Poisson's ratio of polymer matrix
E_p	67 Gpa	Young's modulus of particle
ν_p	0.3	Poisson's ratio of particle
E_t	170 Gpa	Young's modulus of tip
ν_t	0.28	Poisson's ratio of tip
W_m	400 (nm)	Width matrix
H_m	600 (nm)	Height matrix

VITA

VITA

Maria J. Cadena was born in Pasto, Colombia. She received her B.Sc. degree in Electronic Engineering from Universidad de Nariño in Pasto, Colombia. After graduation, she attended Universidad de los Andes in Bogota, Colombia, where she received a M.Sc. degree in engineering with an emphasis in electronic engineering and computers. She first joined Purdue University as a visiting scholar in Prof. Ramans research group. After graduating from Universidad de Los Andes, she was accepted by Purdue University to pursue a Ph.D. degree in Mechanical Engineering. Her doctoral research was advised by Prof. Arvind Raman and Prof. Ron Reifenberger, with a focus on the subsurface characterization capabilities of the atomic force microscope.